Surface effects on charge carrier dynamics in semiconductor quantum dots

Pooja Tyagi

Department of Chemistry
McGill University
Montréal, Québec, Canada
February 2013

A thesis submitted to McGill University
in partial fulfillment of the requirements of the degree of
Doctor of Philosophy

Abstract

Due to the large surface-to-volume ratio of quantum dots, their surface conditions play a significant role in determining their electronic and optical properties. In this thesis, we show that the presence of surface states modifies the optical selection rules in quantum dots and enhances the rate of surface charge trapping. These surface-induced effects have profound impact on the measurement of multiexciton recombination and carrier multiplication processes. Specifically, in transient absorption studies, surface states result in additional decay timescales which may be misattributed to multiexciton recombination processes. Additionally, they lead to large "apparent" carrier multiplication yields even under conditions where it is forbidden by energy conservation. The surface-dependent transient absorption studies presented in this work suggest ways to identify and minimize the undesirable surface-induced signals.

Interestingly, surface-induced processes also result in significant electrostatic effects. We show that due to the piezoelectric nature of wurtzite CdSe quantum dots, the strong electric field created by surface charge trapping can drive coherent acoustic phonons in these systems. We further show that the amplitude of this piezoelectric response can be controlled by altering the surface conditions of the quantum dot. Finally, we theoretically investigate the

effect of multiple surface layers on carrier localization in nanostructures. We find that in a core/barrier/shell configuration, layered nanostructures offer independent control over electron and hole wave functions. These results suggest design principles for wave function engineering in potential quantum dot applications in light emitting devices, photovoltaics and optical amplification.

Résumé

En raison du rapport surface volume élevé des points quantiques, les conditions de leurs surfaces jouent un rôle important dans la détermination des propriétés électroniques et optiques. Dans cette thèse, nous démontrons que la prsence d'états de surface modifie les règles de sélection optiques dans les points quantiques et améliore le taux de piégeage des charges sur la surface. Ces effets induits par la surface ont un impact profond sur la mesure de la recombinaison de mutliexcitons et les processus de multiplication de porteurs. Plus précisément, en poursuivant des études d'absorption transitoires, nous démontrons que la présence des états de surface se traduits dans des délais de décroissance supplémentaires qui peuvent être attribuées à tort à des processus de recombinaison de multiexcitons. En outre, ils conduisent à de grandes rendements apparents de multiplication des porteurs, même dans des conditions où il est interdit par la conservation de l'énergie. Les études d'absorption transitoires de la surface présentés dans ce travail suggèrent des moyens d'identifier et de réduire les signaux indésirables induits par la surface.

Fait intéressant, les processus induites par la surface entraînent aussi des effets électrostatiques significatifs. Nous démontrons qu'en raison de la nature piézoélectrique des points quantiques de wurtzite CdSe, le fort champ électrique créé par le piégeage de charges sur la surface peut conduire des

phonons acoustiques cohérents dans ces systèmes. En plus, nous démontrons que l'amplitude de cette réponse piézo-électrique peut être contrôlé en modifiant les conditions de la surface du point quantique. Enfin, nous avons étudié théoriquement l'effet sur la localisation des porteurs de strates multiples de surface dans les nanostructures. Nous constatons que dans une configuration de base/barrière/coque, les nanostructures stratifiées offrent un contrôle indépendant sur la fonction d'onde des électrons et trous. Ces résultats suggèrent des principes de conception pour l'ingénierie de fonction d'onde dans des applications potentielles de points quantiques dans les dispositifs émettant de la lumière, l'énergie photovoltaque et de l'amplification optique.

Acknowledgements

First of all, I would like to thank my advisor Patanjali Kambhampati for his constant support and encouragement throughout my PhD. His scientific expertise and foresight have been invaluable in the compilation of this work. Pat gave me the independence that I needed for my scientific development while always being available for guidance. Anyone who has ever interacted with him will agree that his enthusiasm and love for science are contagious.

Graduate school gave me the opportunity to work with a fascinating group of people. I am grateful to Dr. Ryan Cooney and Dr. Sam Sewall for training me as a first-year grad student and leaving an amazing spectroscopy set-up for us to build on. Eva Dias was the go-to person for chats about science, tea and art. Our discussions of core/barrier/shell nanostructures (that she can synthesize in her sleep) inspired the work presented in Chapter 6. Jonathan Saari is talented with lasers, and I thank him for taking good care of the equipment used in this thesis and always being available for help. Jonathan Mooney probably knows everything there is to know about cryostats and vacuum pumps, including procurement. I thoroughly enjoyed our discussions of the reaction coordinate and low-temperature studies. Michael Krause is an independent thinker, so it was no surprise that he synthesized white-light quantum dots (with special PLE features) within his first year of grad school. I thank him for helping me with my first quantum dot synthesis. Brenna Walsh has eagerly adapted to the new directions of the lab, quickly learning and contributing to

2D experiments. Thanks to Dr. Yousef Kamali and Dr. Amin Kabir, post-docs in our group, for helping out when needed. And to Dr. Sagar, our first post-doc. I would like to thank all Kambhampati group members, esp. Jon, Jonathan and Michael, for their company, lunch at Thomson House, stimulating discussions and a memorable grad school experience. Sharing office space with the Siwick group gave me the pleasure of getting to know Vance Morrison, Bob Chatelain, Andrew Bruhacs, Chris Godbout, Mark Stern and Shona McGowan. I would like to thank them all for making the office atmosphere fun and enjoyable.

I am thankful to my thesis committee members Prof. Brad Siwick, Prof. David Ronis and Prof. Paul Wiseman for their probing scientific questions and helpful advice. Chantal Marrotte was quick to resolve any technical issues that came up during the course of this work. She cares well for grad students and makes the tortuous McGill thesis submission process a breeze.

I have been fortunate to have friends like Nidhi Khurana, Sakshi Bajaj and Shipra Khanna, whom I could always rely on. I thank Lars Grant for being a constant source of support and understanding.

I am humbled to be loved by a wonderfully large family that I would like to thank. For the sake of brevity, I restrict myself to thanking Bibi, Babaji and Binny for their motivation and support. Thanks to my parents, Rakesh and Sushma, for providing the love, security and support that allowed me to undertake unconventional endeavours with little apprehension. To my brother Monu, for always making me laugh. To Snowie, my little bundle of joy. And above all, to my sister, Nikki, for continually reminding me what is truly important in life.

Contributions and Statement of Originality

The author claims that this thesis constitutes original scholarship and makes distinct contributions to knowledge. The work presented in this thesis is mainly an adaption of original research papers published in peer-reviewed journals [1–3]. Chapter 4 is based on Ref. [2] (Reprinted with permission from [Tyagi, P. and Kambhampati, P., J. Chem. Phys. 2011, 134, 094706]. Copyright 2011, American Institute of Physics). Jonathan I. Saari and Jonathan Mooney assisted with part of the data acquisition in this project. Pooja Tyagi performed data analysis and modeling. Pooja Tyagi wrote the manuscript in collaboration with Prof. Kambhampati.

Chapter 5 is based on Ref. [1] (Adapted with permission from [Tyagi, P. et. al., Nano Lett. 10 (8), 3062 (2010)]. Copyright 2010, American Chemical Society). The experiments presented in this chapter were performed by Pooja Tyagi in collaboration with Ryan R. Cooney. Discussions with Ryan R. Cooney, Samuel L. Sewall, D. M. Sagar and Jonathan I. Saari were helpful in the development this project. Pooja Tyagi performed data modeling. Pooja Tyagi and Prof. Kambhampati wrote the manuscript.

Chapter 6 is an adaption of Ref. [3] (Adapted with permission from [Tyagi, P. and Kambhampati, P., J. Phys. Chem. C 2012, 116, 8154 8160]. Copyright

2012, American Chemical Society). Pooja Tyagi performed the calculations, and wrote the manuscript in collaboration with Prof. Kambhampati. Appendix A is based on unpublished work from our group in Ref. [4]. Jonathan I. Saari and Pooja Tyagi share first authorship in Ref. [4]. Pooja Tyagi, Jonathan I. Saari, Nicolas Forget, Vincent Crozatier developed the 2D spectroscopy set-up. Pooja Tyagi designed the experiment, wrote the data analysis software, analyzed data and wrote the manuscript in collaboration with Prof. Kambhampati. The phase stability experiments were carried out by Pooja Tyagi, Jonathan I. Saari and Nicolas Forget. Jonathan I. Saari implemented the 2D spectroscopy set-up and executed 2D experiments with the assistance of Brenna Walsh and Amin Kabir.

Table of Contents

Abstract ii

Résumé iv

Acknowledgements vi

Contributions and
Statement of Originality viii

List of Figures xiii

List of Tables xvi

List of Abbreviations xvii

1 Introduction 1

1.1 Auger processes: non-radiative recombination and relaxation 3
1.1.1 Surface dependence of Auger processes 4
1.2 Role of Auger processes in photoluminescence blinking . . . 6
1.3 Optical gain in semiconductor nanocrystals 7
1.4 Carrier multiplication 8
1.4.1 Surface effects on observed carrier multiplication signals 10
1.5 Measurement of carrier multiplication and Auger recombination processes 12
1.6 Exciton-phonon interaction 15
1.6.1 Exciton-phonon interaction in metal nanoparticles . . 16
1.6.2 Exciton-phonon interaction in quantum wells 17
1.6.3 Exciton-phonon interaction in quantum dots 17
1.6.4 Surface effects on exciton-phonon coupling 19
1.7 The mysterious photoproduct 21
1.8 Wave function control in nanostructures 24

1.9 Thesis overview . . . 27

2 Theoretical background . . . 29

2.1 Quantum confinement . . . 30
2.2 Effective-mass model . . . 30
2.3 Many-body interactions in nanostructures . . . 33
2.4 CdSe nanocrystals . . . 36

3 Experimental methods . . . 39

3.1 Pump-probe Spectroscopy . . . 39
3.2 Experiment . . . 41
3.3 Second Harmonic Generation . . . 41
3.4 Self-phase Modulation . . . 44
3.5 Pulse compression . . . 46
3.6 Pulse characterization: Autocorrelation . . . 48
3.6.1 Intensity autocorrelation . . . 49
3.6.2 Interferometric autocorrelation . . . 50

4 Surface effects on multiexciton generation and multiexciton recombination signals . . . 52

4.1 Introduction . . . 53
4.2 Experimental Methods . . . 56
4.3 Results and Discussion . . . 57
4.3.1 Surface dependence of bleach dynamics . . . 57
4.3.2 Signatures of surface induced processes in semiconductor quantum dots . . . 60
4.3.3 Role of state-filling in the observed multiexciton recombination dynamics . . . 66
4.3.4 Fluence and surface dependence reveal false multiexciton recombination signals . . . 72
4.3.5 Surface-induced effects on multiexciton generation signals . . . 75
4.3.6 Implications for blinking in quantum dots . . . 79
4.4 Conclusions . . . 80

5 Piezoelectric response in semiconductor quantum dots via surface charge trapping . . . 82

5.1 Introduction . . . 83
5.2 Experimental Methods . . . 86
5.3 Results and Discussion . . . 87

5.4 Conclusions . . . 98
5.A Appendix . . . 99

6 Wave function enginering in core/barrier/shell nanostructures . . . 112

6.1 Introduction . . . 113
6.2 Methods . . . 118
6.3 Results and Discussion . . . 120
6.4 Conclusions . . . 129

7 Conclusions . . . 131

A Appendix A . . . 135

Bibliography . . . 152

List of Figures

Figure		page
1–1	Emission colors as a function of size for CdSe/ZnS quantum dots	2
1–2	Schematic of non-radiative Auger processes	4
1–3	Illustration of CM process in semiconductor quantum dots	8
1–4	Linear absorption spectrum of CdSe quantum dots	12
1–5	Band edge bleach as a function of time for CdSe quantum dots	14
1–6	Schematic of Type-I and Type-II nanostructures	25
2–1	Quantum confinement effect in semiconductor nanocrystals	32
2–2	Schematic of a core/barrier/shell nanostructure	32
2–3	Schematic of a core/shell nanosctructure	34
2–4	Degeneracy breaking in CdSe nanocrystals	37
3–1	Schematic illustration of a pump-probe spectroscopy experiment	40
3–2	Schematic illustration of second-order nonlinear processes	42
3–3	Phase matching in a negative uniaxial crystal	44
3–4	Self-phase modulation of a Gaussian pulse	45
3–5	Schematic illustration of a prism compressor	47
3–6	Intensity autocorrelation	49
4–1	Linear absorption and band-edge transient absoprtion signal for CdSe quantum dots	55

4–2 Surface-dependence of the transient absorption signal in CdSe quantum dots 58

4–3 Illustration of two forms of excited state absorption in the visible regime in CdSe quantum dots 61

4–4 Time-dependent transient absorption spectra of CdSe quantum dots for different surface passivations 63

4–5 Schematic illustration of the chronology of multicarrier excitation, relaxation, and recombination 67

4–6 Illustration of the onset of state-filling in CdSe quantum dots . . 69

4–7 Simulation of ground state bleaching dynamics in CdSe quantum dots 70

4–8 High fluence ground state bleaching signal for phototreated, untreated and ZnS-capped CdSe quantum dots 71

4–9 Fluence dependence of ground state bleach as a function of exciton population for different surface conditions 73

4–10 False positive signals for multiexciton generation in transient absorption studies 76

5–1 Phonons in CdSe quantum dots 85

5–2 Transient absorption spectra for different surface passivations of CdSe quantum dots 89

5–3 Surface-dependent phonon amplitudes in CdSe quantum dots . . 92

5–4 Fluence-dependent phonon amplitudes for different surface passivations 94

5–5 Linear absorption and photoluminescence spectra of photo-treated and untreated CdSe quantum dots 99

5–6 Transient absorption spectra for photo-treated and untreated CdSe quantum dots 101

5–7 Determination of the number of surface trapped charges using the photo-induced absorption signal in CdSe quantum dots . . 102

5–8 Modeling phonons in photo-treated and untreated CdSe quantum dots 110

6–1 Localization regimes of an exciton in a core/barrier/shell nanostructure . . . 115

6–2 Probability of finding electron (hole) in the core as a function of core radius and barrier width for a CdSe/ZnS/CdSe nanostructure . . . 117

6–3 Overlap of electron and hole wave functions in CdSe/ZnS/CdSe as a function of core radius and barrier width . . . 122

6–4 Electron and hole kinetic energies and their interaction energy as a function of core radius in CdSe/ZnS/CdSe nanostructures 125

6–5 Effective mass-dependence of 1S carrier localization for fixed barrier height and shell thickness in CdSe/ZnS/CdSe nanostructures . . . 126

6–6 Dependence of 1S carrier localization on the height of the confinement barrier in CdSe/ZnS/CdSe nanostructures . . . 128

A–1 Schematic of a 2D spectrum . . . 136

A–2 Schematic of the different geometries used in a 2D spectroscopy experiment . . . 139

A–3 Dual-shaper set-up for 2D spectroscopy . . . 141

A–4 Phase stability measurements of a dual-shaper set-up . . . 143

A–5 Polarization shaping using a dual-shaper set-up . . . 145

A–6 2D spectrum of CdSe quantum dots . . . 147

A–7 Demonstration of a two-step phase cycling scheme . . . 149

A–8 Population time dependence of 2D absorptive spectrum of CdSe QDs . . . 151

List of Tables

Table		page
1–1	A comparison between Type-I and Type-II nanostructures	26
5–1	Calculation of $N_{surface}$ for photo-treated CdSe ($R = 1.6nm$) QDs	105
5–2	Calculation of $N_{surface}$ for untreated CdSe ($R = 1.6nm$) QDs . .	105
A–1	Comparison of boxcar and pump-probe geometries	140

List of Abbreviations

$\boldsymbol{e^-}$ ..... Electron

$\boldsymbol{h^+}$ ..... Hole

Δ_{XX} ..... Biexciton Binding Energy

ϵ ..... Dielectric Constant

Cd ..... Cadmium

CM ..... Carrier Multiplication

e-ph ..... Electron-phonon

EFM ..... Electric Force Microscopy

EMA ..... Effective-mass Approximation

ESA ..... Excited State Absorption

FFT ..... Fast Fourier Transform

FWHM ..... Full Width at Half Maximum

GSB ..... Ground State Bleach

GVD ..... Group Velocity Dispersion

LA ..... Longitudinal Acoustic

LED ..... Light emitting diodes

LO ..... Longitudinal Optical

MCR ..... Multicarrier Recombination

MEG ..... Multiexciton Generation

MER ..... Multiexciton Recombination

MX ..... Multiexciton

NC ..... Nanocrystal

OD ..... Optical Density

PA ..... Photoinduced Absorption

PL ..... Photoluminescence

PV ..... Photovoltaic

QD ..... Quantum Dot

QE ..... Quantum Efficiency

QW ..... Quantum Well

Se ..... Selenium

SHG ..... Second Harmonic Generation

SPM ..... Self-phase Modulation

t-PL ..... Time resolved Photoluminescence

TA ..... Transient Absorption

TOPO ..... Trioctylphosphine oxide

X ..... Exciton

XX ..... Biexciton

'Science is a way of thinking much more than it is a body of knowledge.'

- Carl Sagan

Chapter 1

Introduction

Consisting of as few as hundreds of atoms, nanocrystals (NCs) provide an elegant avenue to experimentally study quantum mechanical effects. Additionally, the ability to tune the optical and electronic properties of NCs by controlling their size and composition makes them attractive for numerous applications ranging from solar cells to medical imaging. The promise that nanomaterials hold both in advancing the understanding of basic physics and in revolutionizing technology has led to extensive research in the field of nanoscience over the past two decades.

The tremendous progress made in the field of NC synthesis has made it possible to study the optical and electronic properties of these materials as a function of their shape, size, composition and environment [5–14]. These investigations, in addition to theoretical predictions, have revealed potential applications of nanomaterials in cell labeling, drug delivery, light-emitting diodes and efficient photovoltaic devices (PVs) [15–21].

Most of the interesting properties of NCs are a consequence of the quantum confinement effect. This effect occurs when the size of a semiconductor becomes comparable to the wavelength of the carrier (electron or hole), causing

the carrier to be "confined" within the boundaries of the material. In analogy with the particle-in-a-box model, quantum confinement results in a discrete, size-dependent energy spectrum in semiconductor NCs[a]. This property can be used to tune to emission color of NCs to desired wavelengths by varying their size. In fact, the emission color of CdSe/ZnS NCs is tunable over the whole visible range of the electromagnetic spectrum (Figure 1–1).

FIGURE 1–1: Size-dependence of emission colors for CdSe/ZnS nanocrystals. Reprinted by permission from Macmillan Publishers Ltd: [Nature Biotechnology] (Han, M.Y., Gao, X.H., Su, J.Z. and Nie, S.M., Nat. Biotechnol. 19, 631635 (2001)), copyright 2001.

Additionally, the three-dimensional confinement of charge carriers in NCs causes a large overlap of electron and hole wave functions, thereby enhancing multicarrier interactions in these quantum-confined systems. In the following sections, we summarize a few important implications of quantum confinement in semiconductor NCs.

[a]See *Chapter 2: Theoretical background* for details.

1.1 Auger processes: non-radiative recombination and relaxation

The spacing between the energy levels of a NC is typically much larger than the longitudinal optical (LO) phonon energy. Therefore, NCs were expected to exhibit slow hot carrier relaxation times because multiphonon emission would be required for the hot carrier to cool down to low energy states [15, 22–25]. This phenomenon is also known as the "phonon bottleneck" effect.

In contrast to these expectations, fast carrier relaxation times (on the order of a picosecond) were observed in colloidal semiconductor NCs [24, 26–30]. Moreover, smaller NCs showed faster carrier relaxation. These studies suggested the presence of a non-phonon-mediated relaxation pathway that became dominant with increasing confinement. Subsequent theoretical investigations showed that charge carriers in NCs could relax via an Auger-type energy transfer between electrons and holes; and hence, bypass the proposed phonon bottleneck [31–33].

An Auger process refers to a relaxation or recombination event in which the energy released is not emitted as a photon but is instead transferred to another charge carrier (Figure 1–2). Quantum confinement causes a large overlap of electron and hole wave functions, resulting in enhanced carrier-carrier interactions in NCs as compared to their bulk counterparts. These strong Coulombic interactions, in turn, lead to an increased efficiency of non-radiative Auger processes in semiconductor nanostructures [29, 31, 34]. Furthermore, electron-hole overlap increases with increasing confinement, and therefore, smaller NCs

will exhibit faster carrier relaxation. The enhanced efficiency of Auger processes significantly affects multiexciton dynamics, optical gain lifetimes, photoluminescence (PL) blinking and multiexciton generation in semiconductor NCs.

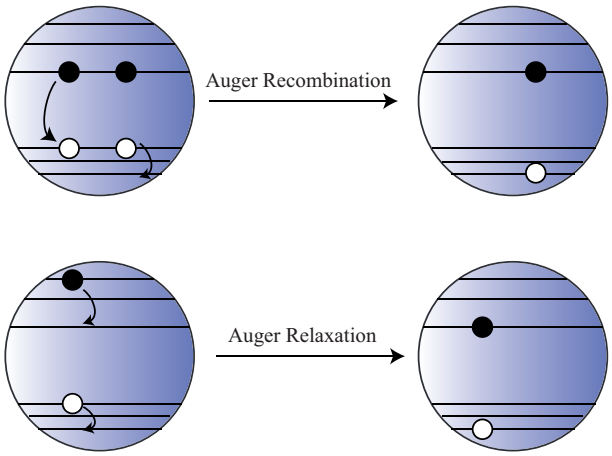

FIGURE 1–2: Schematic of non-radiative Auger recombination (top) and relaxation (bottom) processes in semiconductor nanocrystals. The solid black and white circles denote electrons and holes respectively

1.1.1 Surface dependence of Auger processes

As discussed above, the efficiency of Auger recombination and relaxation processes increases with decreasing NC size because of confinement-enhanced Coulomb interaction between electrons and holes. The exact nature of the electron-hole energy transfer in an Auger-type process is further revealed by surface-dependent measurements of charge carrier dynamics in quantum dots (QDs)[b].

[b]In this thesis, we use the terms "quantum dot" and "nanocrystal" interchangeably to refer to colloidal semiconductor nanoparticles prepared using solution phase chemistry.

One can control the overlap of electron and hole wave functions (and hence, manipulate electron-hole interaction) by modifying the surface properties of the QD. Guyot-Sionnest et al. carried out one of the first experiments that very nicely illustrate surface dependence of Auger processes [26]. They performed infrared pump-probe spectroscopy measurements on CdSe QDs with three different surface ligands: (*i*) Trioctylphosphine oxide (TOPO), (*ii*) thiocresol, and (*iii*) pyridine, to study intraband relaxation dynamics. These capping groups control the coupling strength of the hole to the QD core states, with pyridine having the weakest coupling and thiocresol and TOPO have stronger coupling in increasing order. Nevertheless, all of these capping groups eliminate any electron traps by passivating the surface Cd atoms. These experiments showed that decoupling the hole from the electron in the QD core significantly slowed down the intraband relaxation, further confirming an Auger-type electron-hole energy transfer.

Essentially, trapping the hole on the surface of the QD (by using pyridine as a ligand), suppresses the Auger relaxation channel and increases carrier relaxation times. Subsequently, several studies corroborated the presence of efficient Auger processes in semiconductor NCs [24, 27–30, 35]. Additionally, the exact pathway of the electron-hole energy transfer in Auger relaxation in CdSe QDs was revealed by state-dependent studies of relaxation dynamics [24]. These measurements showed that in CdSe QDs, it is the electron that transfers its excess kinetic energy to the hole, which then relaxes via surface ligand induced nonadiabatic channel and phonon emission. This topic will be further discussed in Chapter 4, where we investigate surface effects on the measurement of Auger processes in CdSe QDs. In particular, we will show

that surface-induced processes can lead to additional fast decay time scales in transient absorption (TA) signals, which may be misinterpreted as Auger recombination times for multiexcitons. We also show that based on the degeneracy of the desired state and observed spectral features in the TA spectra, one can distinguish surface-induced artifactual signals from real Auger recombination signals.

1.2 Role of Auger processes in photoluminescence blinking

The intermittency in the PL of single QDs under continuous excitation is called "blinking". The blinking behaviour of semiconductor QDs is usually ascribed to Auger-type processes involving charged excitons [36, 37]. In the charged-exciton picture, an extra charge is present in the QD, and the photoexcited electron-hole pair undergoes nonradiative Auger recombination with this extra charge, thereby rendering the QD "dark" or "off". When the QD neutralizes, it returns to its "bright" or "on" state.

However, in disagreement with the charging model, recent studies have suggested that there may be alternative channels that cause blinking [2, 14, 38–41]. Specifically, time-resolved PL (t-PL) studies have shown that the dark state of the QD has decay times faster than that of the biexciton [38, 39]. Also, excited off-state decay rates increase with increase in off-state duration suggesting a distribution of nonradiative decay rates [40, 41]. Both of these observations are inconsistent with the predictions of the charging model. So far, it is clear that there is photo-product that causes QDs to blink, but the nature of this photo-product still remains elusive. Based on our studies of surface-dependent recombination dynamics Chapter 4, we suggest that this

photo-product may be a charge-neutral "polarized" QD instead of a "charged" QD.

1.3 Optical gain in semiconductor nanocrystals

The original idea to manipulate quantum effects in semiconductor heterostructures for the purpose of producing spectrally tunable and low threshold optical gain was proposed by Dingle and Henry in 1976 [42]. The quantization and size-dependence of the energy spectrum in 3D-confined NCs is expected to result in increased thermal stability and wavelength tunability of optical gain.

In fact, spectrally tunable, size-dependent optical gain was first observed in CdSe QDs, both in solution and in thin-films [43,44]. An important result of these studies was that the magnitude of optical gain decreased with decreasing size, approaching zero for NC radius of $2.3nm$. This trend was ascribed to the enhancement of multicarrier interactions in NCs with decreasing size, which limits the development of optical gain in two ways: (i) enhanced carrier-carrier interactions cause shifting of energy levels such that the incident probe photon, instead of causing stimulated emission, gets absorbed by the NC, and (ii) Auger recombination becomes more efficient with decreasing size and leads to short multiexcitonic lifetimes ($\sim 100ps$), which in turn, limits the gain lifetime [25, 45–49]. However, it was later discovered that these strong multicarrier interactions could be manipulated by state-selective pumping and by designing novel nanostructures that modified the localization of electron and hole wave functions.

In particular, by preparing the QD in a suitable initial state, optical gain could be recovered in small CdSe NCs (radius $< 2.3nm$) [47, 48]. It has now also been shown that alloyed nanostructures that have a smooth confinement

potential and "giant" nanocrystals consisting of a small core capped with a thick passivating shell exhibit suppressed Auger decay and consequently, long-lived ($\sim 10ns$) optical gain with broad spectral bandwidth ($\sim 500meV$) [12]. More recently, it was shown that the spatial separation of different excitons in core/barrier/shell nanostructures also slows down multiexcitonic recombination and increases the bandwidth and lifetime of optical gain [50].

1.4 Carrier multiplication

Carrier multiplication (CM), also known as multiexciton generation (MEG), refers to the creation of multiple electron-hole pairs via absorption of a single photon. The prospect of CM in nanoparticles has arguably generated the most interest in the NC community because of its considerable potential for solar energy conversion. In bulk semiconductors, the CM process is inefficient and limits the conversion efficiency of conventional solar cells. In NCs, however, CM is expected to be enhanced due to quantum confinement effects. This expectation relies on the fact that due to the translational symmetry breaking, the law of momentum conservation is relaxed in NCs, and therefore, only the total energy would be conserved in carrier relaxation processes.

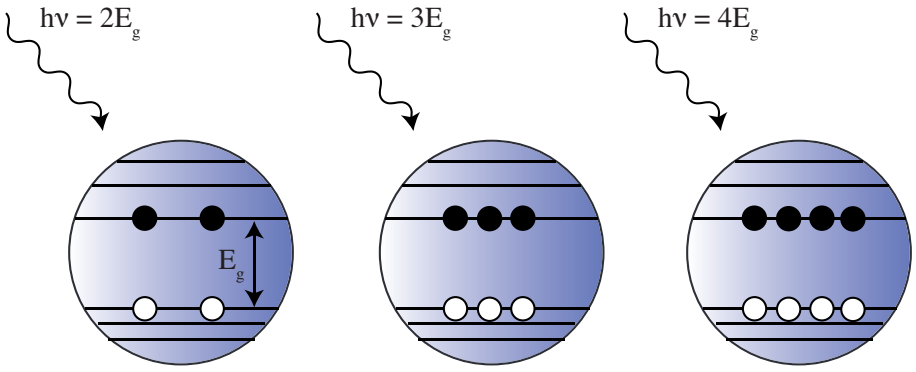

FIGURE 1–3: Illustration of CM process in semiconductor nanocrystals

In a CM event, absorption of a high energy photon creates a high energy exciton, and the excess kinetic energy of the hot exciton, instead of being dissipated as heat, is used to create additional electron-hole pairs (Figure 1–3). An important requirement for the CM process to occur is that energy of the incident photon must be at least twice the material band gap to satisfy energy conservation. For $h\nu < 2E_g$, there will be insufficient energy to create an extra electron-hole pair, whereas a photon of energy $h\nu = nE_g$ can, in principle, dissipate energy to produce n electron-hole pairs, each with E_g units of energy.

A. Nozik first proposed that enhanced CM in NCs could be exploited to make more efficient solar cells [15, 16]. This prediction led to experimental investigations of CM in NCs, and it was in 2004 that the first experimental signature of CM was observed in PbSe NCs [51]. Further work led to observations of CM signals in other QD systems such as CdSe [52] and PbS [53] NCs, with PbSe NCs having the highest conversion efficiency of seven excitons per absorbed photon, i.e. a quantum efficiency of 700% [54]. Interestingly, CM signals were also observed in single-walled carbon nanotubes [55]. In contradiction to the results cited above, there have also been studies reporting inefficient or even the absence of CM in NCs [56–61]. In some cases, even for the same samples studied using same experimental techniques by different groups, there is little to no agreement between reported CM yields [61, 62]. CM yields reported in InAs QDs by Pijpers et al. were retracted by the same authors [63, 64]. McGuire et al. showed that stirring the QD sample during the experiment could diminish the observed CM yields [57]. This inconsistency

between different reports casts doubt on the existence of CM, and the nature or efficiency of CM in NCs still remains controversial.

Several arguments have been proposed to explain these contradictory CM results. First, an inaccurate measurement of absorption cross-sections for different pump wavelengths will lead to a misestimation of the number of absorbed photons, and therefore, multiple exciton generation due to multiphoton absorption may be misinterpreted as CM. Alternate methods, that do not require the measurement of absolute cross-sections, were also suggested for studying CM [56]. Second, spatial inhomogeneities in the pump beam may cause non-Poissonian distribution of excitons in QDs. In other words, multiexcitons could be generated by absorbing multiple photons from different regions in the spatial inhomogenous pump beam. Sample-to-sample variability has also been cited as one of the possible reasons for difference in reported CM yields. As we shall discuss in Chapter 4, surface-induced effects in QDs can also lead to inflated "apparent" CM yields, even under conditions where CM is forbidden by energy conservation (i.e. $h\nu < 2E_g$). It is likely that a combination of all these effects is responsible for the reported discrepancies in the CM literature.

1.4.1 Surface effects on observed carrier multiplication signals

In this thesis, we focus on the effect of surface characteristics on the observed CM signals. The first demonstration of surface-dependent CM signals was by McGuire et al. in 2008 [57]. By using TA spectroscopy and t-PL, they showed that stirring the sample during the experiment could diminish the observed CM yields in PbSe QDs. In particular, they observed that static

samples show attenuated late time PL and TA signals. There was also an increase in the early time PL while the TA signal remained unchanged at early times. They invoked a photo-ionization process to rationalize these observations. Basically, in the absence of stirring, a fraction of QDs in the sample get photo-ionized. These ionized QDs will have long-lived charges and create a sub-ensemble of "charged" QDs within the sample, resulting in the trends observed in their t-PL and TA data.

In our work (Chapter 4), we investigate the surface-dependence of observed CM signals in CdSe QDs. We find that surface-induced charge trapping effects and modification of optical selection rules can give false measurement of CM yields. In fact, we observe 200% CM yields under conditions where CM is forbidden by energy conservation. Our measurements also show that irradiating the sample with intense radiation during the course of the experiment leads to the degradation of NC surface, making them susceptible to surface-induced artifactual signals that obscure the "real" state-filling signals. We further show that these spurious signals manifest themselves as photo-induced absorption (PA) in the TA spectra. Therefore, one can identify the presence of surface effects by in-situ measurement of TA spectra.

It is worth noting that, in contrast to the charging model as proposed by McGuire et al. [57], our results suggest that it may be the presence of a surface-trapped excitonic state (i.e. a "polarized" rather than a "charged" QD) that is responsible for false CM yields. This polarized dot also has implications for measurement of Auger recombination processes and PL blinking in QDs as discussed in Section 1.1.1 and Section 1.2 respectively.

1.5 Measurement of carrier multiplication and Auger recombination processes

The results presented in this thesis were obtained using pump-probe spectroscopy, also known as TA spectroscopy, which is a commonly employed technique to study CM and multicarrier dynamics in semiconductor QDs[c]. In a pump-probe experiment, a pump pulse perturbs the sample at time $t = 0$, thereby changing its optical density (OD), and a probe pulse measures this change (ΔOD) as a function of time delay (τ) between the pump and the probe pulses. The change in the optical density of the band edge state (ΔOD_{1S}) is the parameter of interest for the study of multicarrier dynamics and CM in QDs.

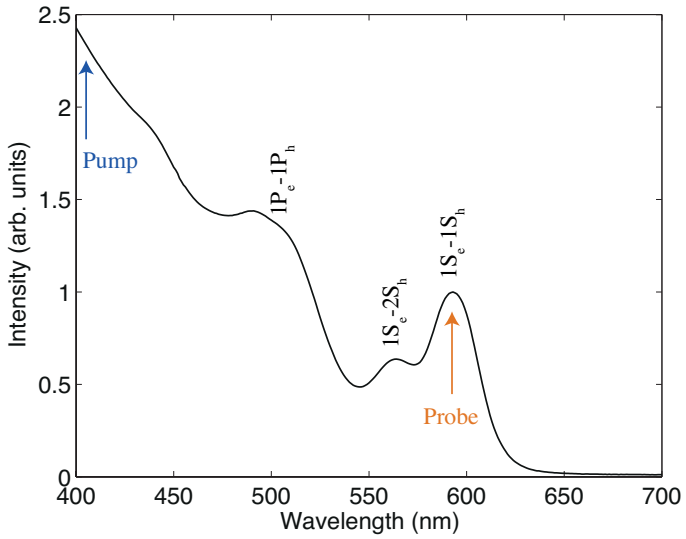

FIGURE 1–4: Linear absorption spectrum of CdSe QDs with band edge (labeled $1S_e - 1S_h$) at $597nm$. The arrows denote the pump and probe excitation wavelengths.

[c]See *Chapter 3: Experimental methods* for details of pump-probe spectroscopy.

Figure 1–4 shows a linear absorption spectrum of CdSe QDs with the band edge state labeled as $1S_e - 1S_h$. ΔOD_{1S} is proportional to the sum of the $1S$ electron and hole occupation numbers (n^e_{1S} and n^h_{1S}), i.e. $\Delta OD_{1S} = -OD_0(n^e_{1S} + n^h_{1S})$, where OD_0 is the optical density of the sample at the $1S$ peak. In CdSe QDs, the low energy hole states have a high spectral density whereas the $1S$ electronic state is two-fold degenerate ($g_{1S} = 2$). Therefore, ΔOD_{1S} is mainly determined by n^e_{1S}, i.e. $\Delta OD_{1S} \approx -OD_0(n^e_{1S})$. This assumption has also been experimentally confirmed by state-selective pumping of excitonic states in CdSe QDs, which showed that the band edge bleach signal (ΔOD_{1S}) is independent of the initial $1S$ hole state and is primarily due to $1S$ electrons [30]. Time-resolved measurements of ΔOD_{1S} can therefore be used to study multicarrier dynamics, and to extract multiexciton recombination times and CM yields in semiconductor QDs.

A pump pulse creates an initial exciton population which decays nonradiatively via Auger recombination on a $10ps - 100ps$ time scale, and the QD is left with a single exciton which decays on a nanosecond time scale. Figure 1–5 shows the band edge bleach (ΔOD_{1S}) as a function of the time delay between pump and probe pulses for CdSe QDs under high energy excitation ($\lambda_{pump} = 400nm$). The late time magnitude of ΔOD_{1S} is due to the long-lived single exciton and the early time magnitude reflects the number of excitons initially created by the excitation pulse. Therefore, for a single absorbed photon, the ratio of the early and late times amplitudes gives the CM yield of the QD.

Also, multiexcitonic recombination times can be extracted by fitting ΔOD_{1S} signal to a multiexponential decay function. For CdSe QDs, recombination

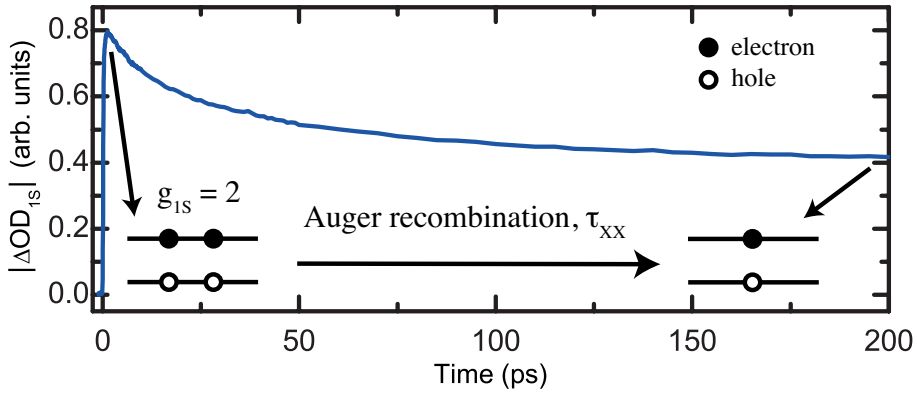

FIGURE 1–5: Band edge bleach (ΔOD_{1S}) as a function of time for CdSe QDs for $\lambda_{pump} = 400nm$. g_{1S} denotes the degeneracy of the band edge state.

times for up to four excitons have been reported using this method [29]. However, as we show in Chapter 4, owing to the two-fold degeneracy of the $1S$ state, it is not possible to determine recombination times of more than two excitons from ΔOD_{1S}. Our experiments reveal that in photodegraded QDs, surface-induced signals overlap with the state-filling signals (ΔOD_{1S}); consequently, giving false measurement of multiexciton recombination and CM processes. In particular, surface effects lead to additional fast time scales in ΔOD_{1S}, which may be misinterpreted as recombination times for multiexcitons ($N > 2$). Following the same reasoning, in the presence of artifactual surface-induced signals, ΔOD_{1S} does not give a true measure of CM yields. We also show that the surface-induced artifactual signals in ΔOD_{1S} by using well-passivated CdSe QDs (e.g. CdSe/ZnS).

Terminology for labeling different surface conditions

Here, we define the terminology used in this thesis to label CdSe QDs with different surface conditions. We performed measurements on CdSe QDs with three kinds of surface passivations, (i) CdSe/ZnS core/shell or "capped" QDs,

(*ii*) CdSe core-only or "untreated" QDs, and (*iii*) "photo-treated" CdSe QDs. As the name suggests, CdSe/ZnS QDs have a CdSe core capped with a ZnS shell. Since the band gap of ZnS is nearly twice the band gap of CdSe, it serves as an excellent potential barrier for low energy excitons. The photo-treated CdSe QDs are prepared by irradiating the core-only CdSe QD sample with high energy $400nm$ radiation for 2 hours prior to the experiment. The core-only CdSe QDs are "untreated" QDs without a passivating inorganic shell. We show that the photo-treatment process enhances the surface-induced effects in CdSe QDs whereas capping with ZnS minimizes any surface trapping processes. The untreated QDs represent the intermediate regime between well passivated (CdSe/ZnS) and poorly passivated (photo-treated CdSe) systems.

1.6 Exciton-phonon interaction

Exciton-phonon interaction is an inelastic scattering process in which excitons lose (gain) energy by emission (absorption) of phonons[d]. Broadly speaking, excitons can interact with lattice vibrations via three coupling mechanisms, (*i*) Fröhlich interaction for optical phonons, and (*ii*) deformation potential coupling and (*iii*) piezoelectric coupling for acoustic phonons. In Fröhlich interaction, optical phonons couple to the polarization created by the relative displacement of positive and negative ions. The deformation potential coupling is due to the interaction of electrons with the changes in the energy band

[d]Lattice vibrations (or phonons) play a significant role in determining the physical and electronic properties of a material. Most notably, electron-phonon interactions are responsible for superconducting behaviour of certain materials as originally proposed by Bardeen, Cooper and Schreiffer in 1957 in their BCS theory [65], for which they were awarded the Nobel prize in Physics in 1972.

structure due to lattice vibrations whereas piezoelectric coupling refers to the interaction electrons with strain-induced lattice polarization. Although this work mainly focuses on acoustic phonon generation in semiconductor QDs, in this section, we describe mechanisms of phonon generation in different quantum confined systems.

1.6.1 Exciton-phonon interaction in metal nanoparticles

In metal nanoparticles, the dominant mechanism for exciton-acoustic-phonon interaction is believed to be impulsive lattice heating (via deformation potential coupling) [66–69]. A femtosecond laser pulse will create a nonthermal electron distribution, which rapidly thermalizes via electron-electron scattering on a subpicosecond time scale. The thermalized population can then be characterized by an electronic temperature. Since electrons have a small heat capacity, they can reach very high temperatures, even at small pump fluences. Following thermalization, hot electrons transfer energy to the lattice on a timescale impulsive with respect to the acoustic phonon time period, thereby exciting phonon modes in the nanoparticle. This three-step phonon excitation process can be conveniently described using a two-temperature model defined as,

$$\begin{aligned} \frac{dT_e}{dt} &= -g\frac{T_e - T_l}{C_e(T_e)} \\ \frac{dT_l}{dt} &= -g\frac{T_l - T_e}{C_l} - \frac{T_l - T_0}{t_s} \end{aligned} \tag{1.1}$$

where, g is the electron-phonon coupling constant, T_e is the electronic temperature, T_l is the lattice temperature, C_l and (C_e) are the lattice and electronic specific heats respectively, and $\frac{1}{t_s}$ is the rate at which heat is transferred to

the surroundings at temperature T_0. Since, C_e much greater than C_l, the final temperature of the metal nanoparticles after electron-phonon scattering is much lower than T_e. For example, Ref. [69] reports a final temperature of 20°C for initial $T_e = 1000$°C.

1.6.2 Exciton-phonon interaction in quantum wells

In quantum wells, the lattice mismatch between different kinds of materials strains the lattice and creates an intrinsic polarization. Photoexcited charge carriers created by a femtosecond laser pulse can impulsively screen this in-built polarization and launch coherent acoustic vibrations of the lattice via piezoelectric interaction [70–73]. As one would expect, the strength of the piezoelectric coupling relative to the deformation potential coupling depends on the strain in the quantum well lattice. For instance, in unstrained GaAs/AlAs superlattices, the acoustic phonon amplitude is an order of magnitude smaller than that for strained InGaN quantum well, indicating stronger piezo coupling the latter material [71, 74]. Furthermore, the amplitude of phonon oscillations can also be controlled by, for example, applying an external bias voltage or varying the relative phases of the incident pump pulses in a two-pump experiment [71, 73].

1.6.3 Exciton-phonon interaction in quantum dots

Due to three-dimensional confinement, the phonon modes in semiconductor QDs become quantized, also known as "phonon confinement". Exciton-phonon interaction is an important factor in determining exciton dynamics

and homogeneous linewidths in QDs. For instance, the optically dark excitonic state in CdSe QDs can undergo phonon-assisted radiatve decay[e]. Over the past few decades, exciton-phonon interaction in QDs has been investigated using several experimental (photoluminescence, transient absorption, continuous wave spectroscopy) and theoretical approaches [75–84].

Initial continuous wave (CW) spectroscopy experiments on QDs suggested a large coupling of excitons to LO phonons and negligible coupling to longitudinal acoustic (LA) phonons [76, 77, 79]. The first experimental observation of coherent acoustic phonon in a semiconductor QD was by Krauss and Wise in PbS QDs using transient absorption spectroscopy [81]. Subsequently, LA phonons were also observed in CdSe and InAs QDs [82]. Contrary to the CW experiments, these time-resolved measurements observed little to no coupling to optical phonons. It was suggested that CW experiments measured exciton coupling to QDs that had developed surface trapped charges over the course of the experiment whereas femtosecond experiments, due their time-resolved nature, measured coupling to a neutral QD. Therefore, in CW measurements, the polarized QD showed a large coupling to optical phonons via Fröhlich interaction.

This issue of mutually exclusive observation of LA and LO phonons (specifically in CdSe QDs) was resolved by state-selective femtosecond spectroscopy measurements by Sagar et al. [83,84]. They reported simultaneous observation

[e]The dark state has an angular momentum projection of 2 and therefore, requires emission of two photons to be optically active. However, in a phonon-assisted decay process, the extra unit of momentum is carried by an LO phonon. For details, see *Chapter 2: Theoretical background*.

of LA and LO phonons in CdSe QDs for excitation into the lowest excitonic state ($1S$). However, LO coupling strength diminished with increasing excitonic state energy, whereas LA coupling demonstrated very weak excitonic state dependence. These results were consistent with earlier time-resolved experiments which used high energy excitation and showed no coupling to LO phonons [82].

Size-dependent studies show that the frequency of LO phonons does not depend on size whereas the LA phonon frequency decreases with decreasing size [83]. This observation supports a deformation potential coupling mechanism for LA phonons, which allows us to model acoustic phonons as elastic vibrations of an isotropic homogeneous sphere (QD). As we will discuss in Chapter 5, we discover a new extrinsic piezoelectric coupling mechanism for LA phonons in CdSe QDs. The strength of this piezo coupling is found to be nearly an order of magnitude larger than the deformation potential coupling. Furthermore, the coupling strength can be tuned by modifying the surface properties of the QD.

1.6.4 Surface effects on exciton-phonon coupling

In addition to affecting multicarrier dynamics and CM signals (Section 1.1.1 and Section 1.4.1), surface has a significant impact on exciton-phonon interactions in semiconductor QDs. The modification of the elastic constant at the QD surface (by capping the QD with a different material) can change the deformation potential coupling to acoustic phonons. For example, capping CdSe QDs and nanorods with ZnS shell completely attenuates acoustic phonon amplitude [1, 85]. Additionally, the piezoelectric interaction can be controlled by changing the polarization of the QD, for example, by using suitable ligands

or changing the shape of the QD. As discussed in Chapter 5, in this thesis, we propose a novel way of controlling the piezolectric exciton-acoustic phonon interaction in QDs via *impulsive creation* of polarization.

Since CdSe has a wurtzite lattice, it is piezoelectric in nature and therefore has a non-zero intrinsic dipole moment. Also, high energy excitons have approximately 1eV of energy to dissipate. Therefore, one might expect to see both lattice heating (analogous to metals in Section 1.6.1) and intrinsic field screening (similar to quantum wells in Section 1.6.2) contributions to e-ph coupling in these QDs. We examine both of these pathways in CdSe QDs by conducting surface- and fluence-dependent TA spectroscopy measurements on three surface conditions described in Section 1.5.

If lattice heating were the dominant mechanism, the phonon amplitude would increase with increasing photon energy because higher energy excitons have more energy to dissipate to the lattice. However, previous studies have shown that the acoustic phonon amplitude is independent of the initial excitonic state [83, 84]. Also, since the excitation and observation conditions are identical for the three systems (capped, untreated and photo-treated), the contributions of lattice heating and intrinsic field screening must be the same in these dots regardless of their surface condition. In contrast, we find a drastic increase in the coupling strength as a function of surface passivation. These observations rule out lattice heating and field screening as dominant mechanisms for phonon generation in CdSe QDs and suggest a coupling channel that is activated by surface-induced processes.

In Chapter 5, we invoke a piezoelectric coupling mechanism to rationalize these observations. Basically, surface charge trapping causes spatial separation

of electron and hole, thereby creating a non-zero dipole moment in the QD. This charge trapping process, and hence the creation of dipole moment, is found to occur on a sub-picosecond timescale, which is impulsive with respect to the acoustic phonon period of $\sim$ 1.3ps. Due to the piezoelectric nature of CdSe QDs, this impulsive creation of polarization will launch coherent lattice vibrations. The untreated and ZnS-capped CdSe QDs have inefficient surface charge trapping and therefore exhibit weak coupling to phonons, whereas in photo-treated dots surface trapping is extremely efficient and results in an order of magnitude increase in the phonon amplitude. Recent studies have shown that spatial separation of charges can also trigger optical phonons in CdSe QDs [86].

1.7 The mysterious photoproduct

So far, we have seen that the surface of the QD not only has significant implications for the measurement of multiexcitonic processes such as Auger recombination, blinking and CM but also leads to electrostatic effects in the QD (e.g. enhancement of piezoelectric coupling). The common factor in all of these observations is the elusive "photoproduct" that may be formed by irradiating the QD either prior to the experiment or inadvertently by long exposure times during the experiment.

Although the exact chemical nature of the photoproduct still remains unclear, recent experimental studies have shed light on the properties of this photoproduct by measuring its spectroscopic signatures [2, 57, 87–89]. Electric force microscopy (EFM) experiments by Li et al. show charges building up on the surface of CdS-capped CdSe QDs under continuous high energy ($396nm$) illumination over 3 hours [88]. For green excitation ($532nm$), very small charge

build-up is observed over the same timescale. On the other hand, ZnS-capped CdSe did not exhibit any photocharging even after 5 hours of high energy excitation. It is important to note that they found the charge build-up to be reversible over 15 hours, i.e. after turning the laser off for 15 hours, CdSe/CdS QDs return to their original charge-neutral state[f].

The TA measurements from our group are in agreement with the EFM results by Li et al. [2, 87, 88]. In particular, we find that ZnS-capped CdSe QDs exhibit no surface charge trapping even under high energy excitation (Chapter 4). Also, charge trapping rates in core-only CdSe QDs increase with increasing pump photon energy [87]. In addition, the absorption and PL spectra of untreated and photo-treated QDs are spectrally identical 1.5 hours after photo-treatment. This indicates that the effect of irradiation is reversible over the timescale of a couple of hours, and more importantly, there is no change in the energy spectrum of the QD. Time-resolved PL measurements by Nair and Bawendi also show similar trends for photo-treatment effects [89].

From the studies cited above, we can conclude that (*i*) the photo-treatment procedure does not physically alter the dots in an irreversible manner, (*ii*) photo-treated dots are more susceptible to charge trapping on the surface, and (*iii*) high-energy excitation causes a larger degree of photo-treatment as compared to low-energy excitation.

From a chemical perspective, the surface of QDs is basically an organic-inorganic (ligand-QD) interface. Organic ligands attached to the surface of

[f]Aged QDs also exhibit similar spectral and temporal features as photo-treated QDs [29, 90]

inorganic QDs are important for the stabilization of QDs and for their development into more complex structures [91, 92]. The adhesion energy of the ligand to the QD determines the dynamic equilibrium of ligands on the surface. During the growth process, ligands must be able to attach and detach from the growing QDs, so that parts of QD surface are transiently available for growth, while still preventing agglomeration. After the growth process is complete and the QD solution temperature reaches room temperature, ligands are less likely to detach from the QD surface. However, by introducing a competing ligand in the QD solution, a ligand exchange reaction can be still be carried out at room temperature, e.g. replacement of TOPO by pyridine in TOPO-capped CdSe QDs. As pointed out by Yin and Alivisatos, a quantitative description of the mechanism governing the binding of ligands to the surface of the QD is still lacking, and therefore the choice of ligands for QDs remains empirical [92].

In addition to acting as nanostructure stabilizers, surface ligands also significantly affect exciton dynamics in QDs [93–98]. For instance, passivating Selenium dangling bonds on the surface of CdSe QDs (e.g. by using hexadcylamine instead of TOPO) can completely suppress deep-trap emission and enhance emission from the band edge [95,97]. Most recently, recent temperature-dependent PL experiments have also shown that deep-trap emission can be enhanced by reducing the temperature of the system, which adjusts the surface ligand equilibrium [99]. Additionally, pseudopotential calculations by Califano et al. show that the presence of surface states lowers the symmetry of the QD and leads to a mixing of the dark and bright exciton states [96]. This state mixing, in turn decreases the radiative decay lifetime of the dark exciton by

three orders of magnitude. Also, recent theoretical studies, using the time-dependent Kohn-Sham approach, have shown that at high excitation energies, surface ligands can signicantly increase phonon-assisted exciton relaxation in CdSe QD [98]. These predictions are consistent with our observations of additional fast timescales and broad photoinduced absorption in the TA spectra of photo-treated QDs.

In the context of our work, the photo-treatment procedure may have perturbed the dynamic equilibrium of loosely bound ligands due to prolonged irradiation of the QD. The effect of this perturbation was to increase the number of surface trap sites available for charge carriers while maintaining the same QD energy band structure. In the case of CdSe, the surface trap sites are believed to be Selenium dangling bonds that act as hole traps [87, 93, 94]. Also, since lower excitonic states have to overcome a higher barrier to be trapped on the surface, the rate of surface charge trapping increases with increasing exciton energy as observed in the TA, EFM and t-PL measurements in Refs. [87], [88] and [89] respectively.

1.8 Wave function control in nanostructures

Similar to charge localization on the surface of the QD by photo-treatment, one can engineer nanostructures to more precisely control the spatial distribution of carrier wave functions within the nanostructure. Although nanostructures with complex shapes such as tetrapods, octapods, dot-in-a-rod can be fabricated, perhaps the simplest way to achieve wave function control is by manipulation of the QD surface [5, 8, 13, 100, 101]. The most basic example would be CdSe/ZnS QDs; as discussed in Section 1.5, capping CdSe QDs with ZnS shell creates a potential barrier for carriers in the CdSe core and suppresses the

leakage of carrier wave functions into the surface. However, if the bandgap of the capping material is less than that of the core, e.g. in ZnSe/CdSe, carriers are more likely to be localized in the shell. The former configuration refers to a Type-I nanostructure and the latter to inverted Type-I.

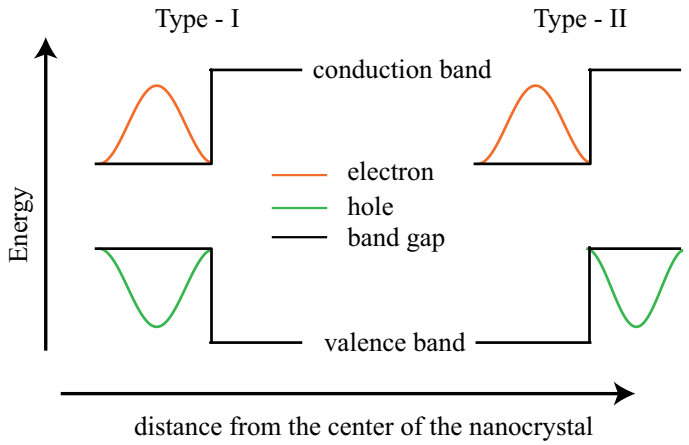

FIGURE 1–6: Illustration of band Type-I and Type-II band configurations and their effect on carrier localization

In Type-I materials, there is a large overlap of the electron and hole wave functions as they are both confined in the same region (either in the core or in the shell), leading to increased quantum yields and fast recombination times. Another configuration, called Type-II refers to the case in which only one (either the conduction or the valence) band sees a higher potential at the core boundary while the other sees a lower potential [5]. This leads to spatial separation of charge carriers: one localized in the core and the other in the shell. Due to the spatial separation of electrons and holes, Type-II QDs result in long exciton lifetimes, useful for extending the time window for charge separation required for photovoltaic applications. The type-II configuration

also leads to repulsive exciton-exciton interactions, thereby reducing the optical gain thresholds [6, 102]. The different localization regimes are compared in Figure 1–6 and Table 1–1.

TABLE 1–1: A comparison between Type-I and Type-II localization regimes in semiconductor QDs

Property	Type-I	Type-II
wave function localization	same spatial region	different spatial regions
electron-hole overlap	large	small
typical quantum yield	high	low
exciton-exciton interaction	attractive	repulsive
exciton lifetime	short	long

One can further increase the functionality of core/shell QDs by adding another layer of semiconductor material on the QD surface. In this configuration, we achieve a core/shell/shell or core/barrier/shell "heteronanostructure". In Chapter 6, we theoretically study electron and hole localization in these heteronanostructures using a two-band effective mass model and first-order perturbation theory. We find that, in addition to the separation of electron and hole in different regions of the nanoparticle, core/barrier/shell nanostructures allow spatial separation of different "excitonic" states. By tuning the material parameters, individual low energy excitons can be localized in either the core or the shell (Type-I localization) or be prepared in a charge-separated state (Type-II).

The control that core/barrier/shell materials offer over single particle wave functions makes them desirable for a wide range of applications. In particular, the dual-color-emitting CdSe/ZnS/CdSe heteronanostructure, first introduced by Peng and co-workers in 2005, has recently become a subject of much interest due to its favorable light emitting properties [7, 9–11, 103].

CdSe/ZnS/CdSe QDs integrated on an InGaN/GaN substrate have been successfully used to produce white-light LEDs [11, 103]. Also, while even the well-passivated CdSe/ZnS core/shell nanostructures show blinking, the dual wavelength emission of CdSe/ZnS/CdSe nanostructures allows them to have periods where the core is "off", but the shell is still "on" [40, 104]. This shortens the overall "off" period of the nanostructure making them useful in fluorescent labeling and imaging applications. Recently, in agreement with the predictions of the model described in Chapter 6, experimental studies from our group have shown that for specific core, barrier and shell dimensions, CdSe/ZnS/CdSe heteronanostructures exhibit a broad bandwidth of optical gain due to emission from spatially separated and long-lived multiexcitonic states [50].

1.9 Thesis overview

Evidently, a good understanding of many-body interactions in semiconductor QDs is essential not only from a fundamental physics perspective but also for potential technological advancements. The theoretical background necessary for a qualitative understanding of multiexcitonic interactions in semiconductor QDs is provided in Chapter 2. Chapter 3 includes the details of a pump-probe spectroscopy experiment designed for the measurement of multiexcitonic processes in QDs.

The results presented in this thesis highlight the sensitivity of multiexciton interactions to their confinement environment, which is largely determined by the surface properties of the nanostructure. This intuitive result is shown to have profound implications for accurate measurements of electronic and

optical properties of QDs. In Chapter 4, we discuss the effects of surface treatment on the measurement Auger processes and CM in CdSe QDs, and the interpretation of pump-probe signals.

In Chapter 5, we investigate the surface-dependence of exciton-phonon interaction in CdSe QDs. These studies reveal an enhanced piezoelectric coupling to phonons due to surface charge trapping. Finally, in Chapter 6, we study the manipulation of charge carrier localization and many-body interactions in core/barrier/shell heteronanostructures as a function of the different material parameters. We find that these heteronanostructures offer excellent control over their electronic and optical properties.

Chapter 2

Theoretical background

In the simplest approximation, excitons in semiconductor nanocrystals (NCs) can be described using a particle-in-a-sphere model. Despite the apparent simplicity of this model, it has been quite successful in qualitatively describing electronic properties of semiconductor NCs since it was first introduced by A.L. Efros and A.L. Efros in 1982 to study interband absorption [105] and L. Brus in 1983 to study ionization potential, electron affinities and transition energies in semiconductor NCs [106]. However, this model ignores significant effects such as valence band mixing, surface imperfections and non-spherical shape of real NCs. The development of advanced theoretical frameworks such as density functional theory, pseudopotential methods, tight-binding approach and multiband $k \cdot p$ model has led to a more precise description of many-body effects in NCs [32,107–109]. A detailed discussion of these theoretical models is beyond the scope of this thesis. In this chapter, we review the effective mass model (based on particle-in-a-sphere approach) that is commonly used for experimental data modeling and to study carrier-carrier interactions in NCs.

2.1 Quantum confinement

When the size of a semiconductor material becomes so small that the charge carriers can feel the material boundaries, they begin to exhibit quantum mechanical effects. This is known as the quantum confinement effect. More precisely, this effect occurs when the radius of the NC becomes comparable to the Bohr radius of the particle (electron, hole or exciton) given by,

$$a_c = \epsilon \frac{m}{m_c} a_B \qquad , \tag{2.1}$$

where ϵ is the dielectric constant of the material, a_B is the Bohr radius of the Hydrogen atom, a_c is the particle Bohr radius, and m and m_c are the electron rest mass and the effective mass of the particle respectively. Given that an exciton is a bound two-particle state consisting of an electron and a hole, we can define three quantum confinement regimes as follows:

1. Weak confinement: $a_{exc} > a > a_e, a_h$
2. Intermediate confinement: $a_e, a_{exc} > a > a_h$ or $a_h, a_{exc} > a > a_e$
3. Strong confinement: $a_e, a_h, a_{exc} > a$

where a is the radius of the NC, and a_e, a_h and a_{exc} are electron, hole and excitonic Bohr radii respectively. For CdSe $a_{exc} = 5.6nm$, therefore the NCs studied in this work ($a < 3nm$) fall in the strong confinement regime. As we will see below, strong confinement approximation allows us to treat the Coulomb interaction as a first order perturbation to the excitonic energy.

2.2 Effective-mass model

As the name suggests, this model is based on the effective mass approximation (EMA). Within EMA, we can ignore the individual atoms in the NC lattice, and treat electrons and holes as free particles with different effective

masses in parabolic energy bands. For a spherical NC of radius a, the potential profile ($V(r)$) can be written as,

$$V(r) = \begin{cases} 0, & 0 < r \leq a. \\ \infty, & r > a. \end{cases} \tag{2.2}$$

Solving the Schrödinger equation, we obtain single particle envelope wave functions[a] and energies as,

$$\Psi_{nlm}(r,\theta,\phi) = C\frac{j_l(\alpha_{nl}r/a)Y_{lm}(\theta,\phi)}{r} \quad , \tag{2.3}$$

$$E_{nl} = \frac{\hbar^2\alpha_{nl}^2}{2ma^2} \quad , \tag{2.4}$$

where C is a constant, j_l is the l^{th} order spherical Bessel function, $Y_{lm}(\theta,\phi)$ are the spherical harmonics, α_{nl} is the n^{th} zero of j_l, m is the particle mass and $\hbar$ is the Planck constant. Equation 2.4 shows that the single particle energy spectrum is quantized and size-dependent (Figure 2–1), and the energy levels can be labeled with quantum numbers n and l, for example, $n = 1$ and $l = 0$ corresponds to the lowest energy $1S$ state. We now extend this approach to two-particle bound states (excitons) in NCs.

Given that the single particle confinement energy is inversely proportional to a^2 (Equation 2.4) and the electron-hole Coulomb interaction goes as $1/a$, in the limit to small NC radius, we can treat electron and hole as independent

[a]This calculation yields only the envelope wave functions. The complete wave function $\Phi_{nlm}(r,\theta,\phi) = \Psi_{nlm}(r,\theta,\phi)u_{nk}(r)$, where u_{nk} is a periodic function with the periodicity of the lattice potential. Assuming a weak k-dependence, in conjunction with the effective mass approximation allows us to ignore u_{nk}.

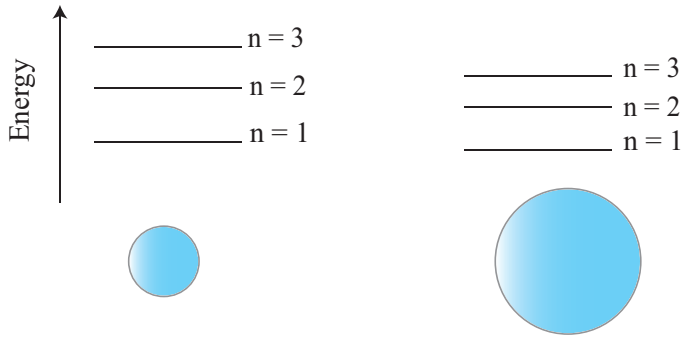

FIGURE 2–1: Effect of quantum confinement in semiconductor nanocrystals.

particles. The Coulomb interaction can be added as a first-order correction to the excitonic energy. This is called the strong confinement approximation. Therefore, we can write excitonic wave function and energy as,

$$\Psi^{exc}_{nlm} = \Psi^{e}_{n_e l_e m_e} \Psi^{h}_{n_e l_e m_e} \tag{2.5}$$

$$E^{exc}_{nl} = E^{e}_{n_e l_e} + E^{h}_{n_h l_h} + E^{c} \quad , \tag{2.6}$$

where Ψ^e and Ψ^h are electron and hole wave functions respectively calculated using Equation 2.3, $E^e_{n_e l_e}$, $E^h_{n_h l_h}$ and E^c are, respectively, the electron, hole and Coulomb energies, and different excitonic states are labeled with quantum numbers n, l, m, with the subscripts $e(h)$ corresponding electron (hole).

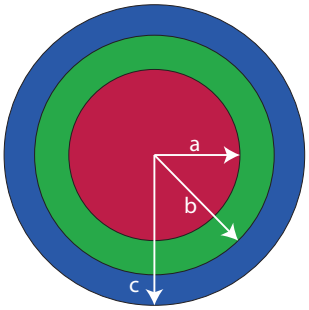

FIGURE 2–2: Schematic of a core/barrier/shell nanosctructure.

This model can also be extended to layered spherical nanostructures, such as core/shell or core/barrier/shell nanostructures. For instance, in the case of a core/barrier/shell nanostructure as shown in Figure 2–2, the potential profile can be written as,

$$V(r) = \begin{cases} 0, & 0 < r \leq a \\ V_b, & a < r \leq b \\ 0, & b < r \leq c \\ \infty, & r > c \end{cases} \tag{2.7}$$

and the excitonic wave functions and energies can be calculated by following the same procedure as for core-only NCs (a single sphere).

2.3 Many-body interactions in nanostructures

As discussed in the preceding section, when the confinement energy of the charge carriers is larger than the interaction energy, the interaction can be treated perturbatively in the effective mass model approach. One can calculate the interaction Hamiltonian by solving the Poisson equation for the desired nanostructure. We use this method to calculate biexciton binding energy in CdSe/ZnS/CdSe nanostructures in Chapter 6. Here, we illustrate these calculations for the simpler case of a core/shell nanostructure. This method can be easily extended to nanostructures with multiple shells.

To begin with, let us consider a sphere of radius a and dielectric constant ϵ_1 surrounded by a shell of thickness $b-a$ and dielectric constant ϵ_2 (Figure 2–3). Due to the different dielectric constants of the core and shell regions, the electron-hole interaction energy will have contributions from both the Coulomb interaction and the induced polarization due to dielectric discontinuity at the

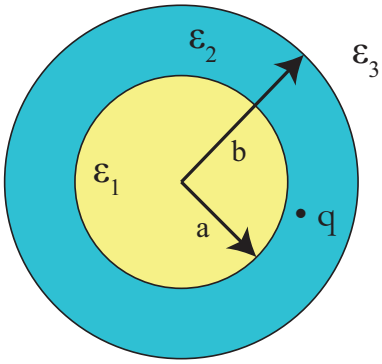

FIGURE 2–3: Schematic of a core/shell nanostructure (core radius a and shell thickness $b-a$) with a point charge q in the shell. ϵ_1, ϵ_2, ϵ_3 are the dielectric constants of core, shell and the surrounding material respectively.

boundaries. To calculate the interaction Hamiltonian (Φ), we solve the Poisson equation ($\nabla^2\Phi = \rho$) to obtain the electric potential in three regions: (i) the core ($r \leq a$) , (ii) the shell ($a < r \leq b$) and, (iii) outside the shell ($r > b$). For a point charge in the shell, we obtain

$$\begin{aligned}
\Phi_1(r,\theta) &= \sum_{n=0}^{\infty} a_n r^n P_n(cos\theta) \\
\Phi_2(r,\theta) &= \sum_{n=0}^{\infty} \left(\frac{q}{4\pi\epsilon_2} \frac{r_<^n}{r_>^{n+1}} + \frac{b_n}{r^{n+1}} + c_n r^n \right) P_n(cos\theta) \\
\Phi_3(r,\theta) &= \sum_{n=0}^{\infty} \frac{g_n}{r^{n+1}} P_n(cos\theta)
\end{aligned} \tag{2.8}$$

where a_n, b_n, c_n and g_n are constants to be determined by boundary conditions, q is the point charge, θ is the angle between the test and the source point charges, $P_n(cos\theta)$ is n^{th} order Legendre polynomial ($n = 0, 1, 2$ for S, P, D excitonic states respectively), Φ_i is the potential in region i with a dielectric constant ϵ_i and $r_{>(<)}$ is $max(min)[r, d]$, d is the location of the source point charge. Applying the following dielectric boundary conditions across the

surface,

$$\begin{aligned} \Phi_i\big|_{r_i} &= \Phi_{i+1}\big|_{r_i} \\ \epsilon_i \frac{\partial \Phi_i}{\partial r}\bigg|_{r_i} &= \epsilon_{i+1} \frac{\partial \Phi_{i+1}}{\partial r}\bigg|_{r_i} \end{aligned} \tag{2.9}$$

we get

$$\begin{aligned} a_n &= \frac{d^{-1-n}(1+2n)(d^{1+2n}(\epsilon_{23})(1+n)+b^{1+2n}(\epsilon_3+(\epsilon_2+\epsilon_3)n))q}{4(a^{1+2n}(\epsilon_{12})(\epsilon_{23})n(1+n)+b^{1+2n}(\epsilon_2+(\epsilon_1+\epsilon_2)n)(\epsilon_3+(\epsilon_2+\epsilon_3)n))\pi} \\ b_n &= -\frac{a^{1+2n}d^{-1-n}(\epsilon_{12})n(d^{1+2n}(\epsilon_{23})(1+n)+b^{1+2n}(\epsilon_3+(\epsilon_2+\epsilon_3)n))q}{4\epsilon_2(a^{1+2n}(\epsilon_{12})(\epsilon_{23})n(1+n)+b^{1+2n}(\epsilon_2+(\epsilon_1+\epsilon_2)n)(\epsilon_3+(\epsilon_2+\epsilon_3)n))\pi} \\ c_n &= \frac{d^{-1-n}(\epsilon_{23})(1+n)\left(-a^{1+2n}(\epsilon_{12})n+d^{1+2n}(\epsilon_2+(\epsilon_1+\epsilon_2)n)\right)q}{4\epsilon_2\left(a^{1+2n}(\epsilon_{12})(\epsilon_{23})n(1+n)+b^{1+2n}(\epsilon_2+(\epsilon_1+\epsilon_2)n)(\epsilon_3+(\epsilon_2+\epsilon_3)n)\right)\pi} \\ g_n &= \frac{b^{1+2n}d^{-1-n}(1+2n)\left(-a^{1+2n}(\epsilon_{12})n+d^{1+2n}(\epsilon_2+(\epsilon_1+\epsilon_2)n)\right)q}{4\left(a^{1+2n}(\epsilon_{12})(\epsilon_{23})n(1+n)+b^{1+2n}(\epsilon_2+(\epsilon_1+\epsilon_2)n)(\epsilon_3+(\epsilon_2+\epsilon_3)n)\right)\pi} \end{aligned} \tag{2.10}$$

where $\epsilon_{23} = \epsilon_2 - \epsilon_3$ and $\epsilon_{12} = \epsilon_1 - \epsilon_2$. At this point, we have obtained the electric potential in a core/shell nanostructure for a point charge in the shell. We again solve the Poisson equation twice (i) for a point charge in the core, and (ii) for a point charge outside the nanostructure ($r > b$). These calculations then give us the complete interaction Hamiltonian ($\hat{\Phi}$) for a core/shell nanostructure. Finally, using the wave functions obtained using the effective mass model as described in Section 2.2, the carrier-carrier interaction energy can be calculated using,

$$E_{12} = \int \mathrm{d}r_2 \int \mathrm{d}r_1 |\Psi_1|^2 \hat{\Phi} |\Psi_2|^2 \quad , \tag{2.11}$$

where the subscripts 1 and 2 refer to the two charge carriers and Ψ_i is the envelope wave function for particle i (i = electron, hole). The biexciton binding

energy (Δ_{XX}) can then be calculated using,

$$\begin{aligned}\Delta_{XX} &= E_{XX} - 2E_X \\ &= (2E_e + 2E_h + E_{ee} + E_{hh} + 4E_{eh}) - 2(E_e + e_h + E_{eh}) \\ &= E_{ee} + E_{hh} - 2E_{eh} \end{aligned} \tag{2.12}$$

The results of these calculations and their implications for optical and electronic properties of for core/barrier/shell nanostructures are discussed in detail in Chapter 6.

2.4 CdSe **nanocrystals**

In Section 2.2, we showed that with a few approximations, a simple particle-in-a-sphere approach can be used to study excitons in NCs. We now apply the results of this model to the material of interest in this work, i.e. CdSe NCs. Specifically, we are interested in the lowest excitonic state in these NCs.

In CdSe, the conduction band is composed of $5s$ electrons from Cadmium atoms and the valence band consists of Selenium $4p$ holes. Therefore, the azimuthal quantum numbers due to the atomic basis are $l_e = 0$ and $l_h = 1$ for electrons and holes respectively. Due to spin-orbit coupling, the valence band degeneracy is broken and it splits into $j_{h1} = l + s = 3/2$ and $j_{h2} = l - s = 1/2$. Due to the crystal field of the hexagonal lattice, the valence band further splits into $j = \pm 3/2$ (heavy-hole) and and $j = \pm 1/2$ (light-hole) subbands. The total quantum number for an excitonic state will have contributions from the atomic basis as well as the envelope function. For the lowest energy exciton (1S exciton), the envelope function contribution is $L_e = L_h = 0$. Therefore, we can write the total quantum number for 1S exciton as, $F = F_h + F_e =$

$(l_h + s + L_h) + (l_e + s + L_e) = 2$. The common notation used to label this excitonic state is $1S_{1/2}1S_{3/2}$, where the first part corresponds to the electron $(n_e L_e)_{F_e}$ and the second to the hole $(n_h L_h)_{F_h}$. Since $F = 2$, 1S exciton is expected to be eight-fold degenerate. However, this degeneracy is lifted due to crystal field splitting, non-spherical shape of the NC and strong electron-hole interaction, and the lowest energy bright excitonic state ends up being two-fold degenerate (Figure 2–4). This is called the "fine structure" of the exciton.

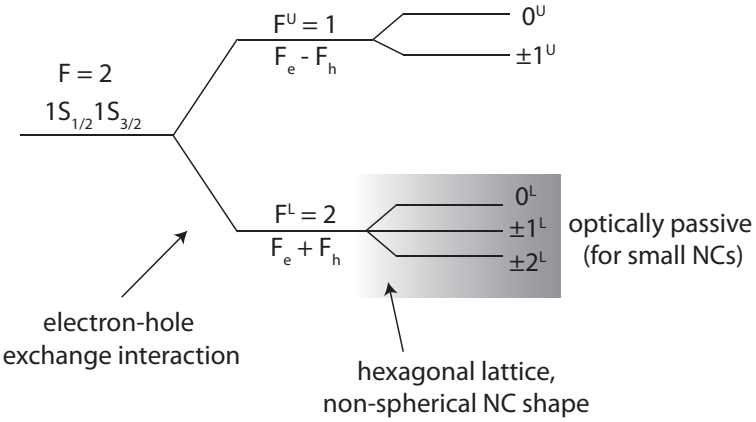

FIGURE 2–4: Degeneracy breaking in CdSe NCs. Due to strong electron-hole exchange interaction , the eight-fold degenerate 1S exciton is split into a five-fold degenerate $F_e + F_h = 2$ state and a three-fold $F_e - F_h = 1$ state. Subscripts U and L are used to distinguish between the high energy (upper-level) and low energy (lower level) states with the same magnitude of the projection of angular momentum.

As calculated by Efros et al. [110], the $\pm 2^L$ state is optically passive because the absorbed or emitted photons cannot have an angular momentum

projection of ± 2 [b]. They also find that the probability of optical transitions to 0^L state is zero for all NC sizes and decreases with decreasing size for $\pm 1^L$. Essentially, for small NCs, the lower manifold of states arising from five-fold degenerate F^L is optically passive whereas that arising from F^U is optically bright. Therefore, the lowest energy "bright" exciton in CdSe NCs is two-fold degenerate.

The degeneracy of the 1S exciton is extremely important in interpreting the data presented in Chapter 4. As discussed in Chapter 3, the pump-probe signal (ΔOD) is directly proportional to the population of the probed state; therefore the observed magnitude of ΔOD for 1S probe will be limited by the degeneracy of the 1S state. This topic will be discussed in detail in Chapter 4 in the context of multiexciton recombination and multiexciton generation processes.

[b]Although, emission from $\pm 2^L$ is optically forbidden, radiative recombination of this state can occur either via thermal activation to the lowest optically allowed state or through longitudinal optical phonon-assisted transitions, where the phonon carries the extra unit of momentum.

Chapter 3

Experimental methods

Optical spectroscopy is the study of light-matter interactions. There are multiple ways in which light can interact with matter, for example, the interaction can be absorptive or emissive, linear or nonlinear, elastic or inelastic, coherent or incoherent. One can obtain a wealth of information about a material from the way it interacts with light, such as energy spectrum of the material, coupling between transitions, lattice vibrations etc. In the experiments presented in this thesis, the material of interest is CdSe quantum dots (QDs) and the spectrocopic technique used is pump-probe spectroscopy. This chapter presents the details of our experiment and the nonlinear processes involved the generation and characterization of femtosecond pulses.

3.1 Pump-probe Spectroscopy

Pump-probe spectroscopy, also known as transient absorption (TA) spectroscopy, is a third-order nonlinear spectroscopic technique, which employs two light pulses (called "pump" and "probe") to measure the nonlinear response of a system. Like other nonlinear techniques, pump-probe spectroscopy can be described using third-order time-dependent perturbation theory; however,

the interpretation of pump-probe data generally does not require invoking the detailed theoretical formalism of nonlinear spectroscopy. In a pump-probe experiment, a pump pulse perturbs the sample at time $t = 0$ and a time delayed probe pulse measures the absorption change (ΔOD) produced by the pump pulse (Figure 3–1).

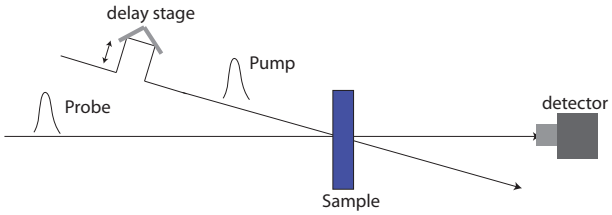

FIGURE 3–1: Schematic illustration of a pump-probe spectroscopy experiment.

The measured signal can be written as,

$$\Delta OD = OD_{pump-on} - OD_{pump-off} \quad , \tag{3.1}$$

where $OD_{pump-on}$ and $OD_{pump-off}$ refer to the optical density of the sample measured with and without a pump pulse interaction respectively. For a sample with an extinction coefficient ϵ, concentration C, length l, and transmitted and incident light intensities of I_{tr} and I_{in}, Beer's law states that $OD = -\log\left(\frac{I_{tr}}{I_{in}}\right) = \epsilon C l$. In a pump probe experiment, the detector measures the intensity of the transmitted probe pulse, therefore, for a pump-probe time delay τ and probe wavelength λ, Equation 3.1 can be written as

$$\Delta OD(\tau, \lambda) = -\log\left(\frac{I_{pump-on}}{I_{pump-off}}\right) \quad , \tag{3.2}$$

where $I_{pump-on}$ and $I_{pump-off}$ are the transmitted probe intensities in the presence and absence of a pump pulse respectively.

If there is an increase in transmitted probe intensity after pump perturbation, for example due to ground state bleaching or stimulated emission, ΔOD is negative. In the case of excited state absorption, $I_{pump-on} < I_{pump-off}$ and ΔOD is greater than zero. By scanning τ and λ, we can obtain both temporal and spectral responses of the system respectively. In the former case, we obtain ΔOD as a function of time, also called a ΔOD "transient" and in the latter case, the measured signal is called a "transient absorption spectrum". In our experiments, we measure both transients as well as TA spectra to study temporal and spectral dynamics of charge carriers in QDs.

3.2 Experiment

The experiments presented in this thesis were performed using an amplified Ti-Sapphire laser system (2.5 mJ, 70 fs, 800 nm, 1 kHz). The pump pulse was derived by second harmonic generation (SHG) of the 800 nm output in a 0.1 mm thick β-barium borate (BBO) crystal. The probe pulse was obtained by single filament white light generation in a 2 mm sapphire crystal. Both the pump and the probe pulses were compressed using fused silica prism pairs yielding an instrument response function of $\sim$ 100 fs. We briefly describe below the nonlinear processes involved in the generation and characterization of pump and probe pulses.

3.3 Second Harmonic Generation

SHG is a second-order nonlinear process in which two photons of frequency ω combine to create a photon of frequency of 2ω. SHG is actually a special case of sum-frequency generation where two photons of frequencies ω_a and ω_b combine to produce a sum-frequency photon at $\omega = \omega_a + \omega_b$ (Figure 3–2). In

our experiments, we use the SHG process to generate a 400 nm pump pulse from 800 nm output of the regenerative amplifier. SHG is also used to measure the time-duration of ultrafast pulses via auto-correlation (Section 3.6).

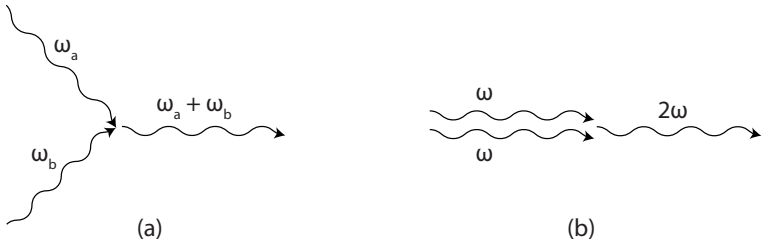

FIGURE 3–2: Schematic illustration of second-order nonlinear processes: (a) Sum frequency generation, and (b) Second harmonic generation.

In systems with inversion symmetry, the second order susceptibility $\chi^{(2)} = 0$ and therefore, SHG is not possible. However, SHG can still be observed on the surface of centrosymmetric crystals, where electrons feel the non-centrosymmetry (inside/outside) of the surface. For our purposes, we use a β-BBO crystal ($\chi^{(2)} \neq 0$)as the nonlinear medium for SHG.

A detailed derivation of SHG can be found in standard texts on nonlinear optics, for example Ref. [111]. Here, we highlight salient results that are relevant to the experimental understanding of this process. For the general case of sum-frequency generation, the intensity of the sum-frequency photon is given by

$$I_c \sim \frac{l^2 I_a I_b \sin^2(\Delta k l/2)}{(\Delta k l/2)^2} \quad , \tag{3.3}$$

where l is the thickness of the nonlinear crystal, I_a and I_b are the intensities of the incident photons with frequencies ω_a and ω_b respectively, I_c is the intensity of the SFG photon that has a frequency ω_c, and $\Delta k = k_c - k_b - k_a$ with k_i being the wave vector of photon 'i'. Equation 3.3 shows that the maximum

SFG intensity is obtained when $\Delta k = 0$; this is called the "phase-matching" condition.

For SHG, $\omega_a = \omega_b = \omega$, $\omega_c = 2\omega$, $k_a = k_b = k = \omega n/c$ and $k_c = 2\omega n_c/c$, where n and n_c are the refractive indices of the incident and SHG photons respectively. Therefore, to satisfy the phase matching condition, we must have $n_c = n$. Since the frequency of the SHG photon is twice that of the incident photon, we must use Group-II crystals (crystals with a unique crystallographic axis) in order to meet the phase matching condition. A negative uniaxial crystal (such as β-BBO) has a unique optical axis and has a higher effective refractive index along the "ordinary" axis as compared to the "extraordinary" axis ($n_o > n_e$) (Figure 3–3). In fact, for a negative uniaxial crystal

$$\frac{1}{n_e(\theta)^2} = \frac{\cos^2\theta}{n_0^2} + \frac{\sin^2\theta}{n_e^2} \qquad , \tag{3.4}$$

where θ is the angle between the wave vector k and the optical axis. Equation 3.4 shows that if the low-frequency incident wave travels along the ordinary axis and the SHG wave travels along the extraordinary axis, we can achieve the phase-matching condition by tuning the angle of the crystal with respect to the incoming beam such that $n_e(\theta)^{2\omega} = n_0^{\omega}$ or in order words, $n_c = n$ (Figure 3–3).

Polarization of the fundamental and second harmonic waves: If the polarization direction of both the waves is the same i.e. both travel as ordinary or extraordinary rays, then $n(2\omega) > n(\omega)$ and phase matching would never be achieved, therefore, the rays have to be orthogonally polarized. In beta barium borate, which is a negative uniaxial crystal, the fundamental propagated as an o-ray and the second harmonic travels as an e-ray.

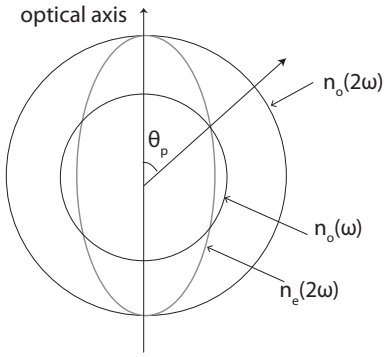

FIGURE 3–3: Phase matching in a negative uniaxial crystal. θ_p is the phase matching angle where $n_e(\theta)^{2\omega} = n_0^{\omega}$.

3.4 Self-phase Modulation

The modulation of the phase of a propagating pulse due to the temporal profile of the pulse itself is called self-phase modulation (SPM). In our experiments, we use SPM for white light generation, which is then used as the probe pulse. For a light pulse with time-dependent intensity envelope $I(t)$, the effective refractive index of a material can be written as

$$n(t) = n_0 + n_2 I(t) \tag{3.5}$$

where n_0 is the linear (or time independent) part of refractive index and n_2 if the nonlinear part of the n. Now, let us consider a light pulse propagating through a medium along z-direction; the electric field of the pulse can be expressed as

$$\begin{aligned} E(z,t) &= E(t)e^{\iota kz - \iota\omega_0 t} \\ &= E(t)e^{\frac{\iota\omega_0 nz}{c} - \iota\omega_0 t} \end{aligned} \tag{3.6}$$

where E(t) is time- varying amplitude of electric field with frequency ω_0 and wave vector k, and c is the speed of light. Assuming that the nonlinear medium

responds instantaneously to the the pulse intensity, the phase of the propagating pulse $\Phi(t)$ can be written as

$$\begin{aligned}\Phi(t) &= \frac{\omega_0 n z}{c} - \omega_0 t \\ &= \frac{\omega_0 n_2 I(t) z}{c} - \omega_0 t + \frac{\omega_0 n_0 z}{c}\end{aligned} \tag{3.7}$$

The instantaneous frequency can be written as time-derivative of the phase,i.e.,

$$\omega(t) = \omega_0 - \frac{\omega_0 n_2 z}{c}\frac{dI}{dt} \tag{3.8}$$

Equation 3.8 shows that the spectral broadening of a pulse depends on n_2, z and $\frac{dI}{dt}$. Therefore, a thick material with large n_2 and a short intense pulse are desirable to have a broad spectrum.

In our experiments, we use a 2mm thick sapphire crystal for white light generation from 800nm output of the regenerative amplifier. For Gaussian pulses in media with $n_2 > 0$, the leading edge of the pulse is shifted to lower frequencies and the trailing edge is shifted to higher frequencies (Figure 3–4).

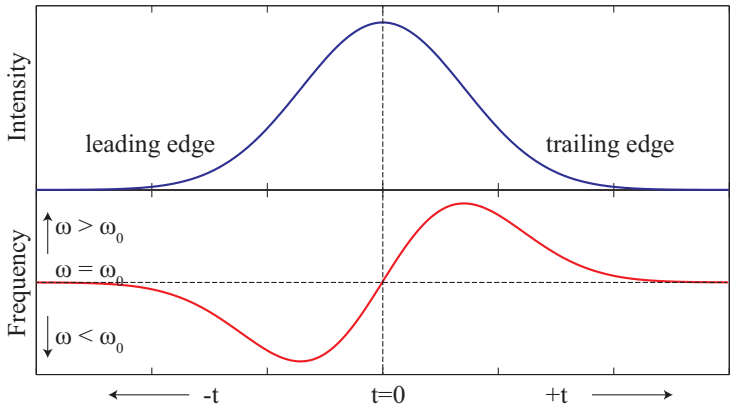

FIGURE 3–4: Self-phase modulation of a gaussian pulse

3.5 Pulse compression

In a dispersive medium, different frequencies travel with different velocities, which leads to broadening of optical pulses with multiple frequency components. This temporal spreading of the pulse is also known as group velocity dispersion (GVD). The velocity at which each phase component travels is called the phase velocity ($v_p = \omega/k = c/n(\lambda)$), and the pulse envelope as a whole travels at group velocity ($v_g = d\omega/dk$). We can obtain the relationship between v_g and v_p as follows:

$$\begin{aligned} v_g &= \frac{d\omega}{dk} \\ &= v_p + \frac{dv_p}{dk} \\ &= v_p\big(1 - \frac{1}{n}\frac{dn}{dk}\big) \end{aligned} \tag{3.9}$$

In the case of normal dispersion, i.e. $\dfrac{dn}{dk} > 0$, long wavelengths travel faster than short wavelengths and therefore $v_g < v_p$ and the optical pulse acquires positive GVD. For anomalous dispersion, on the other hand, $\dfrac{dn}{dk} > 0$ and the GVD is negative. For non-dispersive media, $\dfrac{dn}{dk} = 0$ and $v_g = v_p$. However, all media have a finite dispersion, so one has to inevitably deal with pulse compression in ultrafast experiments. GVD causes the pulse phase to vary quadratically with frequency. We can understand this by simply Taylor expanding the wave vector ($k(\omega)$) around a center frequency ω_0,

$$k(\omega) = k_0 + \frac{\partial k}{\partial \omega}(\omega - \omega_0) + \frac{\partial^2 k}{\partial \omega^2}\frac{(\omega - \omega_0)^2}{2!} + ... \tag{3.10}$$

Since the pulse propagation is determined by $e^{-\iota k(\omega) z}$, it is clear that the second term $\dfrac{\partial k}{\partial \omega} = \dfrac{1}{v_g}$ varies linearly with frequency and adds a delay to the pulse.

The third term varies quadratically with frequency and introduces a frequency-dependent delay, temporally modifying the pulse. The fourth term is called the third order dispersion.

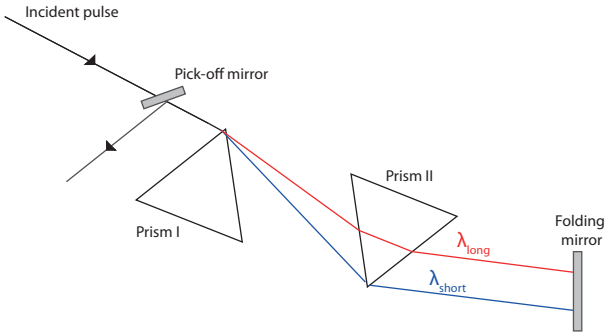

FIGURE 3–5: Schematic illustration of a prism compressor

As discussed above, in normally dispersive media, the optical pulse acquires a positive GVD. To correct for positive GVD, we must use a device that imparts negative GVD to the pulse. We accomplish this using a pair of Brewster cut prisms in the arrangement shown in Figure 3–5. This optical device is called a prism compressor. In this configuration, longer wavelengths are made to traverse more glass, thereby adding negative GVD to the pulse. The first prism disperses the incident beam, the second prism collimates the beam and after reflecting back from the folding mirror, the action of the two prisms is reversed so that the compressed and incident beams are spatially identical. The compressed pulse is slightly vertically displaced with respect to the incident pulse and is picked off by a mirror. It is also possible to use use four prisms in the compressor instead of using a folding mirror.

Generally, prism compressors utilize Brewster cut prisms, i.e. for these prisms, Brewster angle is equal to the angle of minimum deviation. An advantage of having Brewster cut prisms is that when the incident beam enters

at Brewster angle, we can change the amount of negative GVD produced by the second prism by translating it into the beam without changing the beam pointing[a].

3.6 Pulse characterization: Autocorrelation

Detectors (e.g. photodiodes, photomultiplier tubes etc.) have very slow rise and decay times (on the order of a nanosecond) which makes it impossible to electronically measure the time duration of a femtosecond pulse. One can overcome this constraint by using the technique of "autocorrelation". Autocorrelation involves overlapping a femtosecond pulse with a time-delayed replica of itself and sampling the degree of overlap (energy of the SHG photon) as a function of the time delay between the two pulses. We can scan the time delay in femtosecond time steps ($1ps = 300\mu m$) and therefore, extract the temporal width of an ultrafast pulse from the overlap function.

An autocorrelator uses a nonlinear crystal for SHG of the femtosecond pulse and a photodiode to measure the energy of SHG pulse. Mathematically, autocorrelation of a function f is expressed as

$$\begin{aligned} R_f &= \int_{-\infty}^{\infty} f(\tau) f(\tau - t) d\tau \\ &= \int_{-\infty}^{\infty} f(\tau) f(\tau + t) d\tau \end{aligned} \tag{3.11}$$

[a]Prism compressors are great for correcting group velocity dispersion; however, they do not compensate for third order dispersion. Since the third-order dispersion of prisms and gratings have opposite signs, they can be used together to produce ultrashort pulses.

Broadly speaking, autocorrelation can be implemented in the following two configurations:

1. Noncollinear autocorrelation (also called intensity autocorrelation)
2. Collinear autocorrelation (also called interferometric autocorrelation)

We discuss these two approaches below; however, we exclusively used the former configuration for the characterization of pulses used in our experiments.

3.6.1 Intensity autocorrelation

In intensity autocorrelation, the two pulses (i.e. the pulse to be measured and its replica) are noncollinear and are focused on a thin SHG crystal (Figure 3–6). The total field incident on the crystal is $E(t) + E(t+\tau)$, where τ is the time delay between the two pulses. As a result of frequency doubling in the SHG crystal, the emitted signal field intensity is given by (Section 3.3)

$$\begin{aligned} I_{2\omega} &\sim |\chi^{(2)}|^2 |(E(t) + E(t+\tau))^2|^2 \\ &\sim |\chi^{(2)}|^2 |E(t)^2 + E(t+\tau)^2 + 2E(t)E(t+\tau)|^2 \quad , \end{aligned} \tag{3.12}$$

where $\chi^{(2)}$ is the second-order susceptibility of the crystal. By measuring the intensity of the middle beam, we select only the cross term in Equation 3.12 and eliminate the background due to SHG of the individual pulses. The signal

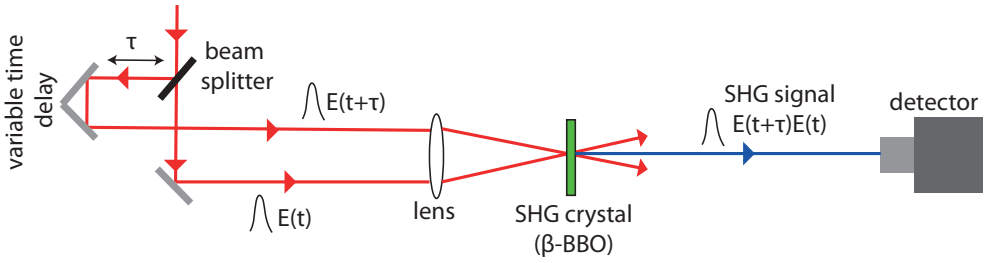

FIGURE 3–6: Intensity autocorrelation.

measured by the detector ($S_{2\omega}$) is the time-integral of $I_{2\omega}$, i.e.

$$\begin{aligned} S_{2\omega} &= \int I_{2\omega}(t,\tau)\mathrm{d}t \\ &\sim \int I(t)I(t+\tau)\mathrm{d}t \end{aligned} \tag{3.13}$$

Equation 3.13 implies that the measured signal is an autocorrelation of the intensity envelope of the pulse. For a pulse with a Gaussian intensity envelope, the full width at half maximum (FWHM) of the autocorrelation is $\sqrt{2}$ times the FWHM of the incident pulse (i.e. $\tau_{pulse} = 1/\sqrt{2} \times \tau_{autocorr}$). Similarly, one can calculate pulse widths for different pulse shapes using autocorrelation.

3.6.2 Interferometric autocorrelation

In interferometric autocorrelation, the three terms in Equation 3.12 are spatially overlapped using a collinear arrangement. After the nonlinear crystal, a filter is used to block the fundamental frequency (ω) and transmit the second harmonic beam (2ω). Since the three terms are collinear, this is not a background-free measurement. The measured signal field intensity has contributions from the SHG of individual pulses in addition to the cross-term. Expanding Equation 3.12 and retaining all the terms, we can write the time integrated intensity as

$$\begin{aligned} S_{2\omega}(\tau = 0) &\sim 16 \int |E(t)|^4 \mathrm{d}t \\ S_{2\omega}(\tau = \pm\infty) &\sim 2 \int |E(t)|^4 \mathrm{d}t \end{aligned} \tag{3.14}$$

Therefore, the ratio of the peak of the measured signal (at $\tau = 0$) to the background signal (at $\tau = \pm\infty$) is equal to 8.

A brief comparison of intensity and interferometric autocorrelation

The 8 : 1 ratio in interferometric autocorrelation serves as a check that the SHG signal is purely due to the autocorrelation of the desired pulse and is artifact-free. This configuration also minimizes temporal distortions due to the collinearity of the pulses. The main advantage of intensity autocorrelation is that it is background free and therefore, it is easier to check the presence of any satellite pulses.

'When you have eliminated all which is impossible, then whatever remains, however improbable, must be the truth.'
- Sherlock Holmes

Chapter 4

Surface effects on multiexciton generation and multiexciton recombination signals

In this chapter, we investigate multiexciton recombination (MER) and multiexciton generation (MEG) processes in semiconductor quantum dots (QDs) using transient absorption (TA) spectroscopy. We further study the effect of surface passivation on the spectral signatures of these two processes. Our experiments reveal that surface-induced charge trapping effects give rise to artifactual TA signals that overlap with state-filling signals and complicate the measurement of the desired parameters, i.e. MER times and MEG yields. Finally, we suggest ways to identify the presence of these spurious signals from the measured TA spectra. Also, we show that capping CdSe QDs with a ZnS shell minimizes surface-induced effects and gives the true measure of MER and MEG processes.

4.1 Introduction

Semiconductor QDs have been under intense investigation in order to explore their unique optical and electronic properties as well as their potential technological applications [1,15,25,45,112]. Two processes that bear relevance to QD applications in photovoltaics and lasers are (*i*) MER [29,45,46,113,114] and (*ii*) the reverse process of MEG [51–53, 56–59, 63, 115].

In the MER process, two low energy excitons non-radiatively recombine to produce one high energy exciton, which then undergoes exciton cooling [45,46, 114]. The MER process bears relevance to QD devices in that the MER times determine the timescale for optical gain in lasers [25, 47, 48, 102] as well as for extraction of multiexcitons [116–119], an important issue in QD photovoltaics (PV). MER is also expected to be a key feature which drives blinking in single dot photoluminescence experiments [120]. The MER process is believed to proceed via confinement enhanced Auger recombination processes. However there are recent experiments by Bawendi and Guyot-Sionnest which call into question the extent to which these processes are understood [14, 38, 39, 113].

The MER experiment also bears relevance to MEG in that the established methods of MER analysis are commonly used to quantify the less well established MEG process [45, 46, 57, 60]. The process of generating multiple electron-hole pairs via absorption of a single photon, called MEG or carrier multiplication (CM) [51–53, 56–59, 63, 115, 121], has received particular attention for its applications in photovoltaic devices. In bulk semiconductors, this MEG process is inefficient and limits the conversion efficiency of conventional solar cells. By virtue of quantum confinement effects, QDs are expected to exhibit enhanced MEG yields [52, 59, 122, 123].

This expectation led to extensive studies of the MEG process in QDs with different sizes and compositions. MEG yields of up to 700% [54] and 165% [52] have been reported in PbSe and CdSe QDs respectively. In contrast to these results, recent experimental studies have reported a diminished and even absence of MEG in QDs, casting doubt on the existence or efficiency of this process [56–61]. Finally, for efficient MEG to be useful, it is important to be able to utilize the photo-generated charge carriers before they recombine. Slow MER is therefore desirable for photovoltaic applications of QDs. Accurate determination of MER times and MEG yields is crucial in gauging the usefulness of QDs in photovoltaic devices [45, 59].

Femtosecond pump/probe TA measurements are commonly used to measure the recombination time of multiexcitons [29,45,46,113,114] and the MEG yields in semiconductor QDs [45, 46, 57]. A pump pulse creates an initial (multi)exciton population. These multiexcitons are proposed to decay non-radiatively via Auger recombination process on a $10 - 100$ ps time scale, and the QD is left with a single exciton (X) which decays on a nanosecond time scale.

These decay processes are spectroscopically identified based on an understanding of the pump induced optical nonlinearities in these QDs [25,30,46,87, 124]. The amplitude of the lowest absorption peak (1S peak) changes due to state filling. Since this change in absorption (ΔOD_{1S}) is proportional to the population of the 1S state, time-resolved measurements ΔOD_{1S} can be used to monitor MER processes (Figure 4–1), and extract MEG yields and MER times. Using this method, recombination times of up to 4 excitons have been reported in the case of CdSe QDs [29].

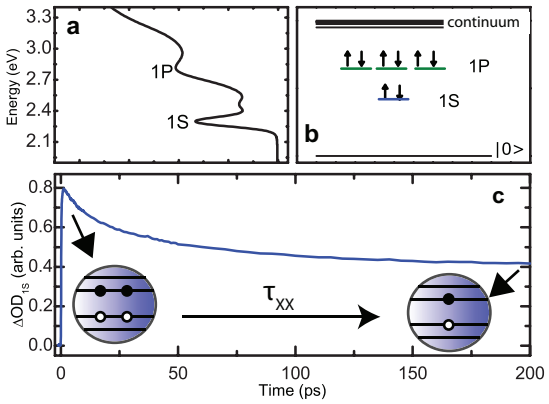

FIGURE 4–1: (a) Linear absorption spectrum of colloidal CdSe QDs with band edge exciton ($1S$) at 2.3 eV. The excitonic energy levels appear as peaks in the absorption spectrum. (b) Schematic level structure. The lowest excitonic state is labeled $1S$ and is two-fold degenerate. (c) The absorption bleaching of the $1S$ peak (ΔOD_{1S}) as a function of time, following hot carrier relaxation. The bleach recovery on this timescale is due to MER. The magnitude of the absorption change is proportional to the population of the $1S$ state. Reprinted with permission from [Tyagi, P. and Kambhampati, P., J. Chem. Phys. 2011, 134, 094706]. Copyright 2011, American Institute of Physics.

In this work, we show that the TA methods commonly used to study MER and MEG are subject to significant artifactual signals which arise from surface charge trapping. In the case of MER, these signals yield quantitatively incorrect measurement of recombination times and even qualitatively incorrect determination of the processes that are observed. In the case of MEG, these false signals result in an incorrect measurement of the critical yet elusive MEG yield. To illustrate, these experiments suggest a significant (170%) MEG yield under conditions in which MEG is forbidden by energy conservation ($E_{pump} \sim 1.35E_g$). These assignments were made by recognizing additional features in the TA spectra as signatures of surface trapping. The surface-induced processes manifest as positive photoinduced absorption (PA) which obscures the negative bleach signals due to state-filling. The overlap of these features

gives rise to false MEG and MER signals. Our experiments identify the physical origin of these false signals. In particular, we find that surface-induced changes in optical selection rules and charge trapping processes lead to false measurement of these signals. We show that well-passivated CdSe/ZnS dots recover the idealized, artifact-free response. We also find that the number of MER timescales that can be extracted from TA experiments is limited by the degeneracy of the probed state. These findings call into question the physical meaning of timescales previously extracted from ΔOD_{1S} in CdSe QDs, and reported to be MER times for $N > 2$ excitons. Finally, the surface polarized excitons due to charge trapping are suggested as the dark state in single dot blinking experiments.

4.2 Experimental Methods

The femtosecond spectroscopic technique used here was described in detail in our prior works [1,24,25,30,47,48,83,84,87,125–128]. The spectroscopic measurements were made using an amplified Ti-Sapphire laser system (2.5 mJ, 70 fs, 800 nm, 1 kHz). The pump pulse was derived by the second harmonic generation of the 800 nm output in a 0.1 mm thick β-barium borate (BBO) crystal. The probe pulses were obtained by single filament white light generation in a 2 mm sapphire crystal. Both the pump and the probe pulses were compressed using fused silica prism pairs yielding an instrument response function of $\sim$ 100 fs. Spot sizes were $\sim 200\mu m$ and $\sim 70\mu m$ for pump and probe pulses respectively.

Samples of colloidal CdSe and CdSe/ZnS QDs dispersed in toluene were purchased from NN-Laboratories. The dots showed no deep trap emission at 295 K. Experiments were performed on colloidal CdSe QDs with band

edge at 547 nm ($R \sim 1.5nm$) with three surface classifications labeled as (i) photo-treated, (ii) untreated, and (iii) capped. The "phototreated dots were prepared by irradiating the sample with intense ($\sim 2.8\mu J/pulse$ at $500Hz$) $3.10eV$ radiation for ~ 100 minutes prior to the experiment. Prolonged irradiation alters the surface of these dots such that they undergo efficient surface trapping [1, 87]. The sample was not flowed while performing experiments on these photo-treated dots. The photo-treatment procedure was reversible on the timescale of hours, with little change to the absorption or emission spectrum as previously described [1]. Further details of the preparation and characterization of phototreated dots can be found in our prior work [1]. The untreated dots refer to the dots that were not irradiated prior to the experiment and were measured in a flow cell at short exposure times. The capped dots have a passivating ZnS shell.

4.3 Results and Discussion

4.3.1 Surface dependence of bleach dynamics

In our experiments, the excitation pulse was tuned to 400 nm to access the continuum of states and the change in the absorption of the 1S peak (ΔOD_{1S}) was measured as a function of the time delay between the pump and the probe pulses [46, 124, 129]. Since ΔOD_{1S} is proportional to the population of the two-fold degenerate 1S state, one can write,

$$\left(\frac{\Delta OD(t)}{OD_0}\right)_{1S} \propto \langle N(t)\rangle \tag{4.1}$$

where, OD_0 is the optical density of the sample. Therefore, a time-resolved measurement of the ground state (1S) bleach can be used to extract the population dynamics of the 1S state (Figure 4–1c). The late time magnitude of

the bleaching signal of the band edge exciton (the B1 feature in the notation of Klimov [25, 30, 46, 87, 124, 130]) is due to the long-lived single exciton and the early time magnitude reflects the number of excitons initially created by the excitation pulse.

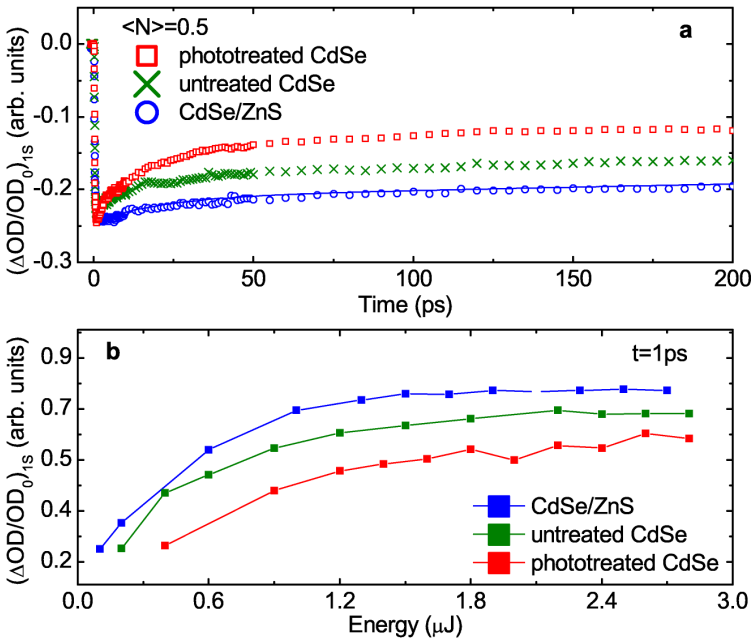

FIGURE 4–2: Deviations from the idealized behavior for different surface conditions. The capped dots best approximate idealized response. (a) Low fluence ($\langle N \rangle$=0.5) ground state bleaching signal for ZnS-capped, untreated and phototreated CdSe QDs. The capped dots show a slow decay component due to X and a fast decay component due to XX, fitting well to a biexponential decay (dashed line). In the phototreated and untreated dots fast time scales of large amplitude appear due other surface-induced processes. (b) Fractional ground state bleach as a function of incident fluence for the three systems at $t = 1$ ps. The bleach saturates at 0.6, 0.7 and 0.8 for phototreated, untreated and capped CdSe QDs respectively. Reprinted with permission from [Tyagi, P. and Kambhampati, P., J. Chem. Phys. 2011, 134, 094706]. Copyright 2011, American Institute of Physics.

We study the population dynamics of CdSe QDs for the three surface passivations described in Section 4.2. Our recent work on piezoelectric coupling in QDs has shown how different surface conditions can affect experimental signatures such as coherent phonon oscillation amplitudes and the spectral features in the TA spectrum [1]. Here, we study the effect of surface passivation on MER dynamics.

Figure 4–2a shows that the $B1$ transients for the three systems are markedly different under identical excitation conditions ($\langle N \rangle = 0.5$). Based on the Poisson distribution of the QD population, the $\langle N \rangle = 0.5$ transient should have a major contribution from single excitons (X) and a small contribution from biexcitons (XX). Therefore, these transients are fit to a bi-exponential function to extract the X and XX recombination times. In the case of CdSe/ZnS we obtain recombination times of $\tau_X = 2.97ns$ and $\tau_{XX} = 28.5ps$, completely consistent with earlier work [29, 113]. Importantly, the ratio of the amplitudes ($\frac{A_{XX}}{A_X}$) is equal to that predicted by the Poisson distribution for $\langle N \rangle = 0.5$. This implies that ΔOD_{1S} in capped dots is free from any artifactual signals and can be described by a set of coupled rate equations discussed in Section 4.3.3. In contrast, additional time constants of significant amplitude appear in phototreated dots leading to a poor fit to a biexponential function. These time scales arise due to the surface-induced processes that come into play in these phototreated dots, as discussed in detail in the following sections.

Another observable related to the surface quality of the dots is the saturation value of the bleach. Figure 4–2b shows the saturation of the bleach as a function of fluence. The capped dots approach the saturation due to state filling ($\frac{\Delta OD}{OD_0} = 1$) more closely than the untreated and phototreated

dots. Hence, the ZnS-capped dots will be considered to represent an idealized response. It has previously been shown that smaller QDs show a greater deviation from the saturation value [43, 46–48, 124, 129, 131]. We find that the fractional bleaching deviates from the saturation response also based on surface induced processes such as charge trapping and excited state absorption (ESA) (Figure 4–2b). These processes manifest as a large positive PA which obscures the negative state filling signals as discussed below.

4.3.2 Signatures of surface induced processes in semiconductor quantum dots

The processes giving rise to different bleach dynamics, and subsequently different MER and MEG signals, in the three systems (capped, untreated and phototreated QDs) can be understood based on their TA spectra [1]. The various contributions to the optical nonlinearities in QDs have been discussed in detail by Klimov [45, 46, 124]. The key spectral feature in these studies is the PA which generically arises from ESA.

In the case of molecules, ESA arises from absorption from the first excited state to higher excited states (e.g. $S1 \rightarrow S2$). In the case of QDs, there are two commonly discussed sources of ESA. The first is absorption from a single exciton to a multiexciton (e.g. biexciton) state [25, 30, 46, 87, 124, 125]. The second is intra-excitonic absorption (e.g. $1S \rightarrow 1P$) from a low energy exciton state to a high energy exciton state [132–136]. Depending on the initial and final excitonic states, this absorption can either be in the infrared or visible spectral range. In this paper, we will focus on the PA features in the visible regime.

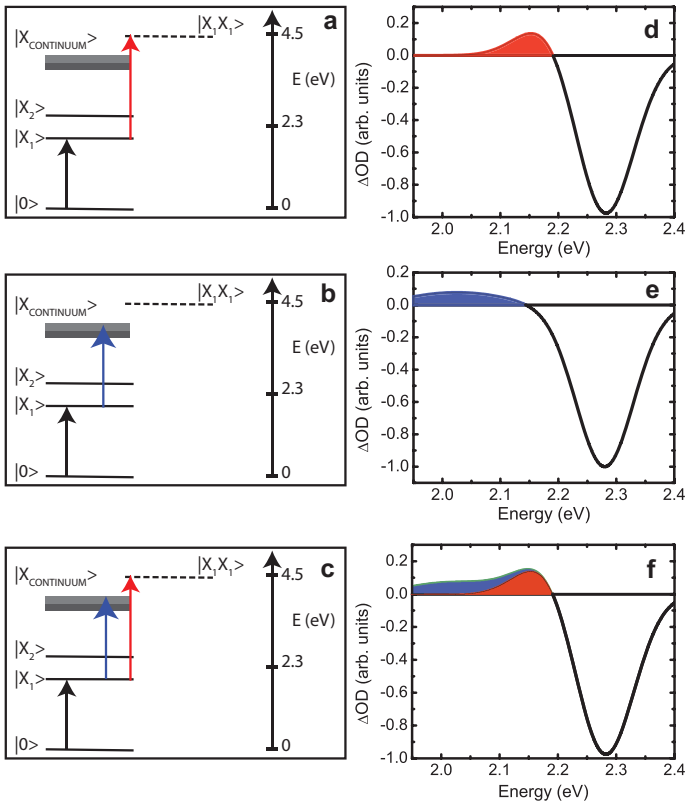

FIGURE 4–3: Transitions from (a) an excitonic state ($|X_1\rangle$) to a biexcitonic state ($|X_1X_1\rangle$), (b) $|X_1\rangle$ to a higher energy excitonic state ($|X_{CONTINUUM}\rangle$), and (c) both (a) and (b), with their corresponding simulated TA spectra (d)-(f). Absorption into the biexcitonic state (case (a)) appears as a narrow photo-induced absorption to the red of the band edge (shaded region in (d)). Absorption into higher excitonic states in the continuum (case (b)) appears as a broad photo-induced absorption (shaded region in (e)).Reprinted with permission from [Tyagi, P. and Kambhampati, P., J. Chem. Phys. 2011, 134, 094706]. Copyright 2011, American Institute of Physics.

The way in which the two sources of ESA discussed above may be spectroscopically identified can be considered as follows. The pump pulse prepares the system in a single exciton state ($|X_1\rangle$). The absorption of the probe pulse can either excite the system to a biexciton state ($|X_1X_1\rangle$) or a higher energy single exciton state ($|X_{CONTINUUM}\rangle$) (Figure 4–3(a-b)). Simulated TA spectra

for transitions from $|X_1\rangle$ to $|X_1X_1\rangle$ and to $|X_{CONTINUUM}\rangle$ are shown in Figure 4–3(d-e). Both of these processes appear as a positive PA to the red of the band edge exciton. The former appears as a narrow PA (Figure 4–3d) due to biexciton induced level-shiftings and the magnitude of this PA is proportional to the biexciton binding energy [25, 30, 87, 125]. The latter should appear as a broad spectral feature (Figure 4–3e) due to excited state absorption into the spectrally broad continuum of states [137, 138], the magnitude of which is proportional to the square of the transition dipole moment between the initial and final excitonic states. In the presence of both of these processes, a large and broad PA should be observed to the red of the band edge (Figure 4–3c and Figure 4–3f).

The early time experimental TA spectra for the capped, untreated and phototreated CdSe QDs are shown in Figure 4–4a. At $t \sim 3ps$, an intense and broad (1.95 eV to 2.2 eV) PA is observed in the TA spectrum of phototreated dots whereas no PA is observed in this region in the capped and untreated dots (shaded region in Figure 4–4a).

We rationalize these observations with the proposition that lower excitonic symmetry in the phototreated dots (due to the presence of surface states) leads to the modification of the optical selection rules in these dots. Therefore, the transitions from single excitonic states to the continuum states that were forbidden in well-passivated CdSe/ZnS dots become allowed in phototreated dots. This proposal of surface induced perturbations bears conceptual similarity to recent pseudopotential calculations which have shown that the presence of surface states in QDs does indeed lower the symmetry of the system and

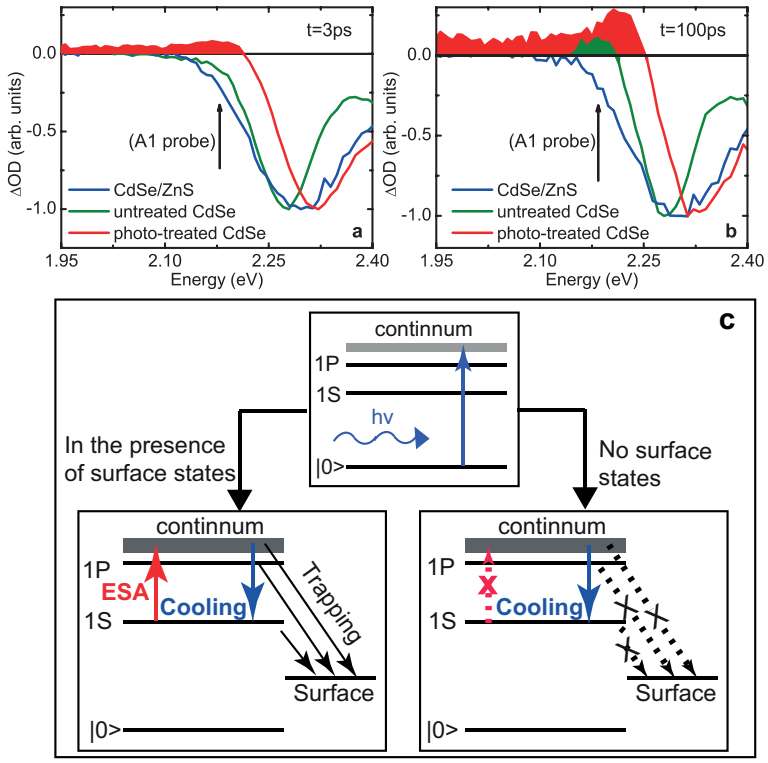

FIGURE 4–4: Transient absorption (TA) spectra at (a) $t = 3$ ps and (b) 100 ps. The $A1$ probe signal is related to the occupancy of the surface states. The phototreated dots reach the surface trapped state within 3 ps (as shown by the positive $A1$ probe signal) whereas the untreated dots take 100 ps to reach such a state. The ZnS-capped dots do not reach the surface trapped state even in 100 ps due to the large confinement potential provided by the ZnS capping layer. New transitions (shown in the red shaded region) become optically allowed in phototreated dots due to change in the optical selection rules. (c) Schematic illustrating various competing relaxation processes that contribute to the TA signal, in the presence and absence of surface states. Reprinted with permission from [Tyagi, P. and Kambhampati, P., J. Chem. Phys. 2011, 134, 094706]. Copyright 2011, American Institute of Physics.

leads to mixing of allowed and forbidden states [96]. We suggest that atomistic calculations will be able to test this proposal.

In particular, we propose that the ESA, corresponding to $|X_1\rangle \rightarrow |X_{CONTINUUM}\rangle$ transition, that is not observed in the capped and untreated dots becomes

allowed in the phototreated dots resulting in a broad PA in these dots (Figure 4–4a), that is

$$\begin{aligned} \langle X_1|\hat{V}|X_{CONTINUUM}\rangle &= 0 \quad \text{well-passivated dots} \\ \langle X_1|\hat{V}|X_{CONTINUUM}\rangle &\neq 0 \quad \text{photo-treated dots} \end{aligned} \tag{4.2}$$

where, $\hat{V}$ is the interaction Hamiltonian, and $|X_1\rangle$ and $|X_{CONTINUUM}\rangle$ are the initial and final excitonic states respectively.

Qualitatively similar PA features have been previously observed in CdSe QDs under intense 400 nm excitation (4-32mJ/cm^2) [139,140]. In both experiments, it was observed that higher pump fluences transformed the bleaching signals into absorptive signals (PA). In both cases, the spectrally broad PA was only observed under extremely intense excitation conditions, effectively photo-treating the dot, presumably during the course of the experiment. Also, the observed PA was spectrally broad rather than the usual narrow PA associated with biexciton induced level shifts. These results, in conjunction with ours, show a common result that a spectrally broad PA arises under prolonged and/or high intensity excitation conditions, in contrast to the narrow PA which accompanies biexciton induced level shifting [25, 30, 87, 125].

Another difference between the three systems is the time dependence of the PA feature due to biexciton-induced level shiftings (Figure 4–4(a-b)). It has been previously shown that this feature (labeled A1 in Figure 4–4(a-b)) can be positive or negative depending on the state of the system and changes sign with time [1,24,25,30,47,48,87,125,127]. Specifically, there is a positive PA for a hot exciton which decays to negative bleach for a relaxed exciton ($t \sim 1ps$) and eventually, reaches a positive value for a surface trapped exciton. In the case of ZnS-capped dots, the A1 feature never attains a positive value at late

times (Figure 4–4b) indicating absence of any surface trapping on a $100ps$ time scale. The A1 signal for untreated dots is negative at $t = 3ps$ (Figure 4–4a) and goes positive at $t = 100ps$ (Figure 4–4b). In phototreated dots, this signal reaches a positive value at $t = 3ps$ (Figure 4–4a). This shows that the excitons in phototreated dots reach a surface trapped state in $t = 3ps$, the untreated dots take $100ps$ to reach such a state and CdSe/ZnS dots do not reach the surface trapped state even in $100ps$. This is consistent with the expected passivating function of the ZnS shell. The ZnS shell provides a large confinement potential and reduces defect density, thereby minimizing charge trapping at the surface of the dot [1, 87, 124, 130].

The competition between the intraband relaxation and surface charge trapping controls the dynamics of the A1 signal [1,48,87]. In phototreated dots, the surface trapping process competes with the intraband relaxation whereas it is relatively slow in CdSe/ZnS dots [1]. The untreated dots represent a middle ground between the phototreated dots and CdSe/ZnS dots. Our assignment of surface charge trapping is consistent with the recent electric force microscopy studies that show development of charges in CdSe/CdS QDs under $396nm$ excitation [141].

Based on the discussion above and comparing the simulated spectra (Figure 4–3) to the experimentally observed TA spectra (Figure 4–4), we conclude that in the case of phototreated dots, the large and broad PA is due to a combination of surface charge trapping and ESA into the continuum. The overlap of this large positive PA due to surface-induced processes and the negative bleach due to state-filling gives rise to reduced bleach signal in phototreated dots. This implies that in these dots, ΔOD_{1S} is not purely due

to state-filling. Rather, it is a combination of surface-induced processes and state-filling. Therefore, the timescales extracted from ΔOD_{1S} for these dots cannot be attributed to MER. On the other hand, ZnS-capped dots do not exhibit any signatures of surface trapping in the TA spectra as discussed above and therefore, give a true measure of X and XX recombination times. The effect of these surface-induced processes on MEG signals will be discussed in Section 4.3.5.

4.3.3 Role of state-filling in the observed multiexciton recombination dynamics

In the absence of surface trapping, the relationship between the multiexciton population and MER can be established by linking the state-filling signals to the chronology of events. Figure 4–5 illustrates the key processes of relaxation and recombination by schematically depicting the chronology of events for the case of an initial (homogeneous) population of $N = 3$.

In this schematic, a femtosecond pump pulse creates an initial hot multiexciton on the timescale of the pump pulse ($\sim 50fs$). This initial multiexciton distribution will thermalize (relax) via several processes [24, 25, 30, 127]. The electrons relax on $200fs$ timescale via Auger electron relaxation thereby uppumping the holes [24, 25, 30–32, 109, 124, 127, 130], and the holes relax on $500fs$ timescale via coupling to ligand vibrations and phonons [24, 25, 30, 109, 127, 135, 142]. This thermalized distribution of multiexcitons ($N = 3$) will then undergo MER whereby $N = 3$ thermalized excitons recombine to $N = 2$ hot excitons [29, 31, 32, 45, 46, 113, 114, 124]. This process is schematically illustrated at $t = 3ps$ based on the data from Klimov which suggested a scaling law for MER rates and multiplicity [29, 46, 114, 124]. Within the next $500fs$

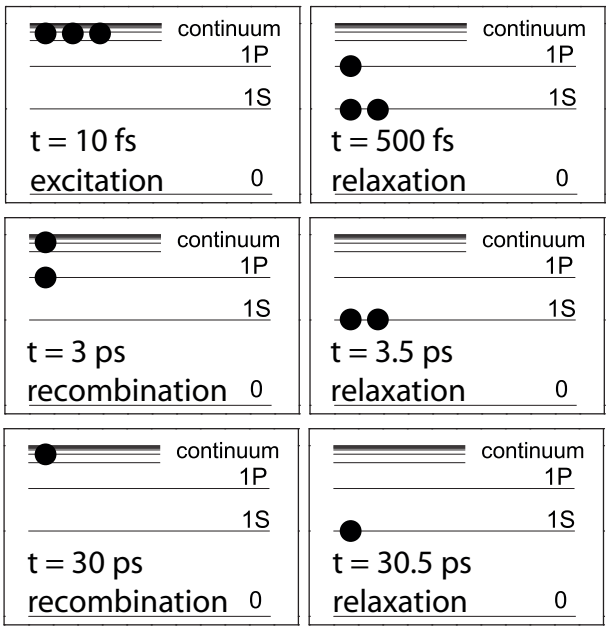

FIGURE 4–5: At t = 10 fs, an initial Poisson distribution of excitons are created by the pump pulse. This schematic illustrates the case of a homogeneous population of $N = 3$. At $t = 500fs$, the initially hot multi-exciton distribution thermalizes (relaxation). At $t = 3ps$, the thermalized distribution of triexcitons undergoes multiexciton recombination (MER) thereby generating a hot biexciton distribution. At $t = 3.5ps$ this biexciton distribution thermalizes. At $t = 30ps$ the thermalized biexcitons undergo MER thereby generating a hot single exciton. At $t = 30.5ps$ the single exciton thermalizes. Reprinted with permission from [Tyagi, P. and Kambhampati, P., J. Chem. Phys. 2011, 134, 094706]. Copyright 2011, American Institute of Physics.

($t = 3.5ps$), the $N = 2$ hot multiexcitons will thermalize, and at $t = 30ps$, this biexciton will recombine, and finally thermalize by $30.5ps$.

In this homogeneous distribution, since the band edge state is two-fold degenerate, there will be no change in the band edge bleach when comparing $N = 2$ and $N = 3$. This point was first made by Klimov [46, 102, 114, 124, 129], and subsequently confirmed by our group by pumping directly into the band edge $1S$ exciton (X_1) and also into the higher-lying $1P$ exciton (X_3) [47, 48, 126]. The results of these experiments are shown in Figure 4–6 at $t = 1ps$ following

completion of hot exciton thermalization (relaxation [24, 25, 30, 127]). These data show the non-linear absorption spectrum ($OD_{NL} = \Delta OD + OD_0$) which allows monitoring the development of state-filling by successive population of the manifold of excitonic states [43, 46–48, 126]. Pumping into the $1S$ exciton bleaches that transition resulting in the $B1$ feature probed here and all prior MER and MEG experiments. But these $1S$ excitation conditions can only prepare a maximum occupancy of $\langle N \rangle = 2$. Pumping into the 1P exciton, however, enables the possibility of creating higher occupancies due to the higher degeneracy of the 1P state. 1P excitation also creates the B1 feature in addition to bleaching signals at higher energies which arise from multiexcitons ($N > 2$) [25, 47, 48, 126]. These bleaching features at higher energies allow the monitoring of the dynamics of higher multiexcitons as opposed to the $B1$ feature which is sensitive only to 1S population ($\langle N \rangle \leq 2$).

In the absence of surface trapping, the multiexciton decay in QDs can be quantitatively described using a set of coupled rate equations for QD populations P_i, where i is the number of excitons in the QD.

$$\frac{dP_i}{dt} = \frac{P_{i+1}}{\tau_{i+1}} - \frac{P_i}{\tau_i} \tag{4.3}$$

In CdSe QDs, the fractional band edge bleaching is 0.5 for$N = 1$ and 1.0 for $N \geq 2$ [46,129], the 1S absorption change (ΔOD_{1S}) can thus be written as

$$\Delta OD_{1S}(t, N) = 0.5P_1(t) + \sum_{i=2}^{N} P_i(t), \quad \text{where} \quad \sum_i P_i = 1 \tag{4.4}$$

For a given initial N, the individual dot undergoes time dependent bleach recovery following the above coupled rate equations. Since the pump pulse creates a distribution in population, $\langle N \rangle$, the experiment measures a set of

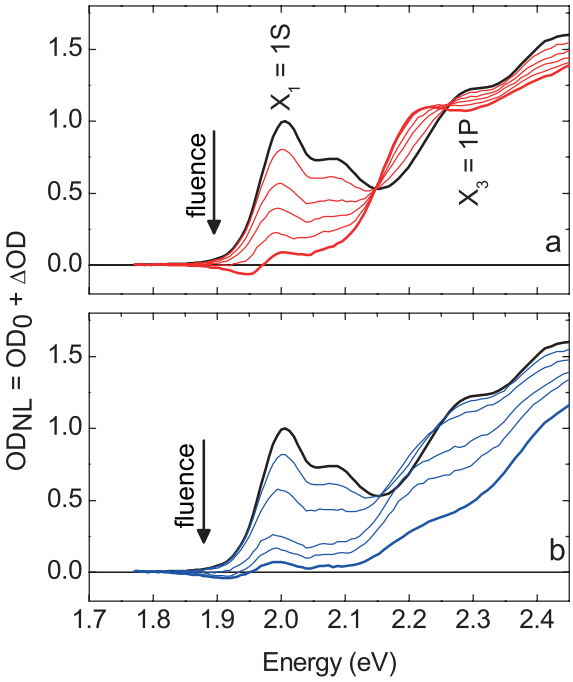

FIGURE 4–6: (a) Pumping directly into $X1$ bleaches the band edge exciton absorption. (b) Pumping into $X3$ creates additional bleaching signals through filling of higher lying states. The X1 state is nominally the $1S$ exciton which only affects the filling of the $1S$ states. The $X3$ state is nominally the 1P type exciton which is six-fold degenerate. Hence, high fluence enables bleaching of higher transitions as shown in the data. Reprinted with permission from [Sewall, S.L et. al., Appl. Phys. Lett. 94 (24), 243116 (2009)]. Copyright 2009, American Institute of Physics.

coupled rate equations averaged over the initial distribution, therefore

$$\Delta OD_{1S}(t) = \langle \Delta OD_{1S}(t, N) \rangle_N \tag{4.5}$$

Figure 4–7 shows the results of the coupled rate equations for homogeneous and Poisson distributions of QD populations. For $\langle N \rangle \leq 2$, ΔOD_{1S} exhibits a biexponential decay as expected from the two-fold degeneracy of the 1S state. For $\langle N \rangle > 2$, rather than seeing the contribution of multiexcitons ($N > 2$) in ΔOD_{1S}, one sees an induction time (delayed onset of the 1S decay)

due to rapid filling of the 1S state from higher states (inset of Figure 4–7c). The higher excitons will fill the vacated lower excitonic states on the $500fs$ timescale [24, 25, 124, 127]. The decay of the 1S state population ($N = 2$ to 1) appears as a decay in the bleach.

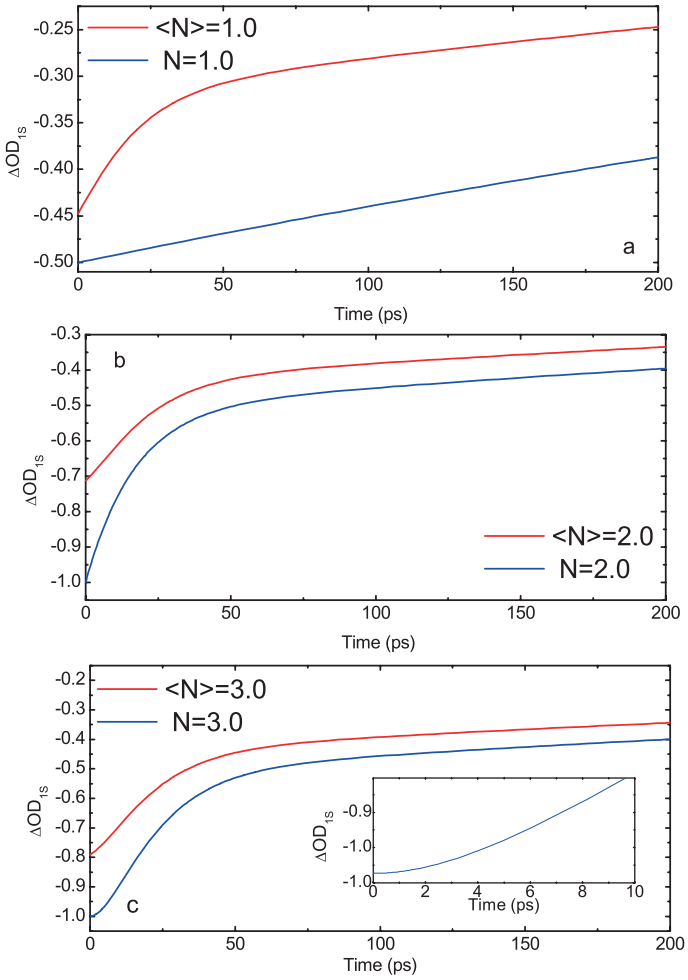

FIGURE 4–7: Ground state bleaching signal for homogeneous (blue) and Poisson (red) distribution of QD populations obtained using the kinetic rate model. An induction time of approximately 2 ps is visible in the bleach for $N = 3$ (inset of c) as expected from rapid filling of $1S$ state from the higher excitonic states. Reprinted with permission from [Tyagi, P. and Kambhampati, P., J. Chem. Phys. 2011, 134, 094706]. Copyright 2011, American Institute of Physics.

This prediction is in perfect agreement with the experimental data in Figure 4–8. The data show a clear induction time of $2ps$ for the case of CdSe/ZnS. Hence, the capped dots exactly recover the anticipated idealized response. In contrast, the untreated and phototreated CdSe dots do not show such a pronounced induction time because of the depopulation of the 1S state due to surface-induced processes. These observations are consistent with the fact that the 1S state is two-fold degenerate and therefore, has major contributions only from $N \leq 2$ (X and XX) and not from higher multiexcitons [47, 48, 126].

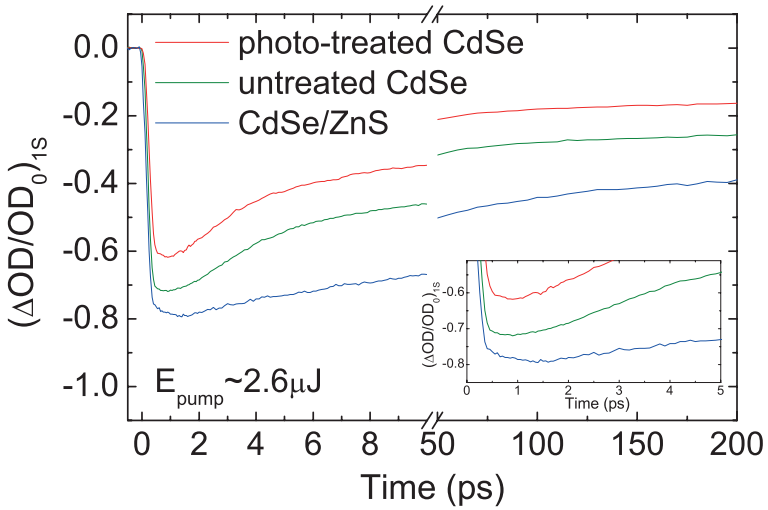

FIGURE 4–8: High fluence (corresponding to $\langle N \rangle > 3$) ground state bleaching signal for phototreated, untreated and ZnS-capped CdSe QDs. The rapid filling of the $1S$ state from higher states results in an induction time of nearly 2 ps (inset) in capped dots whereas the induction time is negligible in the phototreated dots due to the fast depopulation of the $1S$ state via other surface-induced recombination/-trapping processes. Reprinted with permission from [Tyagi, P. and Kambhampati, P., J. Chem. Phys. 2011, 134, 094706]. Copyright 2011, American Institute of Physics.

In order to obtain the decay constants for $N > 2$, one needs to measure the absorption change for 1P (ΔOD_{1P}) rather than the ΔOD_{1S}, since ΔOD_{1P} will have a major contribution from multiexciton states corresponding to $N > 2$.

Essentially, the B1 feature generally used to monitor MER it not sensitive to recombination from higher multiexcitons. We propose that the B3 feature [25, 87] (ΔOD_{1P}) allows for monitoring the recombination for $N > 2$.

4.3.4 Fluence and surface dependence reveal false multiexciton recombination signals

Figure 4–9 shows the bleaching transients for the three systems as a function of $\langle N \rangle$. The fluence dependence of CdSe/ZnS dots is idealized firstly in that it is purely biexponential at all fluences. Secondly, the time constants (τ_X and τ_{XX}) do not change with fluence. Only the amplitudes corresponding to each time constant change, exactly as expected from the Poisson distribution. And thirdly, the long time value of the bleach is precisely 50 percent of the early time value of the bleach for high fluence, as expected from simple kinetic considerations. These observations are consistent with the fact that ΔOD_{1S} has major contributions from X and XX owing to the two-fold degeneracy of the $1S$ state.

In stark contrast, the absence of the passivating shell has a profound influence on the above three metrics of idealized response. The untreated and phototreated CdSe QDs show bleach recovery transients that are not simple biexponentials. In particular, both show additional fast decay components on the 2 to 4 ps timescale, which may be incorrectly interpreted as arising from recombination of higher multiexcitons [29,46,114]. These uncapped CdSe dots (with and without photo-treatment) do not show the expected bleach recovery to 50% of their initial value.

We, therefore, conclude that in well-passivated CdSe/ZnS dots, the rapid filling of the two-fold degenerate 1S state from higher excitonic states prevents

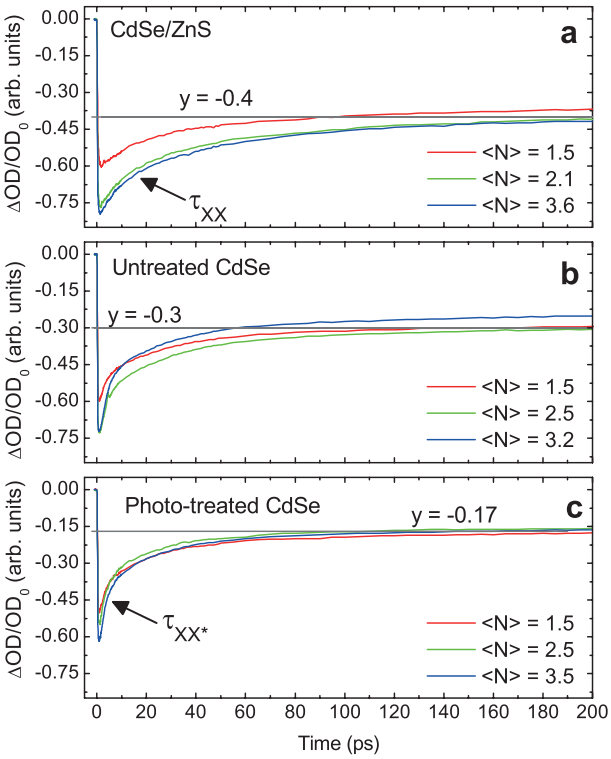

FIGURE 4–9: Ground state bleaching signals for (a) ZnS-capped, (b) untreated, and (c) phototreated CdSe QDs for different values of $\langle N \rangle$. Additional fast time scales appear in the phototreated and untreated dots leading to a faster bleach recovery in these systems as compared to the well-passivated CdSe/ZnS dots. The late time signal, which is due to a single exciton, is larger in CdSe/ZnS dots than in untreated and phototreated CdSe QDs. Reprinted with permission from [Tyagi, P. and Kambhampati, P., J. Chem. Phys. 2011, 134, 094706]. Copyright 2011, American Institute of Physics.

ΔOD_{1S} from yielding MER times for $N > 2$ [24, 25, 30, 127]. In the case of phototreated dots, however, additional time scales of significant amplitude appear in ΔOD_{1S} due to surface-induced processes as discussed below and can be misinterpreted as MER times for $N > 2$.

We note that our analysis calls into question the physical origin of the previously reported time scales for up to four excitons extracted from ΔOD_{1S} in CdSe QDs [29]. The additional time scales observed in the bleach could

have been due to poor surface passivation of the dots, thereby, yielding time constants corresponding to other surface-induced processes rather than the Auger recombination processes. Similar fast time scales have been observed in the bleaching signal for CdSe and CdTe QDs under intense excitation conditions [139, 140], and different surface passivations [29, 143]. These observations are consistent with our results and our proposed hypothesis that surface-induced processes such as charge trapping and ESA in QDs lead to additional timescales in ΔOD_{1S}.

We contrast our results to a recent report on CdSe and CdS QDs which suggested that the MER rates are insensitive to hole trapping. Since the time duration of the pulses used in those experiments was $> 5ps$, and the signature of charge trapping appears as a fast component ($\sim 2ps$) in the bleaching signal (Figure 4–9c), it is not surprising that effects of hole trapping could not be resolved in those experiments.

One might anticipate that only TA experiments are subject to these false signals and hence a time-resolved photoluminescence (t-PL) experiment is a cleaner measure of the relevant processes [57, 58, 60, 61]. This view would be mistaken. Essentially, t-PL will observe the very same generic decay time(s) as the $B1$ spectral feature in the TA spectra [25, 30, 46, 124, 127]. A t-PL measurement would have the same fast components for phototreated dots, with several added disadvantages. In the case of t-PL, the time resolution is usually low (1 to 10 ps vs. 50 to 100 fs for TA), and there is a complete absence of complementary spectroscopic signatures (e.g. the A1 region extensively analyzed in detail below and in related experiments [1]). In fact, it is the existence of the complementary spectral signatures that is utilized here to

suggest a common physical origin for spurious measures of MER, MEG and blinking.

4.3.5 Surface-induced effects on multiexciton generation signals

We next connect these surface-dependent studies to MEG analysis. Very low fluence B1 bleach transients are commonly used to extract the quantum efficiency (QE) of QDs. The QE is calculated by taking the ratio of the early time bleaching signal (A) to the late time bleaching signal (B), $QE(\%) = \frac{A}{B}$ (Figure 4–10a).

To illustrate the presence of false MEG signals we performed low fluence ($\langle N \rangle \sim 0.5$) TA measurements under conditions where MEG is forbidden by energy conservation ($E_{pump} \sim 1.35E_g$). In most experiments that aim to measure the MEG yield, $\langle N \rangle$ is held to a much lower value to avoid the creation of multiexcitons by multiple photon absorption. Here, since we use $\langle N \rangle \sim 0.5$, we correct for the multiexciton population by direct absorption of multiple photons by taking into account the Poisson distribution of QD population. In this case, the population of single excitons to total excitons is 0.77. Hence the dots will have some fraction of multiexcitons which would be expected to yield a fast component and give an apparent MEG yield of 123%. This implies that any apparent MEG signal with $QE > 123\%$ must be artifactual. We find that for the same initial fractional bleach (corresponding to $\langle N \rangle \sim 0.5$), the capped dots give a QE of 125% precisely as expected whereas the phototreated and untreated dots give a QE of 200% and 145% respectively (Figure 4–10a). This confirms the complete absence of any artifactual signals in capped dots, and the presence of large MEG-like artifactual signals in the uncapped dots.

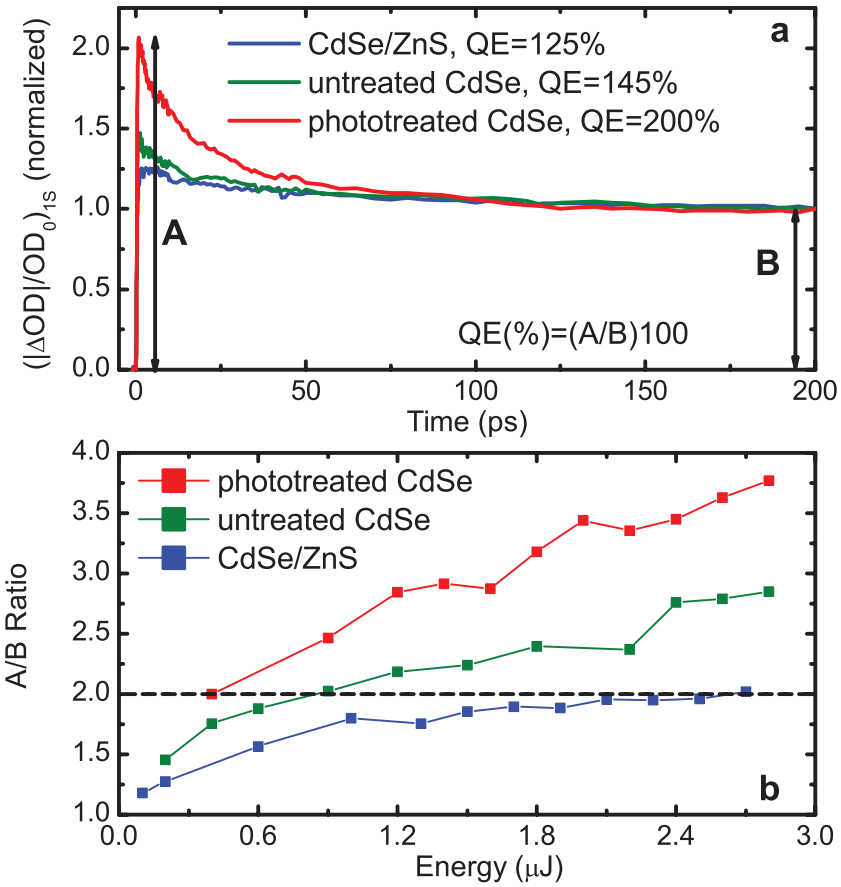

FIGURE 4–10: Illustration of false positive signals for multiple exciton generation (MEG). (a) Low fluence ground state bleaching signal for three surface conditions. For the same initial occupancy for the three systems ($\langle N \rangle = 0.5$), the phototreated dots show a false positive MEG signal. (b) For CdSe/ZnS dots, the A/B ratio saturates at 2 (as expected from state-filling of the two fold degenerate $1S$ state) whereas it exceeds this limit and goes up to 4 in the case of phototreated dots. Reprinted with permission from [Tyagi, P. and Kambhampati, P., J. Chem. Phys. 2011, 134, 094706]. Copyright 2011, American Institute of Physics.

We also find that at high fluence, the early time bleach ($t = 1ps$) saturates at 0.6/0.7/0.8 for photo-treated/untreated/capped dots respectively (Figure 4–10b), and the late time signal ($t = 200ps$), which is due to X, is larger in capped dots than in untreated and phototreated dots (Figure 4–9). In phototreated

dots, ΔOD_{1S} will have contributions from ESA into the continuum, surface charge trapping and state-filling. These data suggest that the overlap of the positive PA due to ESA and charge trapping, and the negative bleach due to state-filling gives rise to a reduced bleach signal in phototreated dots, thereby giving a false QE of 200%.

Given that the contribution of a state to the TA signal is proportional to the population of the corresponding state, the 1S bleaching signal will reach its maximum value when the 1S state is full (two excitons for CdSe QDs) and would decay to the single exciton value at late times ($t = 200ps$). Due to the linear scaling of ΔOD with $\langle N \rangle$ (Equation 4.1), one would expect the A/B ratio not to exceed 2 for the 1S state. In contrast to this expectation, recent atomic pseudopotential calculations [144] predict a nonlinear scaling of ΔOD with $\langle N \rangle$ and propose that for the 1S state the A/B ratio cannot exceed 1.5 in well-passivated CdSe dots. In disagreement with their theory, we find that in the case of well-passivated CdSe/ZnS dots the A/B ratio saturates precisely at 2 for high fluences (Figure 4–10b) as expected from Equation 4.1. In the case of phototreated dots, however, this ratio exceeds 2 and goes up to 4 at high fluence (Figure 4–10b).

Due to the controversial nature of the MEG issue, there are several timely reviews which thoroughly outline the concepts and the salient results in this field [57,59,60]. Briefly, it has now become clear that there is some photoproduct which creates artifactual signals and thereby yields false MEG yields [57, 60, 145]. This photoproduct and the false MEG yield are exacerbated by the combination of high photon energy and low sample flow rates. Hence, rapid stirring of the sample diminishes the photoproduct and the MEG yield [57–61].

The nature of the photoproduct and processes that create the false signals has remained unclear. Our results identify a spectroscopic signature of this photoproduct as well as the processes that lead to false MER and MEG signals.

The TA spectra in Figure 4–4 clearly show that the phototreated dots undergo rapid and efficient surface trapping. As the excitons undergo surface trapping [1,87] one sees the formation of mixed phase core/surface excitons [25, 87] which are strongly polar [1]. We introduce the notation of XX^* to suggest the existence of a perturbed multiexcitonic state that decays faster than XX.

While the nature of XX^* state is unclear, it is conceivable that phototreatment may simply perturb the equilibrium of weakly adsorbed ligands [137, 146] thereby increasing the rate of surface trapping [47, 48, 87]. In this case, XX^* would be a perturbed state comprised of a combination of core excitons and surface trapped excitons [25, 87]. Since there is no evidence of photoionization in the phototreated dots (based on the decay time scales observed here), it is likely that XX^* is not a "charged" state (exciton with an excess charge). Rather, it is a polarized state due to the migration of charges to the surface [1, 87] as shown by the TA spectra in Figure 4–4. At present, these experiments are not able to distinguish the pathways by which the surface charge buildup proceeds. This buildup of charges at the surface is similar to what is referred to as charging in MEG experiments, introduced by Klimov [57, 60]. Our data identify a clear spectroscopic signature of a perturbation to the electronic structure of the QD which results in large amplitude spurious MER and MEG signals. Atomistic calculations should be able to provide a realistic picture of XX^* by computing its decay rates and intraband transition strength to the continuum.

From an experimental standpoint, these experiments on CdSe QDs have two clear advantages in advancing MEG analysis: (*i*) one can easily do surface passivation studies (e.g. ZnS shells) and (*ii*) the additional spectroscopic signatures (e.g. the broadband and narrowband PA) are easy to resolve. We expect that a similar approach may be helpful in the MEG analysis of other systems.

4.3.6 Implications for blinking in quantum dots

As a final point, we note that these surface dependent studies bear relevance to the nature of the dark state in single dot blinking experiments [36, 104, 120, 147–155]. The standard picture of blinking invokes a trion as the dark state [36, 39, 120]. Yet recent experiments have convincingly shown that the trion cannot be the dark state in a QD based on their quantum yield and decay rates [38, 39]. The experiments by Guyot-Sionnest directly measure the decay time of the trion by electrochemically preparing a trion [38]. Since the dot film is electrochemically charged and then optically pumped under modest illumination, a trion is created. The experiments showed that the decay rate of the trion is found to be slower than that of the biexciton. Hence the trion cannot be the cause of the dark state. In parallel, the experiments by Bawendi reveal that the intensity of PL from the dark state is lower than that of the biexciton [39]. Simple kinetics clearly show that the decay rate of the as yet unidentified dark state must be faster than that of the biexciton. Both experiments suggest that our understanding of the origin of blinking in terms of trions and biexcitons is lacking.

We propose that the surface-induced fast decay processes (due to photo-treatment) discussed here may be the underlying cause of the dark state

which causes blinking. The dynamics of multiexcitonic states involving surface trapped charges appear as additional decay components in the bleaching signal that are faster than the biexciton (Section 4.3.1 and Section 4.3.4). In the case of phototreated dots, this fast decay component (τ_{XX^*}) is found to be $\sim 2.4ps$. Since $\tau_{XX} = 28.5ps$, $\frac{\tau_{XX}}{\tau_{XX^*}} \sim 10$. This ratio is precisely the same as suggested by Bawendi [39] based on PL intensities of the dark state relative to the biexciton. Hence we propose that the polarized multiexciton (XX^*) is the dark state which causes QD blinking.

4.4 Conclusions

In this chapter, we have shown that the standard pump/probe transient absorption methods of analysis in MER and MEG experiments are significantly contaminated by artifactual signals due to surface-induced processes. The presence of surface trap sites enhances the rate of surface trapping, and leads to the modification of optical selection rules in QDs. In particular, these surface-induced processes lead to additional time scales in the bleaching signal that can be misinterpreted as MER times from higher multiexcitons. These processes also lead to significant MEG signals, notably under conditions where MEG is forbidden by energy conservation. Finally, we show that well-passivated CdSe/ZnS dots recover all the signatures of the idealized MER and MEG experiment. We suggest that for reliable measurement of MER and MEG, it is essential to monitor the absorption change as a function of wavelength. When the TA spectra indicate the presence of surface-induced processes, the standard MER and MEG experiments yield false results. In

addition to affecting multiexciton dynamics, surface-induced processes also result in large electrostatic effects in CdSe QDs. We address this topic in the next chapter.

‘The most exciting phrase to hear in science, the one that heralds new discoveries, is not ‘Eureka!’ but ‘That’s funny...’ ’
- Isaac Asimov

Chapter 5

Piezoelectric response in semiconductor quantum dots via surface charge trapping

In this chapter, we explore the piezoelectric response of CdSe quantum dots (QDs). Owing to their wurtzite lattice structure, CdSe QDs are intrinsically piezoelectric. Therefore, the electric field created by trapped charges on the surface of the QD will result in a mechanical strain in the QD. Moreover, if the charge trapping process is impulsive with respect to the time period of the phonons, the electric field created by the trapped charges will act as a driving force to excite coherent acoustic phonons in the QD. This implies that this piezoelectric response manifests as the electron-phonon coupling strength in these systems and is proportional to the acoustic phonon amplitude. Surface and fluence dependent studies presented in this chapter reveal that one can control the piezoelectric response of CdSe QDs by modifying the surface conditions, and in turn the surface charge trapping rates of the QD.

5.1 Introduction

QDs are nanoscale semiconductor crystallites which can interpolate between the quantized limit of molecules and the continuum limit of bulk solids [46]. The lower excitonic states of the dot are quantized, as denoted by atomic-like term symbols having low degeneracy [29, 46, 156]. These lower states yield phenomena such as quantized Auger recombination [29] and Coulomb blockade [157]. In contrast, the higher states converge to a continuum, enabling creation of dozens of excitons per dot, thereby creating an excitonic plasma with $\rho_{e-h} \approx 10^{20} cm^{-3}$ [139, 158, 159].

Excited electron-hole pairs can launch acoustic vibrations of the lattice. The interaction of excited charge carriers with these vibrations, called phonons, can determine many aspects of a systems response, from the Stokes shift in quantized systems [83, 160, 161], to carrier thermalization [66, 67] and piezoelectricity [70, 71] in continuum systems. A clear understanding of these interactions in semiconductor nanocrystals is of particular importance given the increasing demand for nanoelectronic devices [162,163]. For example, the saturation velocity of charge carriers in a system is limited by phonon emission, thereby, limiting the operating speed of electronic devices. Also, the switching time of a laser and other optoelectronic devices is limited by the electron thermalization time which depends on electron-phonon (e-ph) interactions.

While the excitonic states can be described at various levels of theory [46, 156, 164, 165], colloidal quantum dots are conveniently described in terms of

an effective mass approximation model [46, 156]. Regardless of theoretical approach, the lower energy transitions yield resolvable absorption features (Figure 5–1a) which reflect quantized excitonic states of low degeneracy (Figure 5–1b). Therefore, one can describe the electron-phonon interactions in terms of a displaced harmonic oscillator picture (Figure 5–1c). In this situation, the e-ph coupling is parameterized in terms of the relative displacement of the harmonic potentials for each quantized state [83]. In these systems, one can probe e-ph couplings directly in the time domain by observing coherent phonons via femtosecond spectroscopy.

Whether in molecules [166], carbon nanotubes [160], or the excitonic states of quantum dots [81,83,167], the coherent phonon dynamics can be related to e-ph coupling via direct optical excitation of coherent phonons via a femtosecond laser pulse. Figure 5–1d shows coherent optical and acoustic phonons in CdSe colloidal quantum dots upon excitation directly into the band edge ($1S$) exciton with $40fs$ laser pulses.

Coherent phonons are also observed in continuum systems such as bulk solids, metal nanoparticles [66, 67], and semiconductor quantum wells [70, 71]. In the case of metallic systems, coherent acoustic phonons are launched indirectly via impulsive lattice heating [67] rather than directly via the femtosecond laser pulse. In this mechanism, an ultrafast pulse creates a hot electron distribution which rapidly thermalizes and impulsively heats the lattice (Figure 5–1e). The two-temperature model parameterizes this energy exchange in terms of an electron-phonon coupling constant, g_{e-ph} [67]. In the case of strain engineered piezoelectric multiple quantum wells [70, 71], the femtosecond pump pulse creates an excitonic plasma [159] which impulsively screens

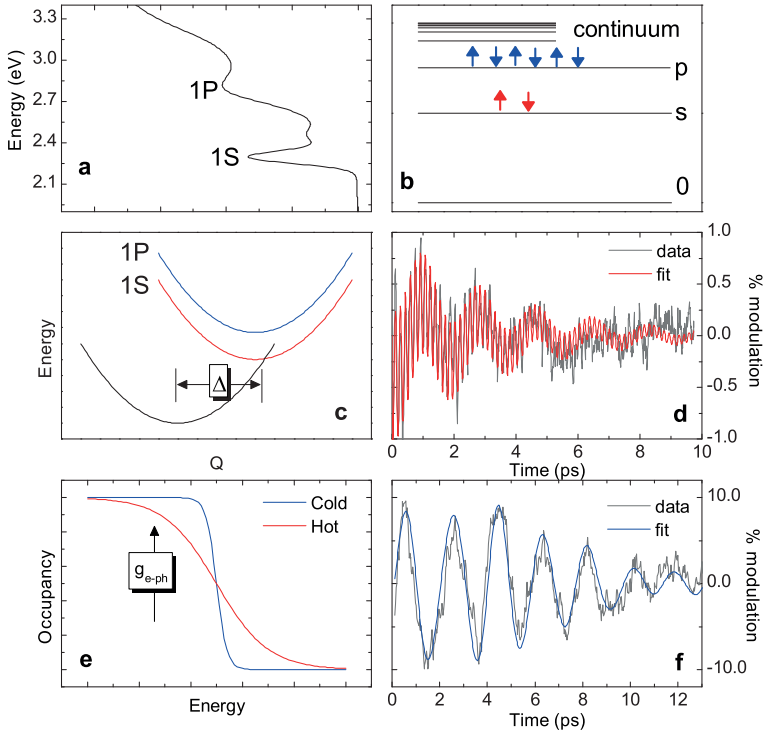

FIGURE 5–1: (a) Absorption spectrum of CdSe colloidal quantum dots. (b) Schematic level structure. (c) Direct optical excitation of coherent phonons in the displaced harmonic oscillator model for quantized states. (d) Low fluence excitation into the $1S$ quantized state yields both coherent optical and acoustic phonons. (e) Indirect generation of coherent phonons via impulsive lattice heating for continuum states. (f) High fluence excitation into the continuum yields large amplitude coherent acoustic phonons. Reprinted with permission from [Tyagi, P. et. al., Nano Lett. 10 (8), 3062 (2010)]. Copyright 2010, American Chemical Society.

the intrinsic piezoelectric field of the system thereby launching piezoelectric coupled acoustic phonons. In these situations, the electron-phonon coupling and its manifestation via coherent phonons is viewed in terms of a continuum response. Since the higher energy states of a quantum dot converge towards an excitonic continuum, one might anticipate a similar e-ph response to intense excitation into these non-quantized states [139, 140, 158].

In contrast to such expectations, we show here a completely new manifestation of e-ph interactions due to spatial migration of charges in the quantum dot: extrinsic piezoelectric coupling. Since CdSe has a wurtzite lattice and is intrinsically piezoelectric, we expect that there would be a piezoelectric response due to the screening of the intrinsic field by the excited electron-hole plasma, as in the case of quantum wells. On the contrary, we find that unlike quantum wells, the intrinsic response in quantum dots is negligible, and the majority of the piezoelectric response is extrinsic and predominantly arises due to the migration of charges to the surface of the QD.

By direct observation of e-ph coupling via coherent phonons, we show that the spatial separation of charges in a quantum dot yields large amplitude coherent acoustic phonons. Since the charge separation (due to localization of the hole at the surface) is on a sub-picosecond timescale, it is vibrationally impulsive for acoustic phonons. The extrinsic piezoelectric response is found to be at least an order of magnitude larger than the intrinsic screening response and is furthermore tunable at the single exciton level. Surface dependent studies reveal that the large amplitude piezo response can be controlled by altering the surface passivation of the QD. In addition to revealing a new mechanism of coherent acoustic phonon generation, these results offer a way of modulating the optical response of quantum dots and suggest design principles for quantum dot based optoelectronic devices.

5.2 Experimental Methods

These results were obtained using a state-resolved femtosecond spectroscopic technique which has been previously described [24, 30, 83, 87, 127]. Experiments were performed on colloidal CdSe quantum dots ($R = 1.6nm$) with

three surface classifications denoted as (*i*) photo-treated, (*ii*) untreated, and (*iii*) capped. The "photo-treated dots" were prepared by several hours of intense illumination without flowing the sample (see Section 5.A). These dots, prepared by the illumination procedure, undergo efficient surface trapping which competes with intraband relaxation (Figure 5–3b inset). The "untreated dots" are measured in a flow cell at short exposure times, and the capped dots have a passivating ZnS shell. The transient absorption measurements yield $\Delta OD = OD_{pump-on} OD_{pump-off}$, where OD is the optical density of the sample. The signal obtained (ΔOD) has both exciton (non-oscillatory) and phonon (oscillatory) contributions. To obtain the phonon contribution, the transients were fit to a multi-exponential model function and the oscillations were extracted by a standard subtraction procedure [83]. The fast Fourier transform (FFT) of the oscillations reveals a phonon mode at a frequency of $26cm^{-1}$ (Figure 5–3c) which corresponds to the well-known longitudinal acoustic (LA) phonon mode [83, 168].

5.3 Results and Discussion

In our prior work [83], the femtosecond pump pulse was resonant with the lower quantized states with fluence intentionally adjusted to maintain low mean occupancies, ($\langle N \rangle < 0.5$). Here, we excite with fluences which create exciton densities of up to $\langle N \rangle \sim 3$ and each exciton having $0.5eV$ to $1.0eV$ of excess electronic energy to dissipate. Owing to the large excess electronic energy per dot and the fast sub-ps hot exciton cooling times [24, 124, 127], one might anticipate that the dissipation of excess electronic energy impulsively heats the quantum dot lattice, thereby, launching coherent acoustic phonons. Alternatively, the excitonic plasma created by the intense pump pulse [159]

($\rho_{e-h} \approx 10^{19}10^{21} cm^{-3}$) could screen the intrinsic electric field of wurtzite CdSe quantum dots [169] and coherent phonons would be launched as in the case of piezoelectric quantum well structures.

In principle, the large amplitude coherent acoustic phonons observed under high excitation density into the continuum may arise from any of the three well established mechanisms of electron-phonon coupling: (*i*) direct optical, (*ii*) impulsive heating, and/or (*iii*) screening of intrinsic piezoelectric field. In order to identify the mechanism driving these large amplitude coherent acoustic phonons, we perform these femtosecond pump/probe experiments on dots of the same size with different surface passivation. The surface dependent studies show that none of the above mechanisms account for the observed results.

Figure 5–1f shows coherent acoustic phonons in CdSe quantum dots upon excitation with intense femtosecond pulses at 3.1 eV. Under these excitation conditions the optical phonon is no longer coupled as we have previously described [83], in contrast the coherent acoustic phonon amplitude increases with excitation intensity. Figure 5–2b shows the pump/probe transients upon excitation with $\langle N \rangle \sim 2$. Since the excitation of the acoustic phonon mode produces frequency modulation of the absorption spectrum [83], the probe is tuned to the red of the band edge (1S) exciton to maximize the oscillation amplitude. The pump is tuned to 3.1 eV to access the continuum states. Adopting the notation of Klimov and co-workers, we have labeled the transient spectral feature in the probed region (Figure 5–2c) as A1 [30,46,124]. We have shown that this feature can have a positive or negative sign based upon the excitonic state which is probed [30, 87, 125]. Indeed, the A1 transients in

Figure 5–2b are positive or negative based upon surface passivation, and in some cases can change sign with time. This sign change will be important in subsequent analysis.

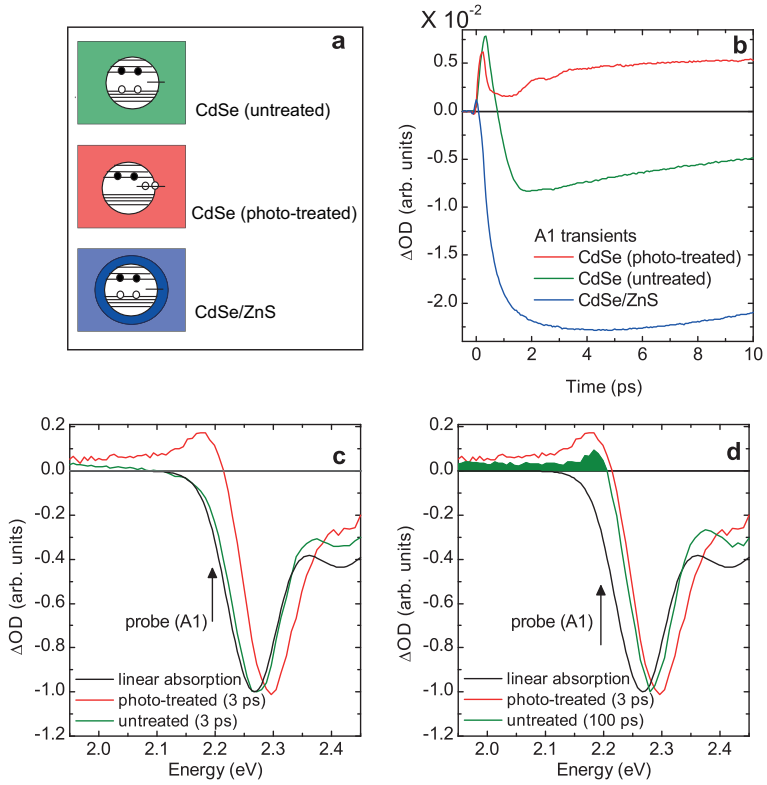

FIGURE 5–2: (a) Schematic illustration of photo-treated, untreated and ZnS-capped dots at $t \sim 1$ to 3 ps. (b) Femtosecond transients of CdSe dots under high excitation density, for 3.1 eV pump to access the continuum states. Coherent acoustic phonons are readily visible in the A1 transients for photo-treated dots. (c) and (d) Femtosecond transient absorption spectra of untreated and photo-treated dots. The untreated dots reach a surface trapped state in $t = 100$ ps (as shown by the positive A1 signal in the probed region), whereas the photo-treated dots reach such a state in $t < 3ps$. Reprinted with permission from [Tyagi, P. et. al., Nano Lett. 10 (8), 3062 (2010)]. Copyright 2010, American Chemical Society.

The transients for the three surface conditions are shown in Figure 5–2b. It is clear that the oscillations are much more pronounced in the photo-treated

dots, being visible without requiring extracting residual oscillations. In contrast, the oscillations are much weaker for the untreated and ZnS-capped dots. We note that the sensitivity to observing the oscillations is nearly identical ($\pm 10\%$) in all cases, as the probe is tuned to the peak in the derivative of the absorption spectrum [83]. Attenuated oscillations in ZnS-capped CdSe nanorods were similarly observed by Lanzani and co-workers [85].

The assignment of surface characterization is based upon the transient absorption (TA) data in Figure 5–2c-d. Our prior work has shown that the sign and amplitude of the pump/probe signal in the probed spectral region (A1) reflects the excitonic state of the system via biexciton induced level shiftings [30, 87, 125]. The pump pulse produces an exciton which undergoes intraband relaxation [24, 127] and ultimately undergoes surface trapping [87]. Our earlier results showed that it is specifically the hole that gets trapped at the surface in CdSe quantum dots [87]. When the exciton is near the band edge ($t = 0.1ps$ to $5ps$), the A1 signal is negative and a surface trapped exciton (t = 50 - $500ps$) yields a positive A1 signal for this size of dot. We refer the reader to our prior works for further details of the pump/probe signals [24, 30, 87, 125, 127].

In the case of untreated CdSe dots, the A1 signal is negative at $t = 0.1, 1, 3ps$. At long time ($t > 100ps$) the A1 signal goes positive due to a surface trapped hole [87]. In contrast, the photo-treated dots have a positive A1 signal at all times. This implies that the photo-treated dots reach the surface trapped state within 1 ps, whereas the untreated dots take much longer ($t > 100ps$) to reach this state. Therefore, in the case of photo-treated dots,

the surface trapping process is impulsive with respect to the acoustic phonon period.

Due to the efficiency of this competing trapping process [87], some fraction of the hot excitons (specifically holes) move to the surface without cooling to the 1S band edge exciton as can be understood from simple competition kinetics (Figure 5–3b). We expect that the illumination procedure adjusts the equilibrium of the weakly bound ligand which passivate the surface of the dot [137]. In order to confirm this assignment, we performed transient absorption experiments on ZnS-capped CdSe quantum dots. In these well-passivated ZnS-capped dots, we were never able to observe positive A1 signals even under prolonged intense illumination. This indicates that these dots do not reach the surface trapped state, a result completely consistent with the expected passivating function of the capping layers [170].

The surface dependent studies are essential towards determining the mechanism of coherent acoustic phonon generation. In all three cases, the size of the dot and the excitation and observation conditions are identical. Yet, only the photo-treated dot couples to the acoustic phonons with sufficient efficiency to be observed directly in the A1 pump/probe transients. In contrast, no coherent phonons are observed in the ZnS-capped dots even at high excitation densities with subtraction of the fits.

Since all three systems under investigation have band edge (1S) at $2.29eV$, they will have equal excess energy to dissipate to the lattice under identical pumping conditions ($E_{excess} = E_{pump} - E_{1S}$). This implies that if lattice heating is the driving force for the longitudinal acoustic (LA) phonons, all three systems should have the same phonon amplitude, which is inconsistent with

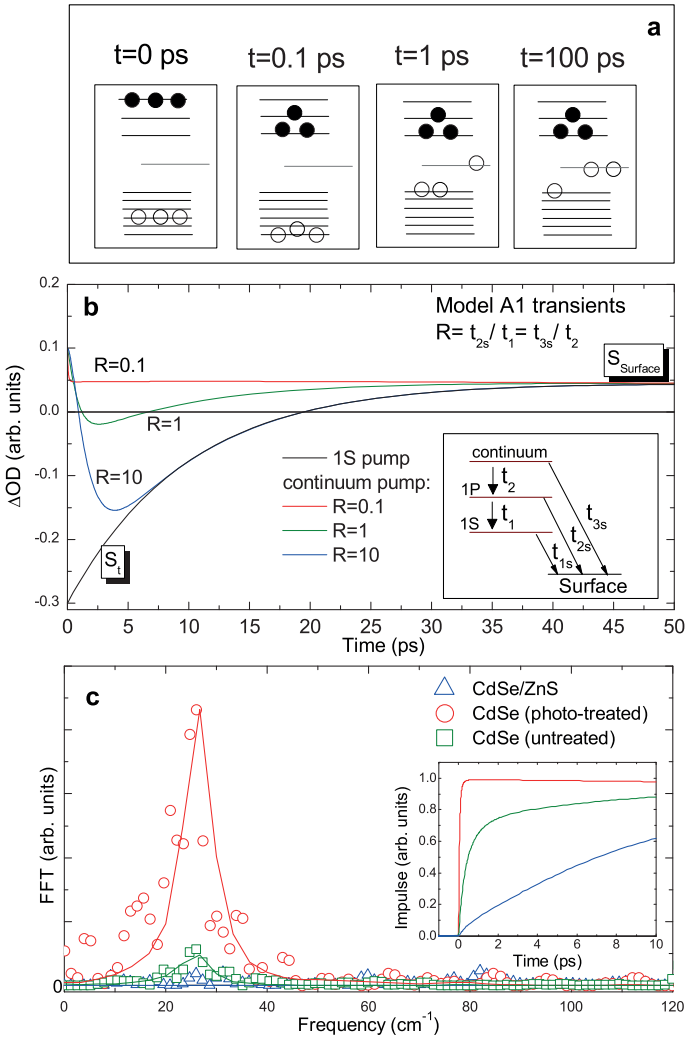

FIGURE 5–3: (a) Timeline of exciton relaxation and the competing process of hole trapping. (b) Representative pump/probe signals in the probed spectral region for band edge (1S) and 3.10 eV pumps. The signal monitors the development of surface charges. S_t becomes more positive with increase in the rate of surface trapping. The inset shows a schematic of the intraband relaxation and the competing surface trapping process. (c) FFT spectra of the data (symbols) and the results of the model (lines) for the three surface passivations revealing the acoustic phonon amplitude at an incident fluence of $2.2\mu J$. The inset shows the driving impulse due to charge trapping in capped (blue), untreated (green) and photo-treated (red) dots. Reprinted with permission from [Tyagi, P. et. al., Nano Lett. 10 (8), 3062 (2010)]. Copyright 2010, American Chemical Society.

our observations. Under different pumping conditions, there would be more lattice heating for high frequency pumps than the band edge pump. This predicts an increase in the phonon amplitude with increasing pump frequency. In contrast, our previous state-dependent studies show a decrease in the amplitude of LA phonons with increasing pump frequency [83]. Hence, we can rule out lattice heating as being the dominant mechanism for generation of coherent acoustic phonons in CdSe QDs.

CdSe lattice has a non-zero intrinsic dipole moment. Photoexcitation of charge carriers will screen the intrinsic piezo field, thereby, launching coherent acoustic phonons. The contribution of the field screening to the generation of coherent phonons would be the same in capped, untreated and photo-treated dots since they have the same lattice structure. In contrast, we find that the response of the quantum dots due to the screening of the intrinsic electric field is an order of magnitude smaller than that due to coupling to the extrinsic electric field. This is revealed by comparing the FFT phonon amplitude for untreated and ZnS-capped dots, which have no surface trapping and therefore no external electric field, to photo-treated dots (Figure 5–4a).

In particular, perfectly passivated ZnS-capped dots must have contribution from lattice heating and intrinsic piezo field screening. In our experiments, we observe negligible electron-phonon coupling in capped dots and a large coupling in photo-treated dots. This implies that the amplitude of the driving force for coherent acoustic phonons is large in photo-treated dots, small in untreated dots and nearly zero in capped dots. Based on these observations, we must necessarily rule out the previously described mechanisms and invoke a new mechanism that is intimately related to surface properties of the QD.

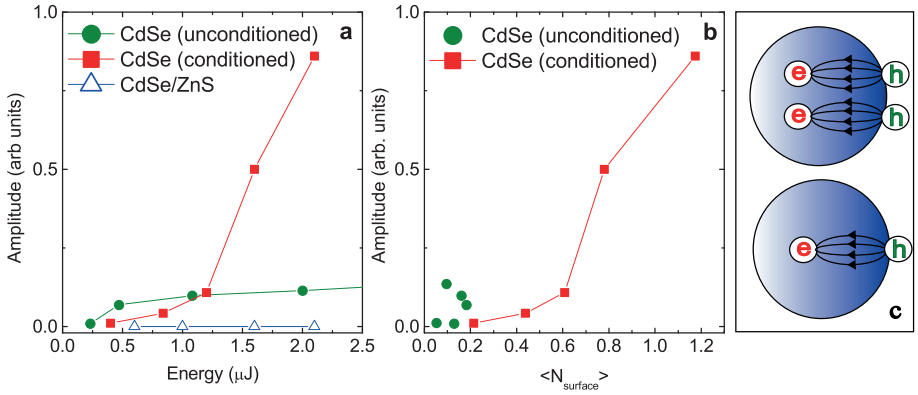

FIGURE 5–4: Fluence dependence of acoustic phonon FFT amplitude for the three surface passivations (a). Relating the phonon FFT amplitude to the mean occupancy of surface trapped charges. No correlation is observed in the case of untreated dots whereas there is a positive correlation in photo-treated dots (b). Schematic illustrating the generation of coherent acoustic phonons via surface charge trapping (c). Reprinted with permission from [Tyagi, P. et. al., Nano Lett. 10 (8), 3062 (2010)]. Copyright 2010, American Chemical Society.

The data suggest that the process of surface trapping creates the impulse which launches coherent acoustic phonons. When the exciton gets trapped at the surface, it creates an electric field which turns on at the timescale of the trapping process. The electric field arises from the migration of charges to the exterior of the quantum dot. Due to the piezoelectric nature of the wurtzite CdSe quantum dots [169], this impulsive electric field launches coherent acoustic vibrations of the lattice. A necessary feature of this process is that it proceeds at the single charge level owing to the excitation and trapping of discrete charges.

The lower limit of the surface piezo response is from the ZnS-capped dots. In the limit of perfect passivation, the impulse would purely arise from impulsive lattice heating and from screening of the intrinsic piezo response of wurtzite CdSe [169]. In these capped dots we see no observable coupling to

acoustic phonons suggesting that the contribution of the above listed mechanisms is at least an order of magnitude smaller than the extrinsic piezo response observed here (Figure 5–4a).

This assignment of extrinsic piezoelectric coupling via surface charge trapping is consistent with the standard damped driven oscillator model commonly used to model coherent phonons in nanoparticles (Figure 5–3c) [66, 67]. We model the system as a damped driven harmonic oscillator, the damping time and frequency of which are determined from the experimentally observed oscillations. The main issue is to derive the driving impulse due to surface charge trapping. This is accomplished by solving the kinetic rate equations for the system shown in the inset of Figure 5–3b. We fix t_1 and t_2 and change the ratio R to control the competition kinetics in order to study the role of surface passivation. We define $R = \frac{t_{2S}}{t_1} = \frac{t_{3S}}{t_2}$, so that $R = 0.1$ ($R = 10$) corresponds to the case where trapping is ten times faster (slower) than the intraband relaxation. Solving the rate equations, we obtain the population of the surface state as a function of time for $R = 0.1/1/10$. Since the impulse, $I(t)$, due to the charge build-up is proportional to the number of charges on the surface $\langle N_{surface}(t)\rangle$, we can write

$$I(t) = C\langle N_{surface}(t)\rangle, \tag{5.1}$$

where C is a constant. The inset of Figure 5–3c shows the impulse obtained for different rates of surface trapping ($R = 0.1/1/10$). Using $I(t)$ as the driving impulse, we solve the damped driven harmonic oscillator for the three cases. The oscillations thus obtained are Fourier transformed and the results are plotted in Figure 5–3c for comparison with the data. The symbols are the

FFT of the experimentally observed oscillations and the lines are the model results. The results for $R = 0.1$ (red), $R = 1$ (green) and $R = 10$ (blue) fit well to the photo-treated, untreated and capped dots data respectively and are consistent with the proposed mechanism.

The inset in Figure 5–3b shows a schematic of the competition kinetics between intraband relaxation and excited state surface trapping. The main panel of Figure 5–3b shows how the A1 pump/probe signals are related to the excited state surface trapping process. In simple terms, the A1 signal will be positive for a hot exciton, will relax towards the negative for a cold (relaxed) exciton, and ultimately converge upon a positive sign for a surface trapped exciton [87].

We simulate the A1 transients from the solution of the kinetic rate equations using

$$\Delta OD(t) = \sum_i A_i n_i(t) \tag{5.2}$$

where $n_i(t)$ is the population of state i and A_i is the amplitude for ΔOD associated with state i. These calculations illustrate the dependence of A1 transients on the surface trapping rate and initial pumping conditions (Figure 5–3b). The results of this calculation are in good agreement with our previous experimental work [24, 30, 87, 127]. Regardless of the value of R and the initial pumping conditions, all A1 signals meet at late times, implying that in all cases, the system eventually ends up in the same surface trapped state. However, the early time A1 signal depends on the rate of surface trapping. As trapping becomes more efficient than the intraband relaxation, some population directly goes to the surface and the A1 signal becomes more positive at early times. It is this population which forms the vibrational impulse.

The number of surface trapped holes can be extracted from the A1 signal. A hole that relaxes to the band edge has a specific value of the early time A1 signal (S_t) and any deviation from S_t (δS_t) is due to surface trapping. Noting that the surface trapped hole ($t = 50 - 100ps$) has a specific value of the signal ($S_{surface}$) (Figure 5–3b), one can calculate the fraction (F) of the excitons which have a surface trapped hole by taking the ratio $\frac{\delta S_t}{S_{surface}}$ (see Section 5.A).

We estimate that the fraction $F \approx 0.0/0.02/0.6$ for capped/untreated/photo-treated dots respectively. Essentially, altering the surface passivation provides a control of the competition kinetics which determines the dominant coupling mechanism. Since exciton relaxation completes in $\sim 1ps$ [24, 127], we estimate that the polarizing process via excited state surface trapping [87] proceeds on a distribution of timescales from 0.1-1ps, precisely as needed to be in the impulsive regime.

The surface treatments show that the impulse which launches the coherent acoustic phonons does not arise from intrinsic mechanisms of direct optical coupling, impulsive heating, or impulsive screening of the intrinsic piezoelectric field of wurtzite CdSe QDs. Instead, the coupling to acoustic phonons is primarily dominated by this new mechanism of extrinsic piezoelectric field due to surface trapped holes, within the detection limits.

Figure 5–4a shows the fluence dependence of the intensity of the FFT of the acoustic phonon. A similar fluence dependence was obtained by Alivisatos and co-workers [140]. In reality, the untreated dots most likely have some polarization accumulated during the course of the experiment. We related the peak FFT intensity to the number of surface trapped holes, Figure 5–4b.

In the case of untreated dots, no correlation is found between the phonon amplitude and the number of surface trapped charges ($\langle N_{surface}(t)\rangle$) whereas in photo-treated dots, the amplitude increases with increasing $\langle N_{surface}(t)\rangle$ (Figure 5–4b).

5.4 Conclusions

In CdSe QDs, excitation into the continuum creates creates new coupling mechanism which reflects a large amplitude, extrinsic piezoelectric response. In addition to identifying the mechanism of phonon generation in QDs, this method also reveals a way of modulating the piezoelectric response of these systems. The piezo response can be enhanced or suppressed by an order of magnitude based upon surface treatment. The tunability and large amplitude of this extrinsic response suggests its importance for QD based optoelectronic devices. We note that these results hold for only piezoelectric QDs. It would be interesting to study surface-dependence of phonons in "non-piezoelectric" QDs, which may reveal new e-ph coupling mechanisms.

5.A Appendix

5.A.1 Characterization of photo-treated dots

The photo-treatment involves exposing the sample to high energy light ($3.1eV$) for a prolonged period of time (1 to 3 hours) depending on the size of the dot. To maximize the effect of pre-conditioning the dots via illumination, a non-flow cell was used for the sample. In contrast, the exposure of untreated dots to light was kept to a minimum by flowing the sample.

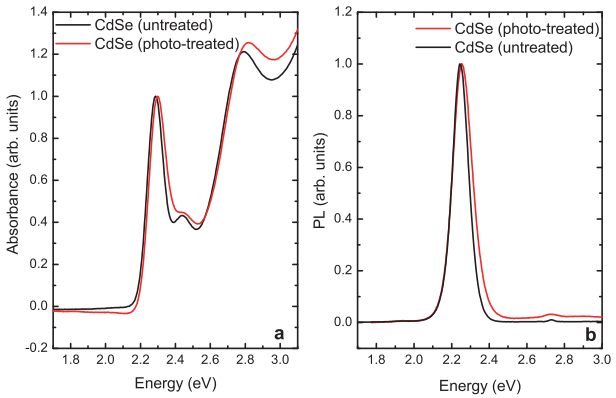

FIGURE 5–5: Comparison of photo-treated and untreated CdSe quantum dots (R=1.6nm). a) Absorbance normalized to the band edge. b) Normalized photoluminescence excited at 3.10eV. Reprinted with permission from [Tyagi, P. et. al., Nano Lett. 10 (8), 3062 (2010)]. Copyright 2010, American Chemical Society.

The pre-conditioning process (photo-treatment) used here maximizes the buildup of surface trapped charges which polarizes the dot. The development of surface trapped charges (specifically holes) was first reported by Klimov [171] and subsequently confirmed by us [87].

The absorption and PL spectra for untreated and photo-treated CdSe QDs ($R = 1.6nm$) are shown in Figure 5–5. The spectra for photo-treated dots were recorded after exposure to $2.4\mu J/pulse$ of $3.10eV$ radiation at $500Hz$ for 90 minutes. Figure 5–5 shows that preconditioning the dots does not physically

alter the dots in an irreversible manner. The absorption and PL spectra (taken a few hours after pre-conditioning) are essentially fully recovered following the pre-conditioning process. Hence this pre-conditioning process produces a reversible effect upon the dots.

The TA spectra provide more information about the effect of illumination on CdSe QDs (Figure 5–6). The TA spectra shown in Figure 5–6 were taken at a time delay of $3ps$. Since both the electron and the hole relax to the band edge in $\sim 1ps$ [24,30,127], any dynamics after $1ps$ are related to surface charge trapping [87].

We use the PA observed to the red of the band edge as a fingerprint of surface trapped charges and the timescale at which charges build up. This PA feature has been extensively discussed in previous work by our group [30, 47, 48, 87, 125]. In the most common situation discussed in those works, the PA is due to biexciton based level shiftings, a point first discussed by Klimov [46]. However, at long time ($\sim 100ps$), the PA is due to surface trapped charges (holes) [87].

The PA observed to the red of the band edge at $t = 3ps$ is also due to charges trapped at the surface. In untreated dots, there is a bleach at 3 ps which turns into an induced absorption (2.15 eV - 2.20 eV) at 100 ps. In photo-treated dots, a large amplitude, spectrally broad (1.77 eV - 2.20 eV) PA is observed at 0.5- 3 ps indicating an increase in the rate of surface charge trapping in these dots. In the absence of polarization via pre-conditioning, this broad PA is only observed at $\sim 100 - 200ps$.

The TA spectrum for CdSe/ZnS dots was unaffected by the preconditioning process and a large PA was never observed in these dots. This is because

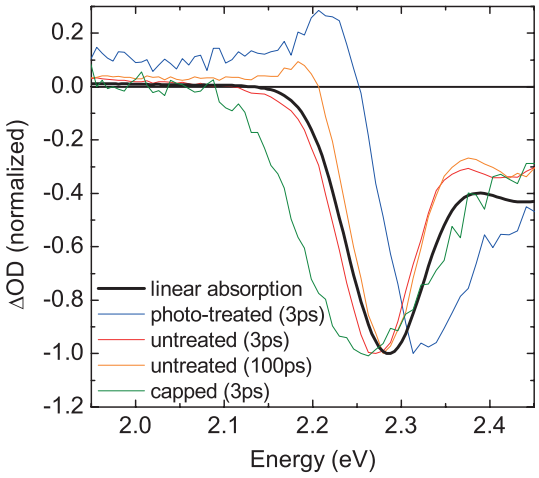

FIGURE 5–6: Transient absorption spectra for photo-treated, untreated and ZnS-capped CdSe QDs ($R = 1.6nm$) at $E = 2.2\mu J$. The black curve is the linear absorption spectrum for untreated dots. Reprinted with permission from [Tyagi, P. et. al., Nano Lett. 10 (8), 3062 (2010)]. Copyright 2010, American Chemical Society.

of the strong confinement potential created by the ZnS capping layer which provides a greater degree of surface passivation and prevents the migration of charges to the surface [170].

From the data shown in Figure 5–6 and Figure 5–7, we conclude that pre-illumination does not physically alter the dot or change the energy spectrum of dot. Instead, the preconditioning process increases the rate at which charges get trapped at the surface. This effect is presumably due to the dynamic equilibrium of weakly adsorbed ligands on the surface [91,137] which is affected by the photo-treatment.

5.A.2 Calculation of the number of surface trapped charges

Previous work from our group has shown that the charges get trapped on the surface over a range of time scales [87]. The rate of trapping is a function of the state that the charges are excited into, the trapping being faster from the

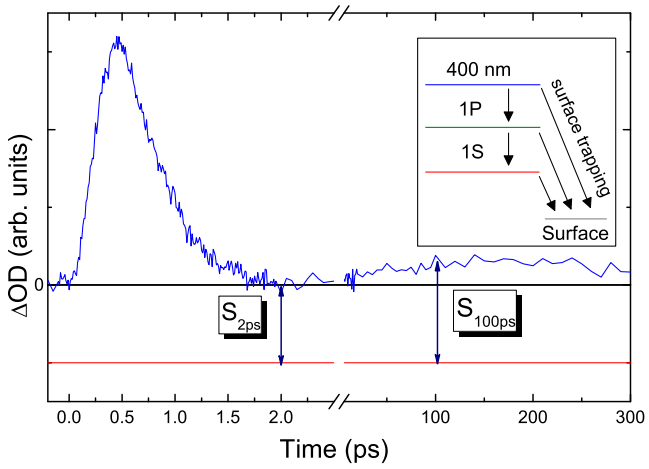

FIGURE 5–7: Calculation of the number of charges trapped at the surface. The blue line is the observed A1 signal. The red line corresponds to the signal expected in the absence of biexcitonic interactions and surface trapping. Reprinted with permission from [Tyagi, P. et. al., Nano Lett. 10 (8), 3062 (2010)]. Copyright 2010, American Chemical Society.

higher lying states. In this experiment, the sample is excited at $3.10eV$. By $t \sim 1.5ps$, both the electron and the hole relax to the band edge [24, 30, 127]. However, for $t < 1.5ps$ there are surface trapping processes that can compete with intraband relaxation [87].

Our aim is to calculate the number of charges that get trapped at the surface on a time scale impulsive with respect to the acoustic phonon period ($T_p = 1.3ps$). Following complete intraband relaxation, the charges build up on the surface over $100ps$ timescale due to slow trapping from the band edge [87], however, this trapping is not vibrationally impulsive. Therefore, we calculate the number of charges on the surface at $t = 2ps$ ($\langle N_{surface}(E) \rangle$). i.e. $\sim 1ps$

after the band edge relaxation.

$$\langle N_{surface}(E)\rangle = \langle N_{total}(E)\rangle F(E) \tag{5.3}$$

where, $N_{total}(E)$ total number of excited electron-hole pairs , E is the incident energy and $F(E)$ is the fraction of charges on the surface at $2ps$. $<>$ denotes the ensemble average. We note that the estimation of the surface trapped charges is ideally done at $t = 0.5ps$ to be well within the impulsive limit. We chose to do the analysis at $2ps$ since the signals yield a cleaner analysis there. The difference between the two times yields no major difference in the numbers or the analysis.

Calculation of $\langle N_{total}(E)\rangle$

At low excitation levels, the change in the band edge absorption is due to the occupancy of the 1S electron state. Assuming a Poisson distribution of quantum dot population, we can write [46–48],

$$\left(\frac{\Delta OD}{OD}\right)_{1S} = 1 - e^{\langle N_{total}\rangle}\left(1 + \frac{\langle N_{total}\rangle}{2}\right) \tag{5.4}$$

where, $\langle N_{total}\rangle$ is the total number of excited e-h pairs and $\left(\frac{\Delta OD}{OD}\right)_{1S}$ is the fractional band edge bleaching. Using the value of $\left(\frac{\Delta OD}{OD}\right)_{1S}$ from the experiment, $\langle N_{total}\rangle$ can be calculated at $E = 0.2\mu J$. For $E > 0.2\mu J$, we further use $\langle N_{total}\rangle = \sigma E$, where σ is the absorption cross section. This gives,

$$\frac{\langle N_{total}(E_1)\rangle}{\langle N_{total}(E_2)\rangle} = \frac{E_1}{E_2} \tag{5.5}$$

Now, knowing $\langle N_{total}(0.2\mu J)\rangle$, $\langle N_{total}(E)\rangle$ can be calculated for higher values of E. We use Equation 5.5 in conjunction with Equation 5.4 since at high

fluences photoinduced absorptions can partially cancel the bleaching signals thereby creating deviations from Equation 5.4 [46, 172].

Calculation of $F(E)$

The photoinduced absorption (A1) in the TA spectrum arises from surface trapping and level shifting due to biexcitonic interactions [30, 46, 87, 125]. A fully relaxed exciton yields a small level shift (negative A1 signal) which can be cleanly observed by direct excitation into the band edge exciton [30, 46].

In the absence of surface trapping, the A1 signal at $3.1eV$ pump will be identical to the A1 signal at band edge pump upon completion of hot exciton relaxation, $t > 1ps$. The difference between the expected and observed value of the A1 signal is reflects the number of charges trapped at the surface.

Based upon a 5% quantum yield, we assume that 95% of the excited charges go to the surface at $100ps$, we can write,

$$F(E) \approx \frac{S_{2ps}}{S_{200ps}} \tag{5.6}$$

where, S_i is the difference between the observed A1 signal and the expected A1 signal in the absence of surface trapping at time t_i. The assumption is valid since we work in the low $\langle N_{total} \rangle$ regime $(0.3 - 2.6)$ and $S_{100ps} \sim S_{300ps}$.

Now, the number of surface trapped charges can be calculated using Equation 5.3. The results of the calculation for photo-treated and untreated CdSe dots are tabulated in Table 5–1 and Table 5–2 respectively. From the results of the above calculation, it can be seen that for untreated dots $\langle N_{surface} \rangle$ is not correlated with the incident pulse energy whereas for photo-treated dots, there is a positive correlation.

At $100ps$, nearly the same number of charges gets trapped at the surface for both photo-treated and untreated dots. However, at $2ps$, $\langle N_{surface} \rangle$ increases with increasing E for photo-treated dots but is not correlated with E for untreated dots.

For capped dots, $S_{2ps} \sim 0$ for all E, therefore, from Equation 5.4, $F(E) \approx 0.0$ for all E. Hence, at $2\mu J$, $F \approx 0.56/0.02/0.0$ for photo-treated/untreated/capped dots respectively.

TABLE 5–1: Calculation of $N_{surface}$ for photo-treated CdSe ($R = 1.6nm$) QDs.

$E(\mu J)$	N_{total}	$F(E)$	$N_{surface}$
0.40	0.39	0.55	0.21
0.84	0.83	0.53	0.44
1.20	1.19	0.51	0.61
1.60	1.50	0.52	0.78
2.10	2.08	0.56	1.17

TABLE 5–2: Calculation of $N_{surface}$ for untreated CdSe ($R = 1.6nm$) QDs.

$E(\mu J)$	N_{total}	$F(E)$	$N_{surface}$
0.23	0.30	0.43	0.13
0.47	0.60	0.30	0.18
1.08	1.40	0.11	0.16
2.00	2.60	0.02	0.05
3.00	3.90	0.02	0.09

Evidence of hole trapping

It has been previously shown that it is mainly the holes that get trapped at the surface [87, 173]. The band edge signal ($B1$) monitors the $1S_e - 1S_{3/2}$ exciton, where $1S_e$ and $1S_{3/2}$ correspond to the ground state of the electron

and hole respectively. Due to the two-fold degeneracy of the $1S_e$ electron state, the $B1$ signal will depend on the occupancy of the $1S_e$ state [30, 46, 124]. Altering the surface passivation of the QD drastically changes the $A1$ dynamics, however, it has little effect on the $B1$ signal [87]. This implies that the electron dynamics are relatively unaffected by surface passivation. Hence it is the hole trapping that can be controlled by the changing the surface passivation of the QD.

5.A.3 Mechanisms for generation of coherent acoustic phonons

Impulsive heating

In continuum systems, the distribution of hot charge carriers after the laser excitation can be characterized by an electronic temperature. The heating of the lattice due to the heat flow from electrons to the lattice is commonly described by the two temperature model [66, 67]. In this model, the coupling between the electrons and phonons (lattice) is given by the following coupled differential equations

$$\frac{dT_e}{dt} = -g\frac{T_e - T_l}{C_e(T_e)} \tag{5.7}$$

$$\frac{dT_l}{dt} = -g\frac{T_l - T_e}{C_l} - \frac{T_l - T_0}{t_s} \tag{5.8}$$

where, g is the electron-phonon coupling constant, T_e is the electronic temperature, T_l is the lattice temperature, $C_l(C_e)$ is the lattice (electronic) specific heat and $\frac{1}{t_s}$ is the rate at which heat is transferred to the surroundings at temperature T_0.

In quantized systems, the energy released during the relaxation of charge carriers to the band edge would be responsible for lattice heating. In CdSe QDs with band edge at $2.29eV$, pumping at $3.1eV$ provides an excess energy of $0.8eV$ per exciton per QD. The increase in the lattice temperature due to this excess energy can be calculated as follows

$$Q = mC_l\Delta T_l \tag{5.9}$$

$$m = V\rho \tag{5.10}$$

where Q is the heat energy transferred to the lattice, m is the mass of the QD, C_l is the lattice specific heat, ΔT_l is the change in the lattice temperature, V is the volume and is the density of the QD. Using $\rho = 5.81gcm^{-3}$, $C_l = 490Jkg^{-1}K^{-1}$ in Equation 5.6, we get $\Delta T_l = 3.27K$.

For N excitons per QD the temperature rise would be equal to $3.27N\ K$. In our experiments, $\langle N\rangle \sim 2$, implying that the increase in the lattice temperature would be less than $7K$.

The excitation of the acoustic phonon mode in the quantum dot produces the frequency modulation of the absorption spectrum. Using $\frac{dE_g}{dT} = 0.26meV/K$ [167] (shift in the band edge absorption peak with temperature), we obtain a $1meV$ shift in the absorption spectrum due to a temperature rise of $4K$. The amplitude of the oscillations is related to the shift in the absorption spectrum by [83, 84],

$$A_{osc} = \left(\frac{dOD}{dE}\right)\Delta E \tag{5.11}$$

where, ΔE is the energy shift, $\frac{dOD}{dE}$ is the slope of the absorption spectrum at the sample position and A_{osc} is the amplitude of the oscillations (phonons). This gives an amplitude $\sim 0.5\%$. This is smaller than the observed amplitude

by nearly 10 times, showing that the majority effect is due to the piezoelectric response.

Furthermore, all three samples (capped, untreated and photo-treated) are pumped at $3.1eV$ and have their band edge at $2.29eV$, therefore they will have the same excess energy to dissipate to the lattice. The lattices of the three systems CdSe will also have the same specific heat. Therefore, the temperature rise is the same for capped, untreated and photo-treated dots. This implies that if lattice heating is the driving force of the LA phonons, charging the dots should have no effect on the amplitude of the phonons.

Based on the above two arguments, we can rule out lattice heating as being the dominant mechanism for generation of coherent acoustic phonons in CdSe QDs. This assignment is also supported by our previous state-dependent studies of electron-phonon coupling [83]. Since band edge pump has less excess energy to dissipate than the $3.10eV$ and 1P pumps, there would be more lattice heating for higher frequency pumps. This predicts an increase in the phonon amplitude with increasing pump frequency. However, in our previous experiments [83, 84], the acoustic phonon amplitude was found decrease with increasing the pump photon energy.

Intrinsic piezoelectric screening

Another well known mechanism for the generation of coherent acoustic phonons is screening of the intrinsic piezoelectric field [70, 71]. In quantum wells (QWs), due to the lattice mismatch of different materials there is an in-built electric field. The laser pulse excites an electron-hole plasma [159] which impulsively screens this electric field and launches phonons in QWs.

Since CdSe has a wurtzite lattice, it is intrinsically piezoelectric [169]. Photoexcitation of charge carriers will screen the intrinsic piezo field. However, the contribution of the field screening to the generation of coherent phonons would be the same in capped, untreated and photo-treated dots.

In particular, perfectly passivated CdSe/ZnS capped dots should have contribution from lattice heating and intrinsic piezo field screening. In our experiments, we observe negligible electron-phonon coupling in capped dots and a large coupling in photo-treated dots. This observation suggests that there is another driving force responsible for the observed large amplitude coherent acoustic phonons in QDs, that can be controlled by modulating the surface passivation of QDs. The amplitude of this driving force is large in photo-treated dots, small in untreated dots and nearly zero in capped dots. Hence the "untreated" dot represents a middle ground between the limits of the capped and photo-treated dots.

The data suggest that it is the piezoelectric field created by the charge carriers trapped on the surface which acts as a driving force for coherent acoustic phonons. For the driving force to be impulsive, the trapping has to be on a time scale shorter than the time period of the LA phonon. Since the electron and the hole are at the band edge by $1.5ps$ [24, 30, 127], the evolution of A1 signal after $1ps$ is related to the trapping of charges on the surface. In the case of photo-treated dots, the surface trapping takes place on a shorter time scale (τ_1) than the LA phonon time period ($T_p = 1.3ps$). In untreated dots, the time scale of charge trapping (τ_2) is of the order of T_p. For capped dots, the time scale of surface charge trapping (τ_3) is larger than T_p and is therefore not

impulsive with respect to T_p. This is supported by modeling in the following section.

5.A.4 Modeling

We model the system as a damped driven harmonic oscillator that is described by the following equation,

$$\frac{d^2x}{dt^2} + \gamma\frac{dx}{dt} + \omega^2 x = F \tag{5.12}$$

where γ is the damping constant, ω is the angular frequency of the oscillator and F is the driving force. The frequency of the oscillator was determined experimentally and was found to be $26cm^{-1}$. The damping constant $\gamma \sim \frac{1}{T_d}$, where T_d is the damping time of the observed oscillations, and was found to be $1.6ps$.

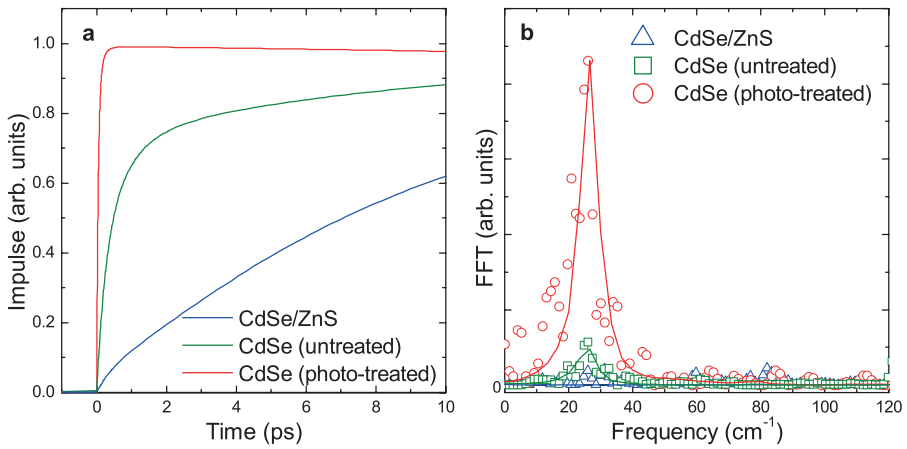

FIGURE 5–8: a) The form of the driving impulse for capped, untreated and photo-treated dots. b) FFT of the observed oscillations. The lines are the results of the model, the circles are the experimental data. Reprinted with permission from [Tyagi, P. et. al., Nano Lett. 10 (8), 3062 (2010)]. Copyright 2010, American Chemical Society.

In the proposed mechanism, the driving force for the oscillator is the piezoelectric field created by the trapping of the charges on a time scale smaller than

the period of LA phonon mode ($T_p = 1.3ps$). The driving impulse is, therefore, proportional to the population of the surface state ($P_{surface}(t)$) (Figure 5–8a). We solve the kinetic rate equations for the system shown in the inset of Figure 5–3b for $R = 0.1/1/10$. We use

$$F = C\langle N_{surface}\rangle(t) \tag{5.13}$$

in Equation 5.12, where C is a constant. The results obtained after performing FFT of the observed oscillations are plotted in Figure 5–8b. The circles are the FFT of the experimentally observed oscillations at $E = 2\mu J$ and the lines are from the model. Figure 5–8 shows that the fast surface charge build-up in photo-treated dots gives rise to large amplitude of phonons whereas the slower trapping rates in untreated and capped dots result in small amplitude phonons. The results of the model are in good agreement with the experimental data and consistent with the proposed mechanism.

'Everything must be made as simple as possible. But not simpler.'

- Albert Einstein

Chapter 6

Wave function enginering in core/barrier/shell nanostructures

In this chapter, we use a two-band effective mass model and first-order perturbation theory to study many-body interactions in core/barrier/shell nanostructures. Our investigations reveal the capacity for complete spatial control over excitonic wave functions in these systems. By exploring parameter space with core size and barrier width as variables, we show that each exciton can be in a core-localized or shell-localized state (Type-I localization) and as well in a charge-separated state (Type-II localization). Furthermore, the width of each localization region in parameter space can be tuned by controlling material properties, providing design principles for nanostructures with desirable features for key applications. Depending on the localization regime of excitons, both radiative and nonradiative decay rates can be significantly enhanced or suppressed in these nanostructures, making them suitable for dual-color emission and for producing low threshold and broad bandwidth of optical gain.

6.1 Introduction

Semiconductor nanostructures are promising materials for a wide range of applications including cell labeling, medical imaging, light-emitting diodes (LEDs), solar cells and other photovoltaic devices [15, 17–21]. Each of these applications exploits a specific property of the nanostructure. For instance, in order to have an efficient radiative recombination for cell labeling and LEDs, a large overlap of electron (e^-) and hole (h^+) wave functions is desirable. For photovoltaic devices, on the other hand, it is essential to use the charge carriers before they recombine, which makes slow recombination preferable. In the case of multicolor emission, spatial separation of different excitons is required, whereas the threshold and spectral profile of optical gain are governed by biexciton interactions [12, 25, 47–49, 102, 172]. This vast range of potential applications, each utilizing a specific property of these materials, has boosted the field of nanostructure design and wave function engineering.

Layered nanostructures have shown considerable promise in manipulating carrier wave functions and controlling carrier dynamics. In particular, by layering nanostructures in a core/shell configuration, it has been possible to produce both Type-I behavior, where the e^- and h^+ wave functions are confined in the same spatial region, and Type-II behavior, where the carriers are spatially separated [5, 6]. Adding a barrier between the core and the shell can further increase the functionality of these systems. The CdSe/ZnS/CdSe (core/barrier/shell) nanostructures have been shown to emit at two wavelengths, and their emission color and intensity can be controlled by changing the size of

the core and the shell [7, 9]. Also, the quantum yield of the core is significantly larger in CdSe/ZnS/CdSe nanostructures as compared to their core-only (CdSe) and core/shell (CdSe/ZnS) counterparts of the same core size [10]. Recently, CdSe/ZnS/CdSe nanostructures integrated on a InGaN/GaN substrate were used to build bright white-LEDs with tunable shades of white light [11]. Another advantage of core/barrier/shell nanostructures is their ability to reduce the *off* periods in fluorescence blinking. While the well-passivated CdSe/ZnS core/shell nanostructures show blinking, the dual-wavelength emission of CdSe/ZnS/CdSe nanostructures allows them to have periods where the core is *off* but the shell is still *on* [40,104]. This shortens the overall *off* period of the nanostructure making them useful in fluorescent labeling and imaging applications.

Despite the potential core/barrier/shell nanostructures have demonstrated in light emitting applications, the control they offer over excitonic wave functions still remains unexplored. Here we investigate the low energy excitonic states (1S, 2S and 1P) in these nanostructures using a two-band effective mass model and first-order perturbation theory that takes into account the dielectric discontinuities across the material boundaries. This model has been successful in describing $e^- - h^+$ interactions and the size-dependence of radiative and non-radiative decays in core/shell nanostructures [6, 12, 103, 174–179]. Although this model excludes band-mixing effects, it serves as an excellent choice in cases where the details of the electronic structure are not essential [180]. This model allows us to qualitatively understand carrier-carrier interactions and multiexciton dynamics in core/barrier/shell nanostructures. In fact, the results presented here show that the typical intuitive picture used to describe

experimental data for these systems may not always hold. For example, it is commonly assumed that the high-energy emission peak in these nanostructures arises from an excitonic state in the shell [7, 9, 10, 104]; however, our results show that depending on the size of the nanostructure, it is possible for the high-energy peak to arise from a core state and the low-energy peak from a shell state.

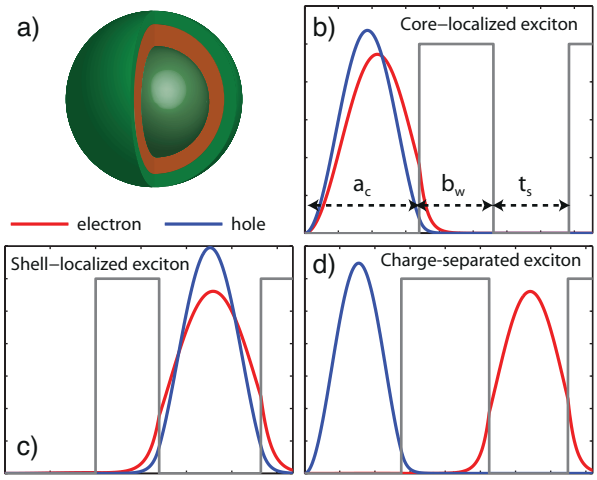

FIGURE 6–1: Localization regimes of an exciton in a core/barrier/shell nanostructure. (a) Schematic of a core/barrier/shell nanostructure. (b)-(d) Probability of finding an electron (hole) as a function of the distance from the center of the core ($f(r) = r^2|R_e(r)|^2$). Black lines depict the confinement potential profile in the nanostructure. Reprinted with permission from [Tyagi, P. and Kambhampati, P., J. Phys. Chem. C 2012, 116, 8154 8160]. Copyright 2012, American Chemical Society.

To the best of our knowledge, two theoretical studies exist on these core/barrier/shell nanostructures to date. These calculations study the S-type excitonic states for specific sizes of dots and have contributed to a better understanding of the dual-color emission property of these systems [103, 178]. Here we present the first calculation of carrier-carrier interactions for both S and P-type states in layered nanostructures. Our theoretical investigations demonstrate complete spatial control over single particle wave functions in

each state and suggest new avenues for achieving this control in semiconductor nanostructures.

Specifically, we show that by varying the core size, each exciton (1S, 2S and 1P) can either be localized in the core or localized in the shell or prepared in a charge-separated state. By exploring different regions in parameter space (with core size and barrier width as variables), we find that the 1S radiative recombination rate can be varied up to five orders of magnitude in these nanostructures. When the e^- and h^+ are spatially separated, these systems exhibit large ($> 90meV$) repulsive exciton-exciton interaction making them suitable for lowering gain thresholds. In addition to the separation of e^- and h^+ of the same exciton (e.g. $1S_e$ in core and $1S_h$ in shell), these nanostructures allow different excitons to be spatially separated (e.g. $1S_e - 1S_h$ in core and $2S_e - 2S_h$ in shell), which would significantly suppress the non-radiative relaxation between different excitonic states; a property which can be exploited to produce spectrally broad optical gain as well as dual color emission. We also find that the $e^- - h^+$ interaction is stronger in core-localized excitons than the shell-localized excitons, as expected from the 3D confinement provided by the core and 1D confinement by the shell. Finally, we study the dependence of carrier localization on effective mass and the strength of the confinement potential, which can help select and design appropriate materials for desired applications.

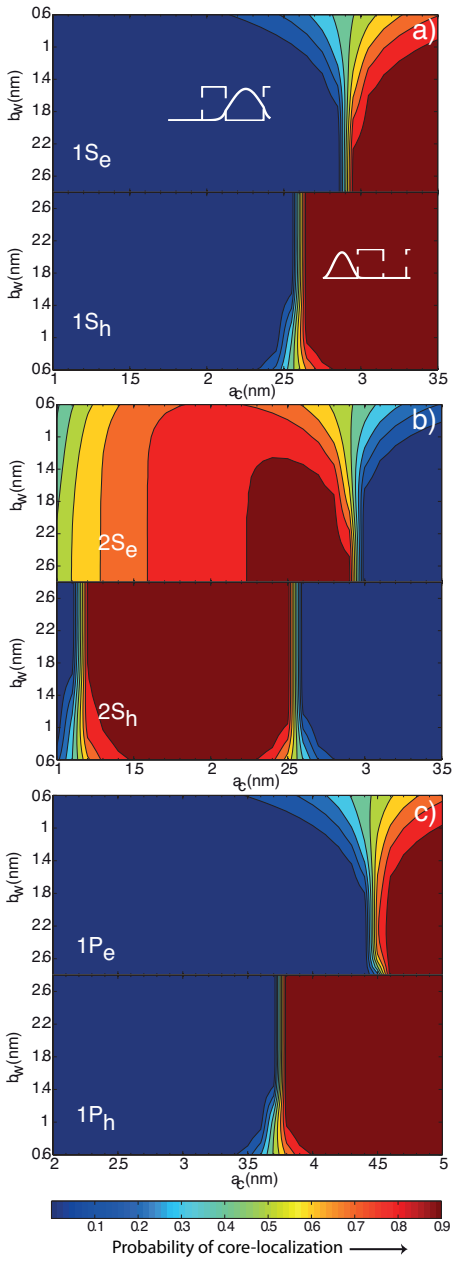

FIGURE 6–2: Probability of finding (a) 1S, (b) 2S and (c) 1P electron (top) and hole (bottom) in the core as a function of core radius (a_c) and barrier width (b_w) for a CdSe/ZnS/CdSe nanostructure of fixed shell thickness of 4ML. All three states show regions where the exciton is core-localized (both carriers in a blue region), shell-localized (both carriers in a red region) and charge-separated (charge carriers in regions of opposite color). Reprinted with permission from [Tyagi, P. and Kambhampati, P., J. Phys. Chem. C 2012, 116, 8154 8160]. Copyright 2012, American Chemical Society.

6.2 Methods

We describe carrier-carrier interactions in core/barrier/shell nanostructures (Figure 6–1) using a two-band effective mass model. Although this model excludes the band-mixing effects [110, 137, 181], it allows us to qualitatively understand the $e^- - h^+$ interactions and multiexcitonic decays in these nanostructures. In this approximation, the e^- and h^+ envelope functions (Ψ_e and Ψ_h) and confinement (kinetic) energies are calculated by analytically solving the Schrodinger equation in the conduction and valence bands respectively. Due to the spherical symmetry of the nanostructure, the confinement potential (V_b) depends only on the radial coordinate and is given by: $V_b(r) = 0$ for $r < a_c$ and $(a_c + b_w) < r < a_t$, and $V_b(r) = V_{b-off}$ for $a_c < r < (a_c + b_w)$, where, a_c and a_t are the core and the shell radii respectively, b_w is the barrier width, V_{b-off} is the conduction (valence) band offset. In this model, we set the potential at the shell boundary to be equal to V_{b-off}, which is equivalent to passivating the system with the barrier material [9]. For a spherically symmetric potential, the separation of variables yields

$$\Psi_{nlm}(r, \theta, \phi) = R_{nl}(r) Y_{lm}(\theta, \phi) \tag{6.1}$$

where, n is the principal quantum number, l and m are the angular quantum numbers, $Y_{lm}(\theta, \phi)$ are the spherical harmonics, and $R_{nl}(r)$ is the radial part of the wave function, which in this case, is a linear combination of spherical Bessel functions. To calculate the radial part for 1S, 2S and 1P states, we apply the following continuity conditions for wave functions and probability

currents each material boundary [182]:

$$R_\alpha(r_\alpha) = R_{\alpha+1}(r_\alpha) \tag{6.2}$$

$$\frac{1}{m_\alpha}\frac{dR_\alpha(r)}{dr}\bigg|_{r=r_\alpha} = \frac{1}{m_{\alpha+1}}\frac{dR_{\alpha+1}(r)}{dr}\bigg|_{r=r_\alpha}, \tag{6.3}$$

where the subscript α indexes the region in the core/barrier/shell nanostructure, r_α is the radius at the outer boundary of the region α, and R_α and m_α are the radial wave function and effective mass of the particle in region α. Additionally, the solutions must be finite at the center of the core ($r = 0$) and vanish at infinity.

Once the wave functions and energies have been calculated, we calculate the $e^- - h^+$ interaction energy (E_{eh}). E_{eh} has contributions from both the Coulomb interaction and the interface polarization energy due to dielectric discontinuity at the boundaries [174]. When the kinetic energies of the carriers are much larger than E_{eh}, we can calculate E_{eh} using first-order perturbation theory [137, 183, 184]. By analytically solving the Poisson equation for a point charge in a core/barrier/shell nanostructure with dielectric boundary conditions, we obtain the interaction Hamiltonian (H) which includes both polarization and Coulomb contributions [185]. For fixed dielectric constants, since H is a function of the location of the point and the test charges and the azimuthal quantum number l, we can calculate the carrier-carrier interaction energy for both S ($l = 0$) and P ($l = 1$) excitons using [174]

$$E_{ab} = \int d^3r_a \int d^3r_b |\Psi_a|^2 \hat{H} |\Psi_b|^2 \ , \tag{6.4}$$

where the subscripts a and b refer to the two charge carriers and $\Psi_i's$ are the envelope wave functions defined in Equation 6.1. For $a = e^-$ and $b = h^+$, this

gives us the $e^- - h^+$ interaction energy, E_{eh}. Subsequently, we calculate the biexciton binding energy (Δ_{XX}) in the charge-separated (Type-II) region as

$$\begin{aligned}\Delta_{XX} &= E_{XX} - 2E_X \\ &= 2E_{eh} + E_{ee} + E_{hh}\end{aligned} \tag{6.5}$$

where E_{XX} and E_X are the biexciton and single exciton energies respectively. This perturbative approach to calculate Δ_{XX} is not applicable in the regions of high $e^- - h^+$ overlap where the exciton is almost neutral. Due to the neutrality of the exciton, the first-order term in exciton-exciton interaction energy is nearly zero, therefore an accurate estimation of Δ_{XX} in such regions requires taking the higher order terms into account [174].

6.3 Results and Discussion

To begin with, we consider CdSe/ZnS/CdSe nanostructures. For these systems, we set $V_{b-off} = 0.9eV$ and $m_{e(h)} = 0.13m_0(0.45m_0)$ in CdSe and $0.28m_0(0.49m_0)$ in ZnS, where m_0 is the rest mass of the electron [186, 187]. The normalized probability of the e^- and h^+ of an exciton being localized in the core can be calculated as,

$$P_p = \frac{\int_0^{a_c} \left|R_p\right|^2 \, dr}{\int_0^{\infty} \left|R_p\right|^2 \, dr}\,, \tag{6.6}$$

where $p = e^-, h^+$. Figure 6–2 shows $P_{e(h)}$ as a function of barrier width b_w and core radius a_c for 1S, 2S and 1P excitons, for a fixed CdSe shell thickness (t_s) of $2.24nm$ ($\sim$ 4 monolayers (ML) [103]). For each exciton, both the e^- and h^+ show a transition from the shell to the core as a function of a_c. Since they have different effective masses, the two carriers transition from shell to core at

different points in parameter space. This separation of transition points gives rise to a region in the $[a_c, b_w]$-parameter space where one carrier is localized in the shell and the other is in the core, i.e. the material exhibits Type-II behavior. This implies that there is a transition from a core-localized to a shell-localized excitonic state via a charge-separated state.

This transition becomes apparent in the overlap integral θ_{eh} given by

$$\theta_{eh} = \left| \int_V \Psi_e \Psi_h \, d^3r \right|^2 \tag{6.7}$$

Figure 6–3 shows θ_{eh} as a function of b_w and a_c for each state for $t_s = 4$ML. As the states go from being localized in the core to the shell, θ_{eh} shows a square wave type behavior. The rate of change of θ_{eh} $\left(\dfrac{d\theta_{eh}}{da_c}\right)$ depends on b_w as it controls the sharpness of the transition from one region to another (Figure 6–2 and Figure 6–3). Since θ_{eh} is directly proportional to the radiative decay rate of the exciton, we can calculate the ratio of decay rates in the Type-I and Type-II regions [96, 188]. For 1S exciton, this ratio $= \dfrac{\theta_{eh}(Type-I)}{\theta_{eh}(Type-II)} \sim 10^5$, implying that the 1S radiative lifetime can be suppressed by up to five orders of magnitude by tuning the core radius. This suppression of the radiative decay of 1S exciton broadens the time window available to separate e^- and h^+ before they recombine, making this region useful in photovoltaic applications and other devices that require efficient charge separation.

Multiexcitons, on the other hand, decay predominantly due to non-radiative Auger recombination, where an e^- and a h^+ recombine transferring energy to a third charge carrier [2, 25, 25, 29, 31, 32, 96, 124]. This implies that in addition to suppressing the 1S radiative decay, the spatial separation of $1S_e$ and $1S_h$ will also suppress the Auger decay of 1S biexciton, thereby increasing the

biexciton emission efficiency [12,189,190]. This, in turn, will not only increase the lifetime of optical gain but also increase gain bandwidth due to emission from both the exciton and the biexciton [12,189]. Additionally, in this charge-

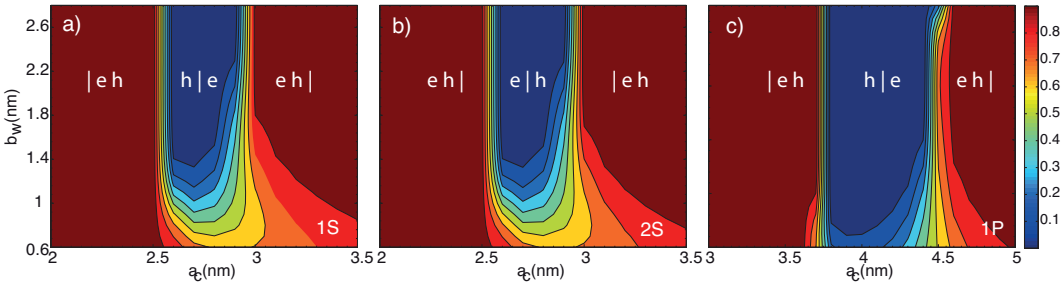

FIGURE 6–3: Overlap of (a) 1S, (b) 2S and (c) 1P electron and hole wave functions in CdSe/ZnS/CdSe as a function of core radius and barrier width. For each state there is a transition from core-localized state to charge-separated state to shell-localized state. The notation used to denote localization regimes is: (carrier in core)|(carrier in shell), e.g. "$e|h$" implies that electron is in the core and hole is in the shell. Reprinted with permission from [Tyagi, P. and Kambhampati, P., J. Phys. Chem. C 2012, 116, 8154 8160]. Copyright 2012, American Chemical Society.

separated region, the calculated binding energy for 1S biexciton is found to be positive (repulsive exciton-exciton interaction) with a magnitude greater than $90meV$; therefore, these materials are expected to exhibit lower gain thresholds in this region [102,191]. This expectation is in good agreement with recent experiments by our group where an optical gain bandwidth of $> 370meV$ is observed in CdSe/ZnS/CdSe nanostructures due to spatial separation of low energy excitons [50].

The spatial separation of excitons in this nanostructure results in suppressed relaxation processes (e.g.. exciton cooling and multiexciton recombination), which give rise to their property of dual color emission. Essentially, there is a competition between radiative recombination from the higher lying

exciton and non-radiative cooling to the lowest excitonic state. If these rates are in approximate competition, spontaneous emission will be observed from both excitons. As discussed above, the non-radiative 1S biexcitonic recombination rate can be suppressed by spatially separating $1S_e$ and $1S_h$, which increases the emission efficiency of the biexciton. In addition to the separation of e^- and h^+ of the same exciton (e.g. $1S_e$ in core and $1S_h$ in shell), these nanostructures also allow two different excitons to be spatially separated, e.g. for $1.25nm < a_c < 2.5nm$, the $1S_e - 1S_h$ exciton is in the core and $2S_e - 2S_h$ is in the shell (Figure 6–2a-b, Figure 6–3). This spatial separation of excitons will decrease the rate of cooling of the higher energy exciton, thereby enhancing its emission efficiency. If the two spatially separated excitons are separated in energy as well, their emission will be at two different wavelengths and the nanostructure will exhibit dual color emission [7, 9, 10, 104] as well as broad multiexcitonic gain. The separation in real space ensures that the overlap between the states is sufficiently small to significantly suppress relaxation processes that couple the two states. The separation in energy is necessary in order to resolve the dual color emission. If the two states are spatially separated but are too close in energy to be experimentally resolvable, one would observe only one broad emission peak rather than observing two distinct peaks separated in energy. The results of this model are in good quantitative agreement with the experimental studies on these nanostructures, that show dual color emission for only a particular set of core and shell sizes where different excitonic states are separated in both space and energy [5–7, 9, 10, 103].

We illustrate this dual color emission property using an example from the CdSe/ZnS/CdSe nanostructure studied here. From Figure 6–3, we can

identify the regions in parameter space where different excitons are spatially separated. Figure 6–4 shows the total energy of each state with and without including $e^- - h^+$ interaction energy for $b_w = 2.5nm$ and 4ML of CdSe shell, which gives an estimate of the energy separation between different states. At $a_c = 1.75$ nm, 1S and 1P are localized in the shell and 2S is localized in the core. Due to this spatial separation, the relaxation from 2S to 1P and 2S to 1S would be suppressed, whereas 1P would relax to 1S. Finally, the system will relax to a state where 1S and 2S excitons are separated in space, with each exciton having a large $e^- - h^+$ overlap (Figure 6–3). Therefore, each of these states will radiatively recombine emitting at $E_{1S} = 2.01eV$ and $E_{2S} = 2.19eV$, making this set of parameters a good choice for dual color emission.

The low energy emission peak in CdSe/ZnS/CdSe is commonly assumed to arise from the core and the higher energy peak from the shell [7, 9, 10, 104]. This assumption is based on the fact that upon the addition of CdSe shell to CdSe/ZnS there is an increase in the absorption cross-section at high energies. Our calculations show that this assumption is not always valid. For example, for $1.25nm < a_c < 2.5nm$ and $0.6nm < b_w < 2.8nm$, the 1S exciton is shell-localized, whereas 2S is core-localized (Figure 6–2). In this configuration, the low energy emission peak would arise from the shell (1S) whereas the high-energy peak would arise from the core (2S).

The spatial localization of charge carriers also controls the e^- and h^+ kinetic and interaction energies of each exciton (Figure 6–4). Comparing Figure 6–2 and Figure 6–4(a-c), we find that, for each state, kinetic energies of both electron and hole (E_e and E_h) are independent of a_c when the carriers are in the shell, whereas they show strong dependence on a_c when the carriers

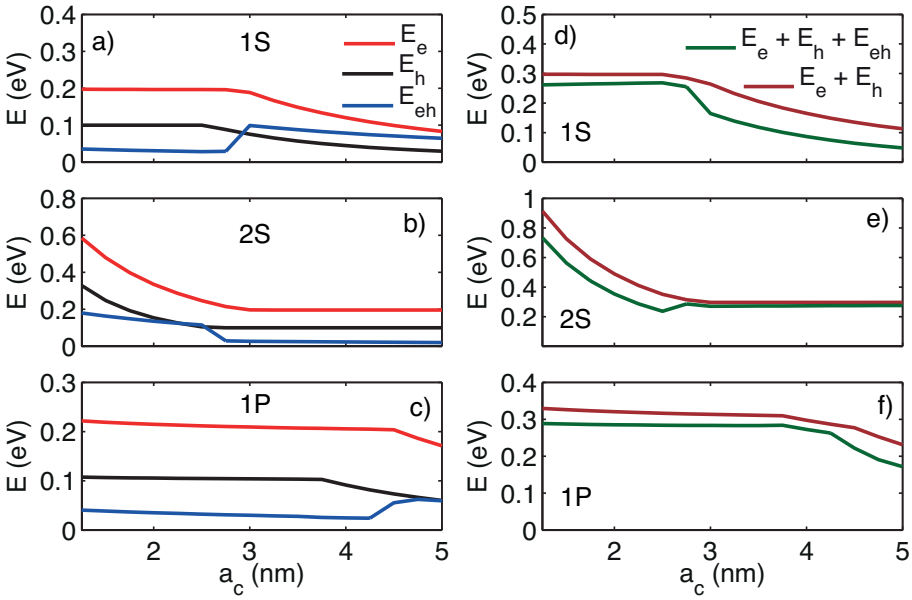

FIGURE 6–4: (a) 1S, (b) 2S and (c) 1P electron and hole kinetic energies (E_e and E_h) and their interaction energy (E_{eh}) as a function of core radius for $b_w = 2.5nm$ and 4ML of CdSe shell. E_e and E_h are independent core radius when carriers are in the shell. core-localized excitons have a larger electron-hole interaction as compared to shell-localized excitons. (d) 1S, (e) 2S and (f) 1P exciton energies with and without including E_{eh}. Regions where $E_{eh} > \{E_e, E_h\}$, the perturbative approach used to calculate E_{eh} may not be accurate. Reprinted with permission from [Tyagi, P. and Kambhampati, P., J. Phys. Chem. C 2012, 116, 8154 8160]. Copyright 2012, American Chemical Society.

are in the core. In contrast, E_{eh} does not show any a_c-dependence in either localization domain (core or shell) except in the transition (charge-separated) region. An interesting observation is that for each state, the $e^- - h^+$ interaction is stronger when both the e^- and h^+ are in the core than when they are both in the shell. This is consistent with the fact that the core provides three-dimensional confinement to the carriers whereas the shell confines them in only one dimension. We note that the perturbative approach used here does not give an accurate estimate of E_{eh} when E_{eh} becomes larger than kinetic energies of the carriers.

Similar calculations performed for different shell thicknesses ($1nm < t_s < 4nm$) show no qualitative difference from the results shown here, i.e. for different thicknesses of the shell, each exciton exhibits a transition from a core-localized state to a shell-localized state via a charge-separated state. Decreasing the shell thickness shifts the points of transition and makes the core to shell transition broader (similar to decreasing the barrier width b_w).

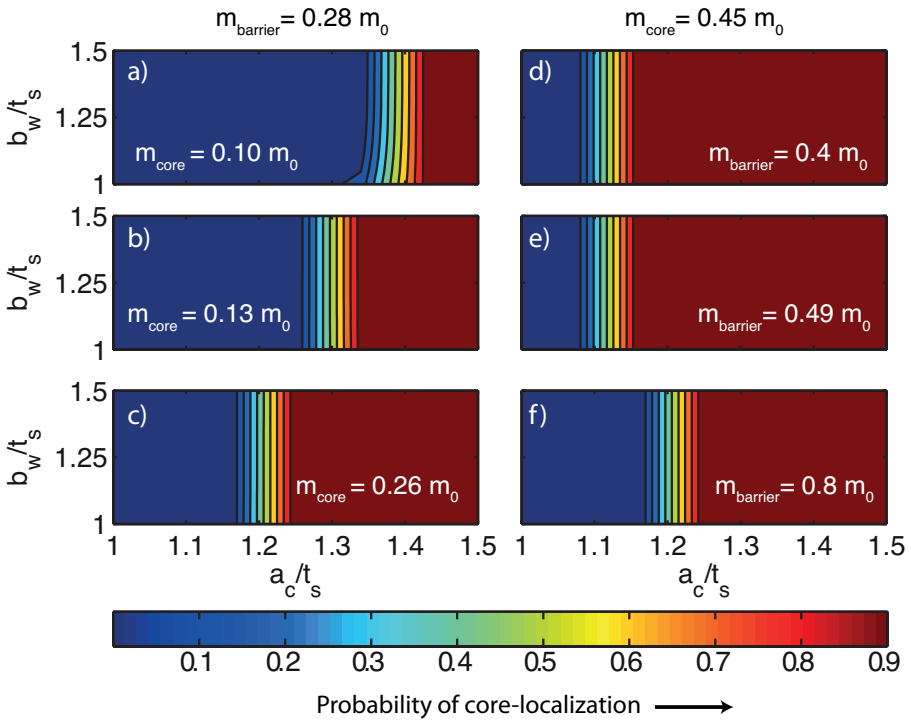

FIGURE 6–5: Effective mass-dependence of 1S carrier localization for fixed barrier height ($V_b = 0.9eV$) and shell thickness (ts = 4ML). (a)-(c) For fixed $m_{barrier}$, the width of the region where the particle is core-localized increases with increasing m_{core}. (d)-(f) For fixed mcore, increasing $m_{barrier}$ decreases the width of the region where the particle in is localized the core. The lighter the particle, the more susceptible it is to the change in effective mass. Reprinted with permission from [Tyagi, P. and Kambhampati, P., J. Phys. Chem. C 2012, 116, 8154 8160]. Copyright 2012, American Chemical Society.

On the basis of the discussion above, we conclude that CdSe/ZnS/CdSe nanostructures can be tuned to specific localization domains in parameter space depending on their desired function. One might also wish to manipulate the width of different localization regions based on the wavelengths and applications of interest. For instance, since the 1S charge-separated region is detrimental for light emitting applications, reducing the width of this region will make a bigger range of sizes (wavelengths) available for use. This can be accomplished by changing the material parameters, including effective mass, height and width of the barrier via e.g. alloying, doping or using a different material.

To provide design principles for nanostructures with desired functionalities, we investigate the dependence of wave function localization on material parameters. In particular, we study the dependence of carrier localization on the effective masses in the core and the barrier (m_{core} and $m_{barrier}$), and on the strength of the confinement potential. Figure 6–5(a-c) shows the probability of the particle being localized in the core for different values of m_{core} for fixed $m_{barrier}$. Our calculations show that for fixed $m_{barrier}$, as the particle becomes heavier in the core, the width of the region where it is core-localized increases. In Figure 6–5(d-f), we study the probability of core-localization of the particle as a function of $m_{barrier}$ for fixed m_{core}. Decreasing $m_{barrier}$ has the same effect as increasing m_{core}, i.e. it increases the width of the core-localized region. Also, the heavier the particle, the less it is influenced by the change in effective masses.

Figure 6–6 shows the dependence of carrier localization on barrier height, V_b. Decreasing V_b reduces the width of the core-localized region, and makes the

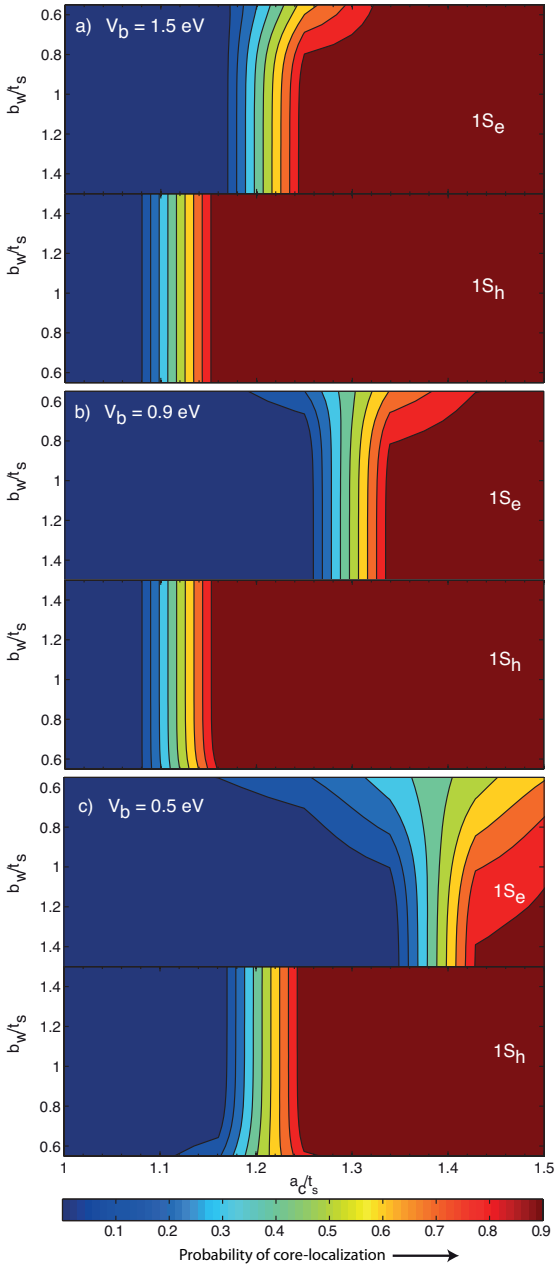

FIGURE 6–6: Dependence of 1S carrier localization on the height of the confinement barrier (V_b). As V_b decreases (from (a) to (c)), the core to shell transition becomes broader, and the width of the charge-separated region increases. The effect of barrier height is larger on the lighter particle (electron). Reprinted with permission from [Tyagi, P. and Kambhampati, P., J. Phys. Chem. C 2012, 116, 8154 8160]. Copyright 2012, American Chemical Society.

core to shell transition broader for both e^- and h^+. Because of their unequal effective masses, lowering V_b affects e^- and h^+ differently, and thereby increases the width of the charge-separated region. We note that reducing the barrier width, b_w has a similar effect on carrier localization as reducing V_b ; this is not surprising considering that decreasing either b_w or V_b decreases the barrier strength. Overall, the change in system parameters (m_{core}, $m_{barrier}$, b_w and V_b) has a larger effect on the lighter particle. This implies that starting with CdSe/ZnS/CdSe the width of the Type-II region can be increased by either (i) making e^- lighter in the core (Figure 6–5), or (ii) decreasing V_b (Figure 6–6). This can be achieved by using appropriate dopants in the core or using a barrier material with a lower band offset (e.g. ZnSe).

6.4 Conclusions

In this chapter, we demonstrated the capacity for a novel and potentially useful path toward spatial control of excitonic wave functions in core/barrier/shell nanostructures. By varying the core size in CdSe/ZnS/CdSe nanostructures, each of the low energy excitons (1S, 2S and 1P) can either be core-localized or shell-localized or prepared in a charge-separated state. Moreover, the width of each localization domain can be controlled by changing material parameters. Each localization regime is useful for specific applications including suppression of the radiative and the non-radiative relaxation processes, dual color emission, and low threshold and high bandwidth of optical gain. Our studies of effective mass, barrier height and barrier width dependence of different localization regimes offer directions for designing desired nanostructures in order to target specific applications. The effects of band-mixing on the electronic structure of bare CdSe QDs are well-understood, but little is known

about these effects in core/barrier/shell nanostructures [125,192,193]. We propose that atomistic calculations will provide a more quantitative description of electronic structure and carrier-carrier interactions in these systems and possibly reveal new phenomena [32,109]. These core/barrier/shell nanostructures hold promise for a wide range of applications and deserve further experimental and theoretical investigations. Nanostructures of different shapes (tetrapods/-nanorods) have also been shown to exhibit multiexcitonic dual-color emission due to suppressed Auger processes [13, 194]. A comparison of the dual-color emission property of nanostructures of different shapes (e.g. tetrapods vs core/barrier/shell) would give further insight into the processes that govern the spatial distribution of wave functions in quantum-confined systems.

'It is a capital mistake to theorize before one has data. Insensibly one begins to twist facts to suit theories, instead of theories to suit facts.'
- Sherlock Holmes

Chapter 7

Conclusions

In this thesis, we have shown that the surface of semiconductor nanostructures has a significant impact on their electronic and optical properties, and consequently on their observed TA spectra. From an experimental standpoint, this can lead to misinterpretation of TA signals, e.g. spurious multicarrier recombination times and "apparent" high CM yields. The analysis of TA signals presented here offers a possible explanation for the disagreement in the MEG literature. Surface-dependent TA studies also revealed the piezoelectric response of wurtzite CdSe QDs, in the form of enhanced electron-phonon coupling.

Our results highlight the need for better understanding of multicarrier interactions in semiconductor nanostructures, which form the basis for their potential applications. Following experiments can be performed to answer a few questions raised by this work:

1. *Carrier multiplication:* Low-fluence TA experiments with high pump photon energy, $E_{pump} > 2E_g$ could be performed QDs with varied surface conditions. Since ZnS-capped CdSe QDs are free of any surface artifacts, they should, in principle, give true measure of CM yields.

2. *Exciton-phonon coupling:* Due to their wurtzite lattice structure, CdSe QDs are inherently piezoelectric in nature. In our experiments, we observed an enhanced piezo coupling to acoustic phonons by conditioning the surface of CdSe QDs (Chapter 5). It would be interesting to investigate the effect of photo-treatment in non-piezoelectric QDs such as PbSe. Surface modifications may create a non-zero dipole moment and give rise to a measurable piezoelectric response in these dots. It is also conceivable that different exciton-phonon coupling mechanisms will become dominant in photo-treated state of these QDs.
3. *Multicarrier dynamics:* As shown in this work (Chapter 4), the measurement of multiexciton decay rates in a TA experiment is limited by the degeneracy of the probed state; moreover, the effect of state-filling appears as an induction time in the time-resolved TA signal. For CdSe/ZnS QDs studied here, this induction time is quite small ($2ps$). QDs with suppressed Auger decay, such as giant-NCs and alloyed nanostructures, may exhibit longer induction times. Such an experiment will serve to verify the limit imposed by state degeneracies on the measurement of multiexcitonic decays. Furthermore, decay times for higher excitons could be extracted by probing their corresponding excitonic states.
4. *Surface characterization:* Perhaps, the most crucial step in understanding the ligand-QD interface is the characterization of the QD surface. The current understanding of the QD surface is limited to a qualitative description of the dynamic interaction of ligands with the QD. Of relevance to this work is the question "what is the chemical effect of

photo-treating the QD?". Based on the available data, the current hypothesis is that the photo-treatment procedure increases the number of surface trap sites by adjusting the dynamic equilibrium of surface ligands. Also, few theoretical and experimental studies are able to indirectly measure the signature of photo-treatment such as photo-induced absorption in TA, decrease in nonradiative decay times, positive surface charge build-up in EFM, decrease in PL quantum yields etc. For a more direct measurement, it would be useful to conduct in-situ transmission electron microscopy, X-ray diffraction, inductively coupled plasma mass spectrometry and X-ray photoelectron spectroscopy to measure any change in QD shape, aggregation, lattice structure and presence of impurities.

Additionally, the sensitivity of the carrier wave functions to the nanocrystal surface, in conjuction with our ability to synthesize nanostructures with nearly atomic precision, opens up a range of opportunities in the field of wave function engineering.

In particular, CdSe/ZnS/CdSe core/barrier/shell heteronanostructures are a good model system to study the effect of confinement environment on carrier localization and to study coupling between two quantum systems (core and shell regions) separated by a barrier. One possible approach is the use of two-dimensional (2D) spectroscopy. This technique has been successfully employed to study many-body correlations in QWs and core-only QDs [193, 195–200], and energy transfer in photosynthetic complexes [201–204]. We expect that 2D electronic spectroscopy experiments on core/barrier/shell nanostructures

will be immensely helpful in revealing the nature of core-shell coupling and energy transfer processes [a].

Consequently, this information may enable researchers to manipulate the surface to design nanostructures that can more precisely control carrier wave functions for specific applications. Also, the theoretical framework for understanding multicarrier interactions core/barrier/shell nanostructures is not yet fully developed. It will be interesting to compare experimental results with theoretical predictions, which will help guide further experiments. With continued collaboration between synthesis, theory and experiments, we will hopefully soon be able to fully exploit the potential of these tiny promising materials.

[a] In our group, we have recently developed a 2D spectroscopy set-up consisting of dual pulse shapers, which is capable of complete amplitude, phase and polarization control of individual shaped pulses. The details of the 2D spectrometer and its application in studying many-body interactions in QDs are provided in Appendix A.

APPENDIX A

In this chapter, we present the recent work done by our group on two-dimensional spectroscopy. In collaboration with Fastlite[a], we have developed a dual pulse-shaper set-up capable of independent polarization, phase and amplitude control over each shaped pulse. By using active phase stabilization, we can achieve a phase stability of $\sim \lambda/314$ between the two pulse shapers, making the dual-shaper setup suitable for both two-quantum and one-quantum measurements. The set-up is compact and easily switchable between pump-probe and collinear geometries. We further illustrate the functionality of the dual shaper setup by performing two-color 2D visible spectroscopy on colloidal CdSe quantum dots in pump-probe geometry.

A.1 Introduction

Two-dimensional (2D) spectroscopy has emerged as a powerful tool that can determine the complete nonlinear optical response of a system up to third-order. By providing access to specific quantum mechanical pathways, it allows

[a]Fastlite, Centre scientifique d'Orsay-Bât.503, Plateau du Moulon-BP 45, Orsay (France)

for the measurement of vibrational and electronic couplings, energy transfer and multiexciton correlations, among other observables [195,201,203,205–207].

A basic 2D experiment is involves three light-matter interactions and is characterized by three time delays: the evolution or coherence time (t_{coh}), the waiting or population time (T_p) and the detection time (t). The evolution of the nonlinear polarization is observed by varying (t_{coh}) and measuring the emitted signal field during (t) with a heterodyne detection scheme. Finally, the data are represented in a 2D spectrum that describes the electronic transitions during t_{coh} and t (Figure A–1).

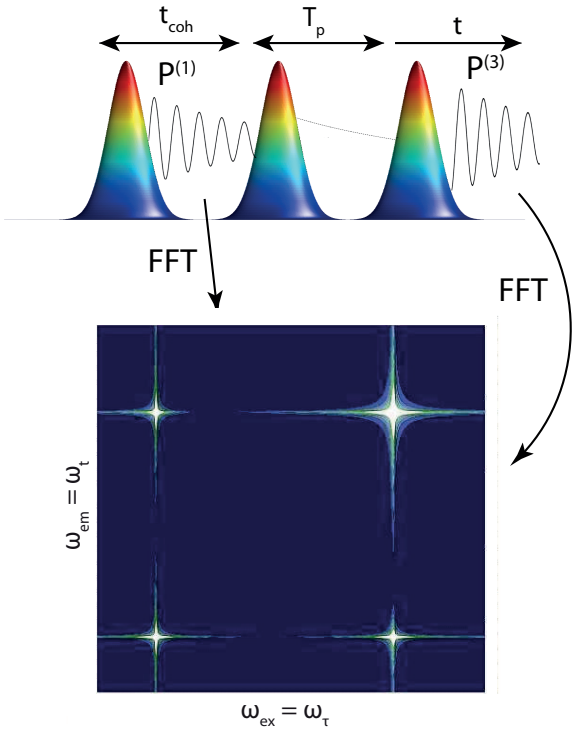

FIGURE A–1: Schematic of a 2D spectrum. $P^{(1)}$ and $P^{(3)}$ are the first and third order polarizations. FFT along t_{coh} and t gives the excitation (ω_{ex}) and emission (ω_{em}) frequency axes respectively

To characterize the complex signal field completely (i.e., obtain both amplitude and phase), interferometric measurement of the signal is required. This is accomplished by heterodyne detection of the emitted signal field with a fourth pulse called the local oscillator (LO). The signal is spatially and temporally overlapped with the LO and their spectral interferogram is detected at a monochromator.

A.1.1 Heterodyne detection

Let the electric fields of the LO (E_{LO}) and the emitted signal (E_{sig}) be defined as,

$$\begin{aligned} E_{LO}(r,t) &= E_{LO}(t)e^{\iota(k_{LO}r-\omega_{LO}t)} \\ E_{sig}(r,t) &= E_{sig}(t)e^{\iota(k_{sig}r-\omega_{sig}t)} \end{aligned} \quad , \tag{A.1}$$

where $\{k_{LO},\, \omega_{LO}\}$ and $\{k_{sig},\, \omega_{sig}\}$ are the wave vector and frequency of the LO and signal field respectively. Now, the total field at the detector can be written as,

$$E_{det}(r,t) = E_{LO}(r,t) + E_{sig}(r,t) \tag{A.2}$$

The time integrated signal at the detector is,

$$\begin{aligned} S_{det} &= \int \mathrm{d}t \mid E_{det}(r,t) \mid^2 \\ &\sim \mid E_{LO} \mid^2 + {E_{LO}}^* E_{sig} + {E_{sig}}^* E_{LO} + \mid E_{sig} \mid^2 \end{aligned} \tag{A.3}$$

We can ignore the first and the last terms because they are do not vary with time and represent a dc background. Therefore, the resultant heterodyne signal is given by

$$S_{het}(t) = 2Re\big[{E_{LO}}^* E_{sig} e^{-\iota(\omega_{LO}-\omega_{sig})t}\big] \tag{A.4}$$

The advantage of heterodyne detection is that the signal obtained is linear in $E_{LO}{}^{*}$ so increasing the amplitude of LO increases the magnitude of the detected signal for the same value of E_{sig}. In addition to this, this method also retains the phase information of the signal field as shown below:

$$\begin{aligned} S_{het}(t) &= A\cos(\omega_{LO}-\omega_{sig})t + B\sin(\omega_{LO}-\omega_{sig}) \quad \text{where,} \\ A &= 2Re(E_{LO}{}^{*}E_{sig}) \\ B &= 2Im(E_{LO}{}^{*}E_{sig}) \\ \frac{A}{B} &= \tan(\phi_{LO}-\phi_{sig}) \end{aligned} \tag{A.5}$$

where, $\phi_{LO}-\phi_{sig}$ is the phase difference between the LO and the signal field.

A.1.2 Different beam geometries for 2D spectroscopy

2D experiments can be implemented in different beam geometries, each having its advantages (Figure A–2). For example, the boxcar geometry offers background-free detection, thereby eliminating the need for phase cycling [208, 209]. The pump-probe geometry has the advantage of directly measuring perfectly phased 2D spectra as it emits both rephasing and non-rephasing components in the same direction [210–212]. The less common collinear geometry, desirable for its simplicity, is easy to extend to higher-order experiments, and allows for both fluorescence and transmission detected experiments [213, 214]. In our experiments, we use a modified version of the pump-probe geometry. A brief comparison between typical boxcar and pump-probe geometries is tabulated in Table A–1.

Traditionally, the pump-probe configuration employs a single pulse shaper to generate a phase-coherent pump pulse pair, and the probe pulse, which also acts as the local oscillator, is derived from a second source such as a

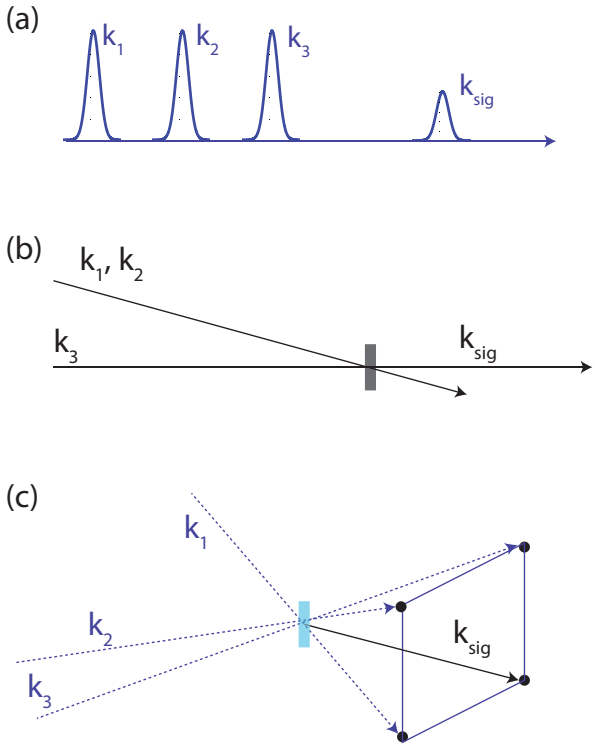

FIGURE A–2: (a) Collinear, (b) pump-probe, and (c) boxcar geometries used in a 2D spectroscopy experiment

white light continuum or a non-collinear OPA [210, 211, 215]. This configuration works well for one-quantum (1Q) measurements where the pump and the probe pulses are not required to be phase-coherent with each other. However, in the case of two-quantum (2Q) measurements, all optical pulses need to be phase-coherent which presents a challenge when using separate laser sources to produce pump and probe pulses [195]. Additionally, a single pulse shaper cannot independently control the polarization of each pump pulse and therefore, the polarization of the pump pulses must be identical. This restriction does not allow the use of optimal polarization selective schemes to completely eliminate the background as they require the polarizations of the two pump pulses to be orthogonal [216].

TABLE A–1: Comparison of boxcar and pump-probe geometries. R: rephasing, NR: non-rephasing.

Pump-probe	Boxcar
Implemented using acousto-optic modulators.	Implemented using diffraction-based pulse shaping or liquid crystal spatial light modulators.
R and NR components are emitted in the same direction, directly measuring the 2D absorptive spectrum.	R and NR emitted in different directions, and need to be phased and added to obtain the 2D spectrum.
Probe acts as the LO, so there are no phase stability issues between the LO/probe pulse pair. The pump pulses are produced by an AOM, which maintains good phase stability between the pump pulse pair. However, the LO/probe pair and pump pulses are not phase-coherent with eachother.	All four beams travel through the same set of optics such that the relative path length of all beams is interferometrically stable, and all four pulses are phase-coherent.
Unwanted TA signals are emitted in the same direction as the desired $2D$ signal.	No unwanted background signals.

We overcome these limitations by using dual pulse shapers (Acousto-Optic Programmable Dispersive Filters (AOPDFs): WR25, low-jitter operation), which enable independent polarization, phase and amplitude control over each pulse (Figure A–3). In this configuration, we can achieve a phase stability of $\sim \lambda/314$ between the two shapers by using active phase stabilization. In addition to being extremely compact, this set-up is easily switchable between

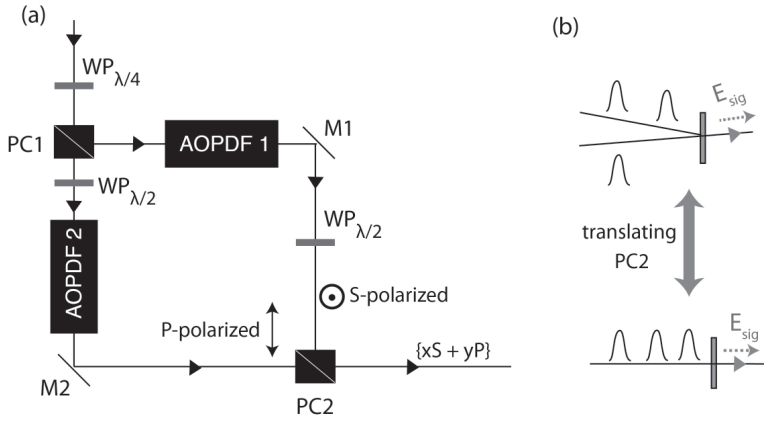

FIGURE A–3: (a) The outputs of the two OPAs are orthogonally polarized and are separated using a polarizing cube (PC1). Each polarization component is then sent through an AOPDF to produce shaped pulses, which are finally combined using PC2. (b) Translating PC2 spatially separates the shaped pulses from the two AOPDFs, making it easy to switch between the pump-probe (top) and collinear (bottom) geometries.

pump-probe and collinear geometries, allowing for detection in both phase-cycling and phase-matching arrangements (Figure A–3). Fast update rates of the AOPDF enable single-shot measurements at 1 kHz, significantly reducing the data acquisition time. Also, we compress the unshaped pump pulse before the shaping set-up using prism compressors; this compensates for part of the dispersion of the AOPDFs and allows us to produce a delay of upto 4 ps between the shaped pulses. Finally, we demonstrate the functionality of the dual pulse shaper set-up by performing 2D visible spectroscopy on CdSe quantum dots (QDs).

A.2 Experiment

The ultrafast laser source used in these experiments is an amplified Ti-Sapphire laser system (2.5 mJ, 70 fs, 800 nm, 1 kHz). The regenerative amplifier is used to pump two optical parametric amplifiers (OPAs), which were

used to produce the pump and the probe pulses. A block diagram of our pulse shaping set-up is shown in Figure A–3a. The output of one OPA was sent to AOPDF 1, which produces the pump pulse pair (532 nm, 10 nm FWHM), and the other OPA was used to produce the probe pulse (616 nm, 25 nm FWHM), which was shaped by AOPDF 2.

In pump-probe geometry, the signal field is emitted in the same direction as the probe and was resolved at 1 kHz using Acton SP2500i spectrometer and PIXIS 100B CCD. A color filter was used to block the pump pulses from reaching the detector. The instrument response function (IRF) was measured by cross-correlation between the pump and the probe pulses and was found to be $\sim$ 60 fs. The coherence time (t_{coh}) was scanned from 0 to 200 fs in 0.4 fs time steps for a fixed population time (T_p). The energy of the pump and the probe pulses were 25 nJ and 2.5 nJ respectively. Samples of colloidal CdSe QDs dispersed in toluene were purchased from NN-Labs; the sample was continuously flowed through a 1 mm path length flow cell during the experiment. The optical density of the sample was $\sim$ 0.2.

A.3 Results

Previous experiments have shown that a pulse pair produced by single Dazzler pulse shaper can maintain a phase stability of approximately $\lambda/85$ at 530 nm over 3 hours [211]. However, a single Dazzler set-up does not allow for 2Q measurements in pump-probe geometry and also lacks the ability to independently control the polarization of individual pump pulses. To overcome these limitations, we use two Dazzlers with active phase stabilization to achieve high phase stability between the pulse pair produced by them. Basically, a spectral interferogram between the two pulses is measured to determine

their relative phase difference, and the required phase correction is applied in subsequent shots to achieve the target phase difference.

The phase stability measurements were performed using spectral interferometry. Figure A–4 shows a comparison of the phase stability produced by single AOPDF without active phase stabilization and two AOPDFs with active phase stabilization at 100 Hz (i.e. using every 10^{th} shot to determine the phase correction). In both cases, the shaped pulses had identical spectra and the measurements were made at 630 nm. Using active phase stabilization, we can produce a phase stability of $\sim \lambda/314$ (at 630 nm over 1 hour) between pulses produced from the two AOPDFs (Figure A–4a), which is, to our knowledge, the highest reported phase stability to date for pulse pairs generated by AOPDFs. In fact, it surpasses the phase stability produced by a single AOPDF (Figure A–4b). By maintaining excellent phase stability between two AOPDFs, this set-up extends the application of pulse shapers to 2Q measurements.

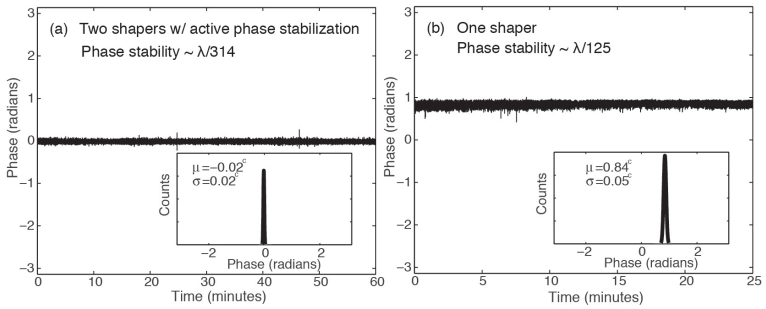

FIGURE A–4: Single-shot (1 kHz) phase measurements (using spectral interferometry) between two pulses (a) from two AOPDFs using active phase stabilization at 100Hz over a period of 60 minutes, and (b) from a single AOPDF over a period of 25 minutes.

Another important application of our set-up is the ability to independently control the polarization of individual pump pulses at 1 kHz. This is

accomplished by combining the pulses produced from the two shapers using a polarizing cube. Since the pulses shaped by the two AOPDFs have orthogonal polarizations (Figure A–3a), by controlling the spectral phase and amplitude of each of these pulses, we can achieve any desired polarization state. Zanni and coworkers have successfully implemented this principle for polarization control in the mid-infrared (mid-IR) [217]. They use a wire-grid polarizer for combining mid-IR pulses whereas we use a polarizing cube (PC2) for the same purpose in the visible range. PC2 combines the pulses from the two AOPDFs while the feedback loop ensures high phase stability between the two Dazzlers, which is critical to achieve polarization shaping. The translation of PC2 controls the spatial overlap between the two pulses from the two Dazzlers, thereby allowing us to easily switch between collinear and pump-probe geometries. When the pulse pair is perfectly overlapped, collinear polarization shaped pulses are produced. However, when the pulse pair is spatially separated, we lose the ability to independently control the polarization of the individual pump pulses while still maintaining excellent phase stability between the two shapers necessary to perform 2Q experiments. This implies that when using Dazzlers for polarization shaping of individual pump pulses, we can *(i)* either use a separate laser source for the probe pulse and perform the 2D experiments in pump-probe geometry, *(ii)* or use the Dazzlers to shape both pump and probe pulses and perform the experiment in collinear geometry.

To characterize the pulse polarization, we employ a simplified Mueller ellipsometer shown in Figure A–5a. The ellipsometer uses a beam splitter (BS1) and two Wollaston prisms (W1 and W2) to measure two quadratures of the

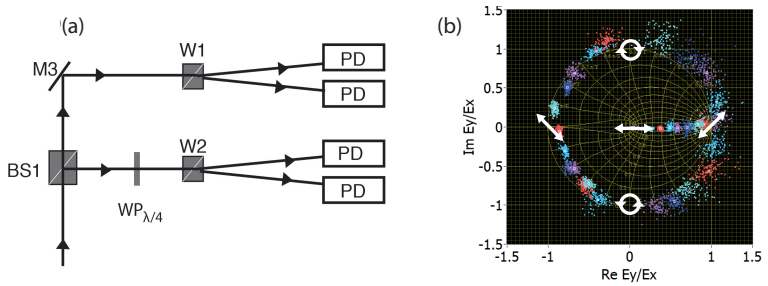

FIGURE A–5: (a) Polarization characterization is achieved by splitting the shaped pulse using a beam splitter (BS1) and subsequently Wollaston prisms (W1, W2) and measuring the intensity of the circularly and linearly polarized components using photo-diodes (PD). (b) Polarization measurements using the ellipsometer shown in (a). The data points are presented on a Poincar sphere for easy visualization. 100 shots are acquired for each phase and amplitude setting. Both linearly and circularly polarized pulses can be produced using the shapers shown in Figure A–3a

polarization state in both linear and circular polarization bases, thus characterizing the polarization of the shaped pulses. Figure A–5b represents the polarization measurements on a Poincar sphere for easy visualization. By controlling the phase and amplitude of pulses from each AOPDF and combining them using PC2, we can prepare pulses in the desired polarization state. By varying $\Delta\phi$ from 0 to 2π (in steps of $\pi/10$), we obtain the data spanning the circumference of the Poincaré sphere. These data points correspond to polarization states of varying ellipticity, from right-handed to left handed circular polarization. By varying the amplitude of one of the pulses from 0 to 1, we obtain data along the equator, which corresponds to linear polarization states.

Finally, we demonstrate the functionality of the dual AOPDF scheme for 2D visible spectroscopy by using colloidal CdSe QDs dispersed in toluene as a test sample. The experiments were performed in pump-probe geometry, with AOPDF 1 producing the pump pulse pair and AOPDF 2 producing the probe

pulse. The pump pulses were tuned to the 1P exciton peak while the probe pulse was set to 1S exciton (Figure A–6a). The polarization of the probe pulse was set to 45° relative to the pump pulses. Since the signal field is emitted collinear to the probe pulse that acts as the local oscillator, an analyzer was used to block probe pulse before the detector by setting it at 85° relative to the probe pulse. This allows us to increase the probe intensity without saturating the detector and the small amount of probe passing through the analyzer allows for heterodyne detection. This polarization scheme significantly enhances the signal to noise of the 2D spectrum by predominantly measuring (X+Y)(X+Y)XY = XYXY+YXXY components (where X and Y denote 0° and 90° polarizations respectively) [206, 211, 216]. A small contribution from (X+Y)(X+Y)XX = XXXX + YYXX is also present because the analyzer is not perfectly perpendicular to the probe polarization.

The desired 1Q 2D absorptive spectrum is the sum of the rephasing (R) and non-rephasing (NR) signals [218]. In the pump-probe configuration, both of these signals are emitted in the direction of the probe pulse. Thus, the detected signal in pump-probe geometry directly measures the 2D spectrum unlike the non-collinear geometries where NR and R signals are emitted in different phase-matched directions and must be separately measured, phased and added to obtain the 2D absorptive spectrum [219]. The disadvantage of the pump-probe geometry, however, is that it is not background-free. The unwanted transient absorption signals due to two light-matter interactions from single pump pulse and one from the probe pulse are also emitted in the probe direction. In order to eliminate the transient absorption background, we employ a two-step phase cycling scheme introduced by Zanni and coworkers [206].

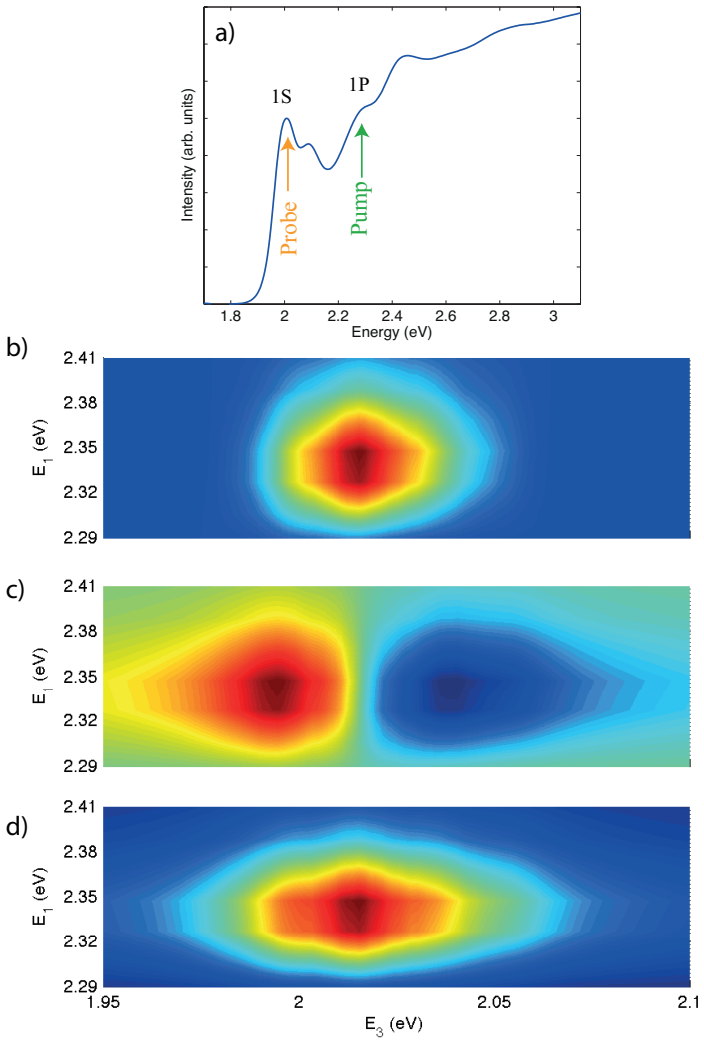

FIGURE A–6: (a) Linear absorption spectrum of CdSe QDs. The arrows indicate the pump and probe pulse energies. (b) Real, (c) Imaginary and (d) Absolute parts of the 2D absorptive spectrum of CdSe QDs at $T_p = 500$ fs.

The phase of the emitted 1Q signal is given by

$$\phi_{sig} = \pm(\phi_1 - \phi_2) + \phi_3 - \phi_{LO} \quad , \tag{A.6}$$

where, $\phi_{1(2)}$ is the phase of the first (second) pump pulse, ϕ_3 is the phase of the probe pulse and ϕ_{LO} is the phase of the local oscillator pulse, $\pm$ signs refer to NR and R components respectively. In pump-probe geometry, since the probe pulse acts as the local oscillator i.e. $\phi_3 = \phi_{LO}$, the phase of the NR and R signals is independent of ϕ_3 and is equal to $\pm(\phi_1 - \phi_2)$ respectively. From the discussion above, it follows that changing $\Delta\phi$ by 'δ' changes the phase of the desired 2D signal by the 'δ' as well, while keeping the phase of the transient absorption signal unchanged. Therefore, subtracting measured signals corresponding to $\Delta\phi = 0$ and $\Delta\phi = \pi$ will enhance the desired 2D signal while eliminating the transient absorption background. Figure A–7 shows the detected signal as a function of t_{coh} for $\Delta\phi = 0$ and $\Delta\phi = \pi$ at a probe wavelength of 616 nm and $T_p = 250$ fs. Changing $\Delta\phi$ by π changes the phase of the desired oscillatory signal by π as well while the background remains unchanged (red and blue curves). The subtracted signal is shown as the black curve in Figure A–7. This phase cycling procedure enhances the amplitude of the desired signal while simultaneously eliminating the background that does not depend of $\Delta\phi$.

To obtain the absorptive 2D spectrum, we acquire data as a function of t_{coh} at fixed T_p for $\Delta\phi = 0$ and $\Delta\phi = \pi$. Since we spectrally resolve the heterodyned signal using a spectrometer and CCD, the signal is collected in the frequency domain i.e. the detected signal can be written as $S(t_{coh}, T_p, \lambda_3; \Delta\phi)$. The first step is to obtain the background-free signal, $S(t_{coh}, T_p, \lambda_3) = S(t_{coh}, T_p, \lambda_3; 0) - S(t_{coh}, T_p, \lambda_3; \pi)$. We then perform a Jacobian transformation to obtain the data as a function of frequency ν_3, followed by interpolation to get equally spaced intervals along ν_3, which gives us $S(t_{coh}, T_p, f_3)$. We further subject

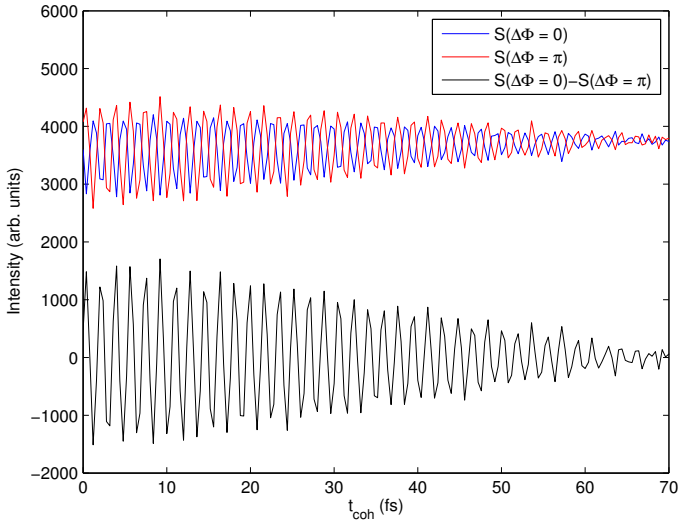

FIGURE A–7: Demonstration of a two-step phase cycling scheme. The measured raw signal as a function of coherence time at $\lambda_{probe} = 616$nm and $T_p = 250$ fs for $\Delta\phi = 0$ (blue) and $\Delta\phi = \pi$ (red). Subtraction of the signals corresponding to $\Delta\phi = 0$ and $\Delta\phi = \pi$ enhances the amplitude of the desired 2D signal while eliminating the background (black).

our data to symmetry and causality conditions as proposed by Ogilvie and coworkers [211]. Since the first two pulses are essentially interchangeable, the data must be symmetric with respect to $t_{coh} = 0$ or in other words, the Fourier transform of $S(t_{coh}, T_p, f_3)$ along t_{coh} must be purely real. We enforce this symmetry condition by selecting the real part of the Fourier transform of $S(t_{coh}, T_p, f_3)$ (i.e. $\mathrm{Re}[S(t_{coh}, T_p, f_3))]$) and inverse Fourier transforming it to obtain $S(\tau_{coh}, T_p, f_3)$ which is symmetric with respect to $\tau_{coh} = 0$. Next, we inverse Fourier transform this signal along f_3 to obtain $S(\tau_{coh}, T_p, t_3)$. Since no signal is emitted at negative t_3 i.e. if the probe pulse interacts with the sample before the pump pulse, $S(\tau_{coh}, T_p, t_3) = 0$ for $t_3 < 0$. We apply this causality condition by multiplying $S(\tau_{coh}, T_p, t_3)$ with the Heaviside step function $\Theta(t_3)$.

Finally, Fourier transforming the resulting signal along both τ_{coh} and t_3 gives us the complex absorptive 2D spectrum $S(\nu_1, T_p, \nu_3)$.

Figure A–6(b-d) shows the absorptive 2D spectrum obtained using the above analysis at $T_p = 500$ fs. The horizontal axis corresponds to the emission axis obtained by Fourier transformation with respect to t_3, and the vertical axis, corresponding to excitation, is obtained by Fourier transformation along the t_{coh} axis. The two-color approach measures the coupling between different excitonic transitions, which in this case are 1P and 1S excitons (Figure A–6a). The real part of the 2D spectrum has an absorptive lineshape whereas the imaginary part is dispersive in character. The population time dependence of the 2D spectrum is shown in Figure A–8. The peak at $(E_1, E_3) =$ (2.340 eV, 2.015 eV) broadens and decreases in intensity with increasing T_p which is indicative of population relaxation. While these 2D spectra are shown merely to demonstrate the functionality of the dual-shaper set-up, we note that the observed lineshape and population relaxation are consistent with previous measurements [193]. The 2D measurements presented here do not utilize the polarization control capabilities of our set-up. A comprehensive analysis of polarization dependent signals will be presented in subsequent experiments from our group. In pump-probe geometry, one can further extract R and NR signals from the measured 2D spectrum by employing three-step phase cycling schemes [211, 220, 221], whereas a fully collinear geometry requires at least ten step-phase cycling procedure to extract desired signals [213, 222].

In conclusion, we have demonstrated a dual-shaper set-up with active phase stabilization. This configuration maintains excellent phase stability between the two pulse shapers, thereby extending the application of AOPDFs

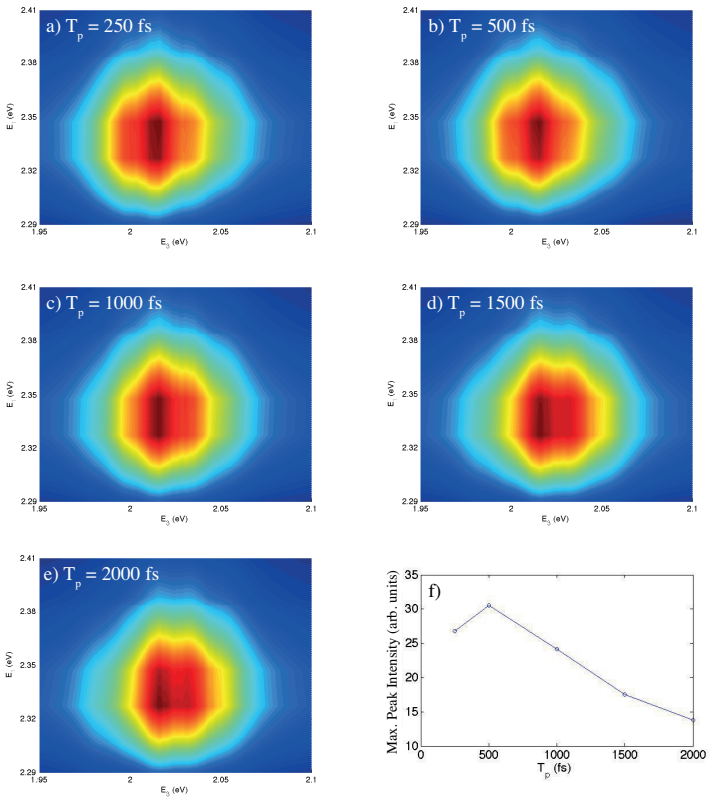

FIGURE A–8: (a-e) Absolute part of 2D absorptive spectra for CdSe quantum dots for T_p = 250 fs, 500 fs, 1000 fs, 1500 fs, and 2000 fs. (f) Maximum intensity of the peak at (E_1, E_3) = (2.340 eV, 2.015 eV) as a function of population time.

to 2Q measurements. The set-up further allows us to independently control the polarization of individual shaped pulses. Previously, 2D spectroscopy has been used to study many-body effects in quantum wells and excitonic fine-structure in QDs by mapping multiexcitonic interactions on a two dimensional plane [193, 195, 197–200, 223]. By offering polarization control over individual shaped pulses, this dual shaper set-up further allows for the study of optical selection rules in QDs.

Bibliography

[1] Tyagi, P.; Cooney, R. R.; Sewall, S. L.; Sagar, D. M.; Saari, J. I.; Kambhampati, P. *Nano Letters* **2010**, *10*, 3062–3067.

[2] Tyagi, P.; Kambhampati, P. *Journal of Chemical Physics* **2011**, *134*, 094706–10.

[3] Tyagi, P.; Kambhampati, P. *The Journal of Physical Chemistry C* **2012**, *116*, 8154–8160.

[4] Tyagi, P.; Saari, J. I.; Walsh, B.; Kabir, A.; Crozatier, V.; Forget, N.; Kambhampati, P. *Submitted* **2013**.

[5] Kim, S.; Fisher, B.; Eisler, H.-J.; Bawendi, M. *Journal of the American Chemical Society* **2003**, *125*, 11466–11467.

[6] Balet, L. P.; Ivanov, S. A.; Piryatinski, A.; Achermann, M.; Klimov, V. I. *Nano Letters* **2004**, *4*, 1485–1488.

[7] Battaglia, D.; Blackman, B.; Peng, X. *Journal of the American Chemical Society* **2005**, *127*, 10889–10897.

[8] Muller, J.; Lupton, J. M.; Lagoudakis, P. G.; Schindler, F.; Koeppe, R.; Rogach, A. L.; Feldmann, J.; Talapin, D. V.; Weller, H. *Nano Letters* **2005**, *5*, 2044–9.

[9] Sapra, S.; Mayilo, S.; Klar, T. .; Rogach, A. .; Feldmann, J. *Advanced Materials* **2007**, *19*, 569–572.

[10] Dias, E. A.; Sewall, S. L.; Kambhampati, P. *Journal of Physical Chemistry C* **2007**, *111*, 708–713.

[11] Demir, H. V.; Nizamoglu, S.; Mutlugun, E.; Ozel, T.; Sapra, S.; Gaponik, N.; Eychmuller, A. *Nanotechnology* **2008**, *19*, 335203.

[12] Garcia-Santamaria, F.; Chen, Y.; Vela, J.; Schaller, R. D.; Hollingsworth, J. A.; Klimov, V. I. *Nano Letters* **2009**.

[13] Choi, C. L.; Li, H.; Olson, A. C. K.; Jain, P. K.; Sivasankar, S.; Alivisatos, A. P. *Nano Letters* **2011**, *11*, 2358–2362.

[14] Qin, W.; Shah, R. A.; Guyot-Sionnest, P. *ACS Nano* **2012**, *6*, 912–918.

[15] Nozik, A. J. *Annual Review of Physical Chemistry* **2001**, *52*, 193–231.

[16] Nozik, A. J. *Physica E: Low-Dimensional Systems & Nanostructures (Amsterdam, Netherlands)* **2002**, *14*, 115–120.

[17] Coe, S.; Woo, W.-K.; Bawendi, M.; Bulovic, V. *Nature* **2002**, *420*, 800–803.

[18] Bruchez, J., Marcel; Moronne, M.; Gin, P.; Weiss, S.; Alivisatos, A. P. *Science (Washington, D. C.)* **1998**, *281*, 2013–2016.

[19] Wu, X.; Liu, H.; Liu, J.; Haley, J. A., K. N.and Treadway; Larson, J. P.; Ge, N.; Peale, F.; Bruchez, M. P. *Nature Biotechnology* **2003**, *21*, 41–46.

[20] Jaiswal, J. K.; Mattoussi, H.; Mauro, J. M.; Simon, S. M. *Nature Biotechnology* **2003**, *21*, 47–51.

[21] Gao, X.; Cui, Y.; Levenson, R. M.; Chung, L. W.; Nie, S. *Nature Biotechnology* **2004**, *22*, 969–976.

[22] Benisty, H.; Sotomayor-Torres, C.; Weisbuch, C. *Physical Review B: Condensed Matter and Materials Physics* **1991**, *44*, 10945–10948.

[23] Bockelmann, U.; Bastard, G. *Physical Review B: Condensed Matter and Materials Physics* **1990**, *42*, 8947–8951.

[24] Cooney, R. R.; Sewall, S. L.; Anderson, K. E. H.; Dias, E. A.; Kambhampati, P. *Physical Review Letters* **2007**, *98*, 177403–4.

[25] Kambhampati, P. *Accounts of Chemical Research* **2011**, *44*, 1–13.

[26] Guyot-Sionnest, P.; Shim, M.; Matranga, C.; Hines, M. *Physical Review B: Condensed Matter and Materials Physics* **1999**, *60*, R2181–R2184.

[27] Klimov, V. I.; McBranch, D. W. *Physical Review Letters* **1998**, *80*, 4028–4031.

[28] Klimov, V. I.; Mikhailovsky, A. A.; McBranch, D. W.; Leatherdale, C. A.; Bawendi, M. G. *Physical Review B: Condensed Matter and Materials Physics* **2000**, *61*, R13349–R13352.

[29] Klimov, V. I.; Mikhailovsky, A. A.; McBranch, D. W.; Leatherdale, C. A.; Bawendi, M. G. *Science* **2000**, *287*, 1011–1013.

[30] Sewall, S. L.; Cooney, R. R.; Anderson, K. E. H.; Dias, E. A.; Kambhampati, P. *Physical Review B* **2006**, *74*, 235328.

[31] Efros, A. L.; Kharchenko, V. A.; Rosen, M. *Solid State Communications* **1995**, *93*, 281–4.

[32] Wang, L.-W.; Califano, M.; Zunger, A.; Franceschetti, A. *Physical Review Letters* **2003**, *91*, 056404/1–056404/4.

[33] Califano, M.; Bester, G.; Zunger, A. *Nano Letters* **2003**, *3*, 1197–1202.

[34] Chepic, D.; Efros, A.; Ekimov, A.; Ivanov, M.; Kharchenko, V.; Kudriavtsev, I.; Yazeva, T. *Journal of Luminescence* **1990**, *47*, 113 – 127.

[35] Hendry, E.; Koeberg, M.; Wang, F.; Zhang, H.; de Mello Donega, C.; Vanmaekelbergh, D.; Bonn, M. *Physical Review Letters* **2006**, *96*, 057408/1–057408/4.

[36] Efros, A. L.; Rosen, M. *Physical Review Letters* **1997**, *78*, 1110–1113.

[37] Frantsuzov, P. A.; Marcus, R. A. *Physical Review B* **2005**, *72*, 155321/1–155321/10.

[38] Jha, P. P.; Guyot-Sionnest, P. *ACS Nano* **2009**, *3*, 1011–1015.

[39] Zhao, J.; Nair, G.; Fisher, B. R.; Bawendi, M. G. *Physical Review Letters* **2010**, *104*.

[40] Cordones, A. A.; Bixby, T. J.; Leone, S. R. *The Journal of Physical Chemistry C* **2011**, *115*, 6341–6349.

[41] Cordones, A. A.; Bixby, T. J.; Leone, S. R. *Nano Letters* **2011**, *11*, 3366–3369.

[42] Dingle, R.; Henry, C.; *Quantum effects in heterostructure lasers*; Patent; 1976; US 3982207.

[43] Klimov, V. I.; Mikhailovsky, A. A.; Xu, S.; Malko, A.; Hollingsworth, J. A.; Leatherdale, C. A.; Eisler, H.; Bawendi, M. G. *Science* **2000**, *290*, 314–7.

[44] Malko, A. V.; Mikhailovsky, A. A.; Petruska, M. A.; Hollingsworth, J. A.; Klimov, V. I. *Journal of Physical Chemistry B* **2004**, *108*, 5250–5255.

[45] Klimov, V. I. *Journal of Physical Chemistry B* **2006**, *110*, 16827–16845.

[46] Klimov, V. I. *Annual Review of Physical Chemistry* **2007**, *58*, 635–673.

[47] Cooney, R. R.; Sewall, S. L.; Sagar, D. M.; Kambhampati, P. *Physical Review Letters* **2009**, *102*, 127404–4.

[48] Cooney, R. R.; Sewall, S. L.; Sagar, D. M.; Kambhampati, P. *Journal of Chemical Physics* **2009**, *131*, 164706.

[49] Kambhampati, P. *The Journal of Physical Chemistry C* **2011**, *115*, 22089–22109.

[50] Dias, E. A.; Saari, J. I.; Tyagi, P.; Kambhampati, P. *The Journal of Physical Chemistry C* **2012**, *116*, 5407–5413.

[51] Schaller, R. D.; Klimov, V. I. *Physical Review Letters* **2004**, *92*, 186601/1–186601/4.

[52] Schaller, R. D.; Agranovich, V. M.; Klimov, V. I. *Nature Physics* **2005**, *1*, 189–194.

[53] Ellingson, R. J.; Beard, M. C.; Johnson, J. C.; Yu, P.; Micic, O. I.; Nozik, A. J.; Shabaev, A.; Efros, A. L. *Nano Letters* **2005**, *5*, 865–871.

[54] Schaller, R. D.; Sykora, M.; Pietryga, J. M.; Klimov, V. I. *Nano Letters* **2006**, *6*, 424–429.

[55] Ueda, A.; Matsuda, K.; Tayagaki, T.; Kanemitsu, Y. *Applied Physics Letters* **2008**, *92*, 233105.

[56] Ben-Lulu, M.; Mocatta, D.; Bonn, M.; Banin, U.; Ruhman, S. *Nano Letters* **2008**, *8*, 1207–1211.

[57] McGuire, J. A.; Joo, J.; Pietryga, J. M.; Schaller, R. D.; Klimov, V. I. *Accounts of Chemical Research* **2008**, *41*, 1810–1819.

[58] Nair, G.; Geyer, S. M.; Chang, L. Y.; Bawendi, M. G. *Physical Review B* **2008**, *78*, 125325.

[59] Nozik, A. J. *Chemical Physics Letters* **2008**, *457*, 3–11.

[60] McGuire, J. A.; Sykora, M.; Joo, J.; Pietryga, J. M.; Klimov, V. I. *Nano Letters* **2010**, *10*, 2049–2057.

[61] Nair, G.; Bawendi, M. G. *Physical Review B* **2007**, *76*.

[62] Schaller, R. D.; Sykora, M.; Jeong, S.; Klimov, V. I. *Journal of Physical Chemistry B* **2006**, *110*, 25332–25338.

[63] Pijpers, J. J. H.; Hendry, E.; Milder, M. T. W.; Fanciulli, R.; Savolainen, J.; Herek, J. L.; Vanmaekelbergh, D.; Ruhman, S.; Mocatta, D.; Oron, D.; Aharoni, A.; Banin, U.; Bonn, M. *Journal of Physical Chemistry C* **2007**, *111*, 4146–4152.

[64] Pijpers, J. J. H.; Hendry, E.; Milder, M. T. W.; Fanciulli, R.; Savolainen, J.; Herek, J. L.; Vanmaekelbergh, D.; Ruhman, S.; Mocatta, D.; Oron, D.; Aharoni, A.; Banin, U.; Bonn, M. *The Journal of Physical Chemistry C* **2008**, *112*, 4783–4784.

[65] Bardeen, J.; Cooper, L. N.; Schrieffer, J. R. *Phys. Rev.* **1957**, *106*, 162–164.

[66] Perner, M.; Gresillon, S.; Mrz, J.; von Plessen, G.; Feldmann, J.; Porstendorfer, J.; Berg, K. J.; Berg, G. *Physical Review Letters* **2000**, *85*, 792.

[67] Hartland, G. V. *Physical Chemistry Chemical Physics* **2004**, *6*, 5263–5274.

[68] Muskens, O. L.; Del Fatti, N.; Vallee, F. *Nano Lett. FIELD Full Journal Title:Nano Letters* **2006**, *6*, 552–556.

[69] Hartland, G. V. *Annual Review of Physical Chemistry* **2006**, *57*, 403–430; PMID: 16599816.

[70] Sun, C.-K.; Liang, J.-C.; Yu, X.-Y. *Physical Review Letters* **2000**, *84*, 179.

[71] Özgür, U.; Lee, C.-W.; Everitt, H. O. *Physical Review Letters* **2001**, *86*, 5604.

[72] Yahng, J. S.; Jho, Y. D.; Yee, K. J.; Oh, E.; Woo, J. C.; Kim, D. S.; Sanders, G. D.; Stanton, C. J. *Applied Physics Letters* **2002**, *80*, 4723–4725.

[73] Kim, C. S.; Kim, J. H.; Jeong, H.; Jho, Y. D.; Kwon, H. K.; Lee, H. S.; Park, J. S.; Song, K.; Kim, S. H.; Kim, Y. J.; Lee, D.; Yee, K. J. *Applied Physics Letters* **2012**, *100*, 101105.

[74] Bartels, A.; Dekorsy, T.; Kurz, H.; Köhler, K. *Applied Physics Letters* **1998**, *72*, 2844.

[75] Efros, A. L.; Ekimov, A. I.; Kozlowski, F.; Petrova-Koch, V.; Schmidbaur, H.; Shumilov, S. *Solid State Communications* **1991**, *78*, 853–6.

[76] Alivisatos, A. P.; Harris, T. D.; Carroll, P. J.; Steigerwald, M. L.; Brus, L. E. *Journal of Chemical Physics* **1989**, *90*, 3463–8.

[77] Shiang, J. J.; Risbud, S. H.; Alivisatos, A. P. *Journal of Chemical Physics* **1993**, *98*, 8432–42.

[78] Takagahara, T. *Journal of Luminescence* **1996**, *70*, 129–143.

[79] Banin, U.; Cerullo, G.; Guzelian, A. A.; Alivisatos, A. P.; Shank, C. V. *Physical Review B* **1997**, *55*, 7059–7067.

[80] Heitz, R.; Mukhametzhanov, I.; Stier, O.; Madhukar, A.; Bimberg, D. *Physical Review Letters* **1999**, *83*, 4654.

[81] Krauss, T. D.; Wise, F. W. *Physical Review Letters* **1997**, *79*, 5102–5105.

[82] Cerullo, G.; De Silvestri, S.; Banin, U. *Physical Review B* **1999**, *60*, 1928–1932.

[83] Sagar, D. M.; Cooney, R. R.; Sewall, S. L.; Dias, E. A.; Barsan, M. M.; Butler, I. S.; Kambhampati, P. *Physical Review B (Condensed Matter and Materials Physics)* **2008**, *77*, 235321–14.

[84] Sagar, D. M.; Cooney, R. R.; Sewall, S. L.; Kambhampati, P. *Journal of Physical Chemistry C* **2008**, *112*, 9124–9127.

[85] Creti, A.; Anni, M.; Zavelani-Rossi, M.; Lanzani, G.; Manna, L.; Lomascolo, M. *Journal of Optics A: Pure and Applied Optics* **2008**, *10*, 064004.

[86] Dworak, L.; Matylitsky, V. V.; Braun, M.; Wachtveitl, J. *Physical Review Letters* **2011**, *107*, 247401.

[87] Sewall, S. L.; Cooney, R. R.; Anderson, K. E. H.; Dias, E. A.; Sagar, D. M.; Kambhampati, P. *Journal of Chemical Physics* **2008**, *129*, 084701.

[88] Li, S.; Steigerwald, M. L.; Brus, L. E. *ACS Nano* **2009**, *3*, 1267–1273.

[89] Nair, G.; Chang, L.-Y.; Geyer, S. M.; Bawendi, M. G. *Nano Letters* **2011**, *11*, 2145–2151.

[90] Saari, J. I.; Dias, E. A.; Reifsnyder, D.; Krause, M. M.; Walsh, B. R.; Murray, C. B.; Kambhampati, P. *The Journal of Physical Chemistry B* **0**, *0*, null.

[91] Murray, C. B.; Norris, D. J.; Bawendi, M. G. *Journal of the American Chemical Society* **1993**, *115*, 8706–15.

[92] Yin, Y.; Alivisatos, A. P. *Nature (London, United Kingdom)* **2005**, *437*, 664–670.

[93] Hill, N. A.; Whaley, K. B. *J. Chem. Phys. FIELD Full Journal Title:Journal of Chemical Physics* **1994**, *100*, 2831–7.

[94] Underwood, D. F.; Kippeny, T.; Rosenthal, S. J. *Journal of Physical Chemistry B* **2001**, *105*, 436–443.

[95] Kalyuzhny, G.; Murray, R. W. *The Journal of Physical Chemistry B* **2005**, *109*, 7012–7021.

[96] Califano, M.; Franceschetti, A.; Zunger, A. *Nano Letters* **2005**, *5*, 2360–2364.

[97] Kippeny, T. C.; Bowers, M. J.; Dukes, A. D.; McBride, J. R.; Orndorff, R. L.; Garrett, M. D.; Rosenthal, S. J. *Journal of Chemical Physics* **2008**, *128*.

[98] Kilina, S.; Velizhanin, K. A.; Ivanov, S.; Prezhdo, O. V.; Tretiak, S. *ACS Nano* **2012**, *6*, 6515–6524.

[99] Mooney, J.; Krause, M. M.; Saari, J. I.; Kambhampati, P. *Phys. Rev. B* **2013**, *87*, 081201.

[100] Pang, Q.; Zhao; Cai, Y.; Nguyen, D. P.; Regnault, N.; Wang, N.; Yang; Ge; Ferreira, R.; Bastard, G.; Wang *Chemistry of Materials* **2005**, *17*, 5263–5267.

[101] Talapin, D. V.; Nelson, J. H.; Shevchenko, E. V.; Aloni, S.; Sadtler, B.; Alivisatos, A. P. *Nano letters* **2007**, *7*, 2951–9.

[102] Klimov, V. I.; Ivanov, S. A.; Nanda, J.; Achermann, M.; Bezel, I.; McGuire, J. A.; Piryatinski, A. *Nature* **2007**, *447*, 441–446.

[103] Nizamoglu, S.; Demir, H. V. *Optics Express* **2008**, *16*, 3515–3526.

[104] Dias, E. A.; Grimes, A. F.; English, D. S.; Kambhampati, P. *Journal of Physical Chemistry C* **2008**, *112*, 14229–14232.

[105] Efros, A. L.; Efros, A. L. *Soviet Physics Semiconductors Ussr* **1982**, *16*, 772–775.

[106] Brus, L. E. *Journal of Chemical Physics* **1983**, *79*, 5566–71.

[107] Fu, H.; Wang, L.-W.; Zunger, A. *Physical Review B: Condensed Matter and Materials Physics* **1998**, *57*, 9971–9987.

[108] Lee, S.; Kim, J.; Jönsson, L.; Wilkins, J. W.; Bryant, G. W.; Klimeck, G. *Physical Review B* **2002**, *66*, 235307.

[109] Prezhdo, O. V. *Accounts of Chemical Research* **2009**, *42*, 2005–2016.

[110] Efros, A. L.; Rosen, M.; Kuno, M.; Nirmal, M.; Norris, D. J.; Bawendi, M. *Physical Review B* **1996**, *54*, 4843–4856.

[111] Boyd, R. W. *Nonlinear Optics*; Academic press, 1992.

[112] Alivisatos, A. P. *Science (Washington, D. C.)* **1996**, *271*, 933–7.

[113] Pandey, A.; Guyot-Sionnest, P. *Journal of Chemical Physics* **2007**, *127*, 111104/1–111104/4.

[114] Klimov, V. I.; McGuire, J. A.; Schaller, R. D.; Rupasov, V. I. *Physical Review B* **2008**, *77*, 195324.

[115] Schaller, R. D.; Klimov, V. I. *Physical Review Letters* **2006**, *96*, 097402/1.

[116] Jin, S. Y.; Lian, T. Q. *Nano Letters* **2009**, *9*, 2448–2454.

[117] Huang, J. E.; Huang, Z. Q.; Jin, S. Y.; Lian, T. Q. *Journal of Physical Chemistry C* **2008**, *112*, 19734–19738.

[118] Huang, J.; Stockwell, D.; Huang, Z. Q.; Mohler, D. L.; Lian, T. Q. *Journal of the American Chemical Society* **2008**, *130*, 5632–+.

[119] Huang, J.; Huang, Z. Q.; Yang, Y.; Zhu, H. M.; Lian, T. Q. *Journal of the American Chemical Society* **2010**, *132*, 4858–4864.

[120] Frantsuzov, P.; Kuno, M.; Janko, B.; Marcus, R. A. *Nature Physics* **2008**, *4*, 519–522.

[121] Trinh, M. T.; Houtepen, A. J.; Schins, J. M.; Hanrath, T.; Piris, J.; Knulst, W.; Goossens, A.; Siebbeles, L. D. A. *Nano Letters* **2008**, *8*, 1713–1718.

[122] Franceschetti, A.; An, J. M.; Zunger, A. *Nano Letters* **2006**, *6*, 2191–2195.

[123] Shabaev, A.; Efros, A. L.; Nozik, A. J. *Nano Letters* **2006**, *6*, 2856–2863.

[124] Klimov, V. I. *Journal of Physical Chemistry B* **2000**, *104*, 6112–6123.

[125] Sewall, S. L.; Franceschetti, A.; Cooney, R. R.; Zunger, A.; Kambhampati, P. *Physical Review B* **2009**, *80*, 081310(R).

[126] Sewall, S. L.; Cooney, R. R.; Kambhampati, P. *Applied Physics Letters* **2009**, *94*, 243116–3.

[127] Cooney, R. R.; Sewall, S. L.; Dias, E. A.; Sagar, D. M.; Anderson, K. E. H.; Kambhampati, P. *Physical Review B* **2007**, *75*, 245311–14.

[128] Anderson, K. E. H.; Sewall, S. L.; Cooney, R. R.; Kambhampati, P. *Review of Scientific Instruments* **2007**, *78*, 073101–6.

[129] Nanda, J.; Ivanov, S. A.; Htoon, H.; Bezel, I.; Piryatinski, A.; Tretiak, S.; Klimov, V. I. *Journal of Applied Physics* **2006**, *99*.

[130] Klimov, V. I.; McBranch, D. W.; Leatherdale, C. A.; Bawendi, M. G. *Physical Review B* **1999**, *60*, 13740–13749.

[131] Klimov, V. I.; Schwarz, C. J.; McBranch, D. W.; Leatherdale, C. A.; Bawendi, M. G. *Physical Review B* **1999**, *60*, R2177–R2180.

[132] Guyot-Sionnest, P.; Hines, M. A. *Applied Physics Letters* **1998**, *72*, 686–688.

[133] Guyot-Sionnest, P.; Shim, M.; Matranga, C.; Hines, M. *Physical Review B* **1999**, *60*, R2181–R2184.

[134] Wehrenberg, B. L.; Wang, C. J.; Guyot-Sionnest, P. *Journal of Physical Chemistry B* **2002**, *106*, 10634–10640.

[135] Guyot-Sionnest, P.; Wehrenberg, B.; Yu, D. *Journal of Chemical Physics* **2005**, *123*, 074709/1–074709/7.

[136] Burda, C.; Link, S.; Mohamed, M.; El-Sayed, M. *Journal of Physical Chemistry B* **2001**, *105*, 12286–12292.

[137] Norris, D. J.; Bawendi, M. G. *Physical Review B* **1996**, *53*, 16338–16346.

[138] Hoheisel, W.; Colvin, V. L.; Johnson, C. S.; Alivisatos, A. P. *Journal of Chemical Physics* **1994**, *101*, 8455–60.

[139] Burda, C.; Link, S.; Green, T. C.; El-Sayed, M. A. *Journal of Physical Chemistry B* **1999**, *103*, 10775–10780.

[140] Son, D. H.; Wittenberg, J. S.; Banin, U.; Alivisatos, A. P. *Journal of Physical Chemistry B* **2006**, *110*, 19884–19890.

[141] Li, S.; Steigerwald, M. L.; Brus, L. E. *ACS Nano* **2009**, *3*, 1267–1273.

[142] Pandey, A.; Guyot-Sionnest, P. *Science* **2008**, *322*, 929–932.

[143] Klimov, V. I.; McBranch, D. W.; Leatherdale, C. A.; Bawendi, M. G. *Physical Review B: Condensed Matter and Materials Physics* **1999**, *60*, 13740–13749.

[144] Franceschetti, A.; Zhang, Y. *Physical Review Letters* **2008**, *100*, 136805–4.

[145] Sykora, M.; Koposov, A. Y.; McGuire, J. A.; Schulze, R. K.; Tretiak, O.; Pietryga, J. M.; Klimov, V. I. *Acs Nano* **2010**, *4*, 2021–2034.

[146] Murray, C. B.; Sun, S.; Gaschler, W.; Doyle, H.; Betley, T. A.; Kagan, C. R. *IBM Journal of Research and Development* **2001**, *45*, 47–56.

[147] Kuno, M.; Fromm, D. P.; Hamann, H. F.; Gallagher, A.; Nesbitt, D. J. *Journal of Chemical Physics* **2000**, *112*, 3117–3120.

[148] Neuhauser, R. G.; Shimizu, K. T.; Woo, W. K.; Empedocles, S. A.; Bawendi, M. G. *Physical Review Letters* **2000**, *85*, 3301–3304.

[149] Shimizu, K. T.; Neuhauser, R. G.; Leatherdale, C. A.; Empedocles, S. A.; Woo, W. K.; Bawendi, M. G. *Physical Review B: Condensed Matter and Materials Physics* **2001**, *63*, 205316/1–205316/5.

[150] Knappenberger, J., Kenneth L.; Wong, D. B.; Romanyuk, Y. E.; Leone, S. R. *Nano Letters* **2007**, *7*, 3869–3874.

[151] Gomez, D. E.; Califano, M.; Mulvaney, P. *Physical Chemistry Chemical Physics* **2006**, *8*, 4989–5011.

[152] Wang, X. Y.; Ren, X. F.; Kahen, K.; Hahn, M. A.; Rajeswaran, M.; Maccagnano-Zacher, S.; Silcox, J.; Cragg, G. E.; Efros, A. L.; Krauss, T. D. *Nature* **2009**, *459*, 686–689.

[153] Peterson, J. J.; Nesbitt, D. J. *Nano Letters* **2009**, *9*, 338–345.

[154] Fomenko, V.; Nesbitt, D. J. *Nano Letters* **2008**, *8*, 287–293.

[155] Rosen, S.; Schwartz, O.; Oron, D. *Physical Review Letters* **2010**, *104*, 157404.

[156] Efros, A. L.; Rosen, M. *Annual Review of Materials Science* **2000**, *30*, 475–521.

[157] Livermore, C.; Crouch, C. H.; Westervelt, R. M.; Campman, K. L.; Gossard, A. C. *Science* **1996**, *274*, 1332–1335.

[158] Son, D. H.; Wittenberg, J. S.; Alivisatos, A. P. *Physical Review Letters* **2004**, *92*, 127406/1–127406/4.

[159] Hendry, E.; Koeberg, M.; Bonn, M. *Physical Review B* **2007**, *76*, 045214–6.

[160] Gambetta, A.; Manzoni, C.; Menna, E.; Meneghetti, M.; Cerullo, G.; Lanzani, G.; Tretiak, S.; Piryatinski, A.; Saxena, A.; Martin, R. L.; Bishop, A. R. *Nature Physics* **2006**, *2*, 515–520.

[161] Norris, D. J.; Efros, A. L.; Rosen, M.; Bawendi, M. G. *Physical Review B: Condensed Matter* **1996**, *53*, 16347–16354.

[162] Steiner, M.; Freitag, M.; Perebeinos, V.; Tsang, J. C.; Small, J. P.; Kinoshita, M.; Yuan, D.; Liu, J.; Avouris, P. *Nature Nanotechnology* **2009**, *4*, 320 – 324.

[163] Perebeinos, V.; Tersoff, J.; Avouris, P. *Physical Review Letters* **2005**, *94*, 086802.

[164] Franceschetti, A.; Zunger, A. *Physical Review Letters* **1997**, *78*, 915–918.

[165] Kilina, S. V.; Kilin, D. S.; Prezhdo, O. V. *ACS Nano* **2009**, *3*, 93–99.

[166] Bardeen, C. J.; Wang, Q.; Shank, C. V. *Physical Review Letters* **1995**, *75*, 3410–13.

[167] Salvador, M. R.; Graham, M. W.; Scholes, G. D. *Journal of Chemical Physics* **2006**, *125*, 184709.

[168] Chilla, G.; Kipp, T.; Menke, T.; Heitmann, D.; Nikolic, M.; Fromsdorf, A.; Kornowski, A.; Forster, S.; Weller, H. *Physical Review Letters* **2008**, *100*, 057403–4.

[169] Liu, T.-M.; Yang, M.-J.; Lai, C.-W.; Chou, P.-T.; Chang, M.-H.; Liu, H.-L.; Sun, C.-K. *Physical Review B* **2008**, *77*, 085428–5.

[170] Hines, M. A.; Guyot-Sionnest, P. *Journal of Physical Chemistry* **1996**, *100*, 468–71.

[171] Klimov, V. I. *Semiconductor and Metal nanocrystals: Synthesis and Electronic and Optical Properties.*; Klimov Victor, I., Ed.; Marcel Dekker: New York, 2004.

[172] Malko, A. V.; Mikhailovsky, A. A.; Petruska, M. A.; Hollingsworth, J. A.; Klimov, V. I. *Journal of Physical Chemistry B* **2004**, *108*, 5250–5255.

[173] Klimov, V. I. *Optical Engineering (New York, NY, United States)* **2004**, *87*, 159–214.

[174] Piryatinski, A.; Ivanov, S. A.; Tretiak, S.; Klimov, V. I. *Nano Letters* **2007**, *7*, 108–115.

[175] Brovelli, S.; Schaller, R. D.; Crooker, S. A.; Garcia-Santamaria, Y., F.; Chen; Viswanatha, R.; Hollingsworth, J. A.; Htoon, H.; Klimov, V. I. *Nature Communications* **2011**, *2*, 280.

[176] Nanda, J.; Ivanov, S. A.; Htoon, H.; Bezel, I.; Piryatinski, A.; Tretiak, S.; Klimov, V. I. *Journal of Applied Physics* **2006**, *99*, 034309/1–034309/7.

[177] Muller, J.; Lupton, J. M.; Lagoudakis, P. G.; Schindler, F.; Koeppe, R.; Rogach, A. L.; Feldmann, J.; Talapin, D. V.; Weller, H. *Nano Letters* **2005**, *5*, 2044–2049.

[178] Kostić, R.; Stojanović, D. *Acta Physica Polonica, A* **2009**, *132*, 598–602.

[179] Zhu, H. M.; Song, N. H.; Lian, T. Q. *Journal of the American Chemical Society* **2010**, *132*, 15038–15045.

[180] Vukmirović, N.; Wang, L.-W. In *Comprehensive Nanoscience and Technology*; Andrews, D. L.; Scholes, G. D.; Wiederrecht, G. P., Eds.; Academic Press: Amsterdam, 2011; pp 189 – 217.

[181] Nirmal, M.; Norris, D. J.; Kuno, M.; Bawendi, M. G.; Efros, A. L.; Rosen, M. *Physical Review Letters* **1995**, *75*, 3728–31.

[182] Haus, J. W.; Zhou, H. S.; Honma, I.; Komiyama, H. *Phys. Rev. B* **1993**, *47*, 1359–65.

[183] Efros, A. L.; Rodina, A. V. *Solid State Communications* **1989**, *72*, 645–649.

[184] Brus, L. E. *Journal of Chemical Physics* **1984**, *80*, 4403–9.

[185] Stratton, J. *Electromagnetic Theory*; McGraw-Hill Book Company, Inc.: New York and London, 1941.

[186] Wheeler, R. G.; Dimmock, J. O. *Physics Review* **1962**, *125*, 1805–1815.

[187] Miklosz, J. C.; Wheeler, R. G. *Physical Review* **1967**, *153*, 913–923.

[188] Efros, A. L. *Physical Review B: Condensed Matter and Materials Physics* **1992**, *46*, 7448–58.

[189] Htoon, H.; Malko, A. V.; Bussian, D.; Vela, J.; Chen, Y.; Hollingsworth, J. A.; Klimov, V. I. *Nano Letters* **2010**, *10*, 2401–2407.

[190] Oron, D.; Kazes, M.; Banin, U. *Physical Review B* **2007**, *75*, 035330/1–035330/7.

[191] Nanda, J.; Ivanov, S. A.; Achermann, M.; Bezel, I.; Piryatinski, A.; Klimov, V. I. *Journal of Physical Chemistry C* **2007**, *111*, 15382–15390.

[192] Wong, C. Y.; Kim, J.; Nair, P. S.; Nagy, M. C.; Scholes, G. D. *Journal of Physical Chemistry C* **2009**, *113*, 795–811.

[193] Turner, D. B.; Hassan, Y.; Scholes, G. D. *Nano Letters* **2012**, *12*, 880–886.

[194] Lutich, A. A.; Mauser, C.; Da Como, E.; Huang, J.; Vaneski, A.; Talapin, D. V.; Rogach, A. L.; Feldmann, J. *Nano Letters* **2010**, *10*, 4646–4650.

[195] Stone, K. W.; Gundogdu, K.; Turner, D. B.; Li, X.; Cundiff, S. T.; Nelson, K. A. *Science* **2009**.

[196] Turner, D. B.; Nelson, K. A. *Nature* **2010**, *466*, 1089–1092.

[197] Wong, C. Y.; Scholes, G. D. *Journal of Physical Chemistry A* **2010**, *115*, 3797–3806.

[198] Wong, C. Y.; Scholes, G. D. *Journal of Luminescence* **2011**, *131*, 366 – 374; ¡ce:title¿Selected papers from DPC'10¡/ce:title¿.

[199] Yurs, L. A.; Block, S. B.; Pakoulev, A. V.; Selinsky, R. S.; Jin, S.; Wright, J. *The Journal of Physical Chemistry C* **2011**, *115*, 22833–22844.

[200] Harel, E.; Rupich, S. M.; Schaller, R. D.; Talapin, D. V.; Engel, G. S. *Phys. Rev. B* **2012**, *86*, 075412.

[201] Brixner, T.; Stenger, J.; Vaswani, H.; Cho, M.; Blankenship, R.; Fleming, G. *Nature* **2005**, *434*, 625.

[202] Read, E. L.; Schlau-Cohen, G. S.; Engel, G. S.; Wen, J.; Blankenship, R. E.; Fleming, G. R. *Biophysical Journal* **2008**, *95*, 847–856.

[203] Myers, J. A.; Lewis, K. L. M.; Fuller, F. D.; Tekavec, P. F.; Yocum, C. F.; Ogilvie, J. P. *The Journal of Physical Chemistry Letters* **2010**, *1*, 2774–2780.

[204] Lewis, K. L. M.; Ogilvie, J. P. *The Journal of Physical Chemistry Letters* **2012**, *3*, 503–510.

[205] Li, X.; Zhang, T.; Borca, C. N.; Cundiff, S. T. *Physical Review Letters* **2006**, *96*, 057406/1–057406/4.

[206] Shim, S.-H.; Strasfeld, D. B.; Ling, Y. L.; Zanni, M. T. *Proceedings of the National Academy of Sciences of the United States of America* **2007**, *104*, 14197–14202.

[207] Engel, G. S.; Calhoun, T. R.; Read, E. L.; Ahn, T.-K.; Mancal, T.; Cheng, Y.-C.; Blankenship, R. E.; Fleming, G. R. *Nature (London, United Kingdom)* **2007**, *446*, 782–786.

[208] Vaughan, J. C.; Hornung, T.; Stone, K. W.; Nelson, K. A. *J. Phys. Chem. A* **2007**, *111*, 4873.

[209] Gundogdu, K.; Stone, K. W.; Turner, D. B.; Nelson, K. A. *Chem. Phys.* **2007**, *341*, 89.

[210] Grumstrup, E. M.; Shim, S.-H.; Montgomery Matthew, A.; Damrauer Niels, H.; Zanni Martin, T. *Optics Express* **2007**, *15*, 16681.

[211] Myers, J. A.; Lewis, K. L. M.; Tekavec, P. F.; Ogilvie, J. P. *Opt. Express* **2008**, *16*, 17420.

[212] DeFlores, L. P.; Nicodemus, R. A.; Tokmakoff, A. *Opt. Lett.* **2007**, *32*, 2966.

[213] Tian, P.; Keusters, D.; Suzaki, Y.; Warren, W. S. *Science* **2003**, *300*, 1553.

[214] Wagner, W.; Li, C.; Semmlow, J.; Warren, W. S. *Opt. Express FIELD Full Journal Title:Optics Express* **2005**, *13*, 3697–3706.

[215] Tekavec, P. F.; Myers, J. A.; Lewis, K. L. M.; Ogilvie, J. P. *Opt. Lett.* **2009**, *34*, 1390–1392.

[216] Xiong, W.; Zanni Martin, T. *Opt Lett FIELD Full Journal Title:Optics letters* **2008**, *33*, 1371–3.

[217] Middleton, C. T.; Strasfeld, D. B.; Zanni, M. T. *Opt. Express* **2009**, *17*, 14526–14533.

[218] Jonas, D. M. *Annual Review of Physical Chemistry* **2003**, *54*, 425–463.

[219] Khalil, M.; Demirdoven, N.; Tokmakoff, A. *Phys. Rev. Lett.* **2003**, *90*, 047401.

[220] Zhang, Z.; Wells, K. L.; Hyland, E. W. J.; Tan, H.-S. *Chemical Physics Letters* **2012**, *550*, 156 – 161.

[221] Yan, S.; Tan, H.-S. *Chemical Physics* **2009**, *360*, 110–115.

[222] Tan, H.-S. *J. Chem. Phys.* **2008**, *129*, 124501–13.

[223] Stone, K. W.; Turner, D. B.; Gundogdu, K.; Cundiff, S. T.; Nelson, K. A. *Accounts of Chemical Research* **2009**, *42*, 1452–1461.